

Politecnico di Torino
Master's Degree in Aerospace Engineering



Master's Degree Thesis

**Study of iQfoil's settings and performance
investigation through 6 DOF dynamic model**

Supervisor:
Prof. Giuliana MATTIAZZO

Candidate:
Matteo MASTORAKIS

Cosupervisors:
Dr. Pietro CASALONE
Dr. Mauro BONFANTI

2023/2024

*La porta devone essere
correttamente aperte e
richiusa.*

Abstract

The gradual inclusion of an increasing number of foiling classes in the Olympic games is prompting national teams to seek consultancy to reduce the adaptation time to this technology. The higher complexity of the system and the lack of training due to the novelty of the discipline pose new challenges for athletes and coaches while providing a unique opportunity to study the involved aerodynamic and flight mechanics for engineers.

This thesis aims to take this opportunity to work with FIV's Olympic team and give to it a map of regulations and attitude effects. To pursue this goal a **3DOF static model** has been implemented which could answer their questions. This necessitated the establishment of geometric and aerodynamic characterizations from a member of the fleet. Subsequently, a non-linear equilibrium equations system was formulated and solved for each condition specified by the FIV's coaches.

Following this, a further investigation was conducted, encompassing **6DOF static and dynamic models** and a tool that linearises them. The latter has been crucial for performing the stability analysis and the examination of degrees of freedom coupling. In the end, a controller has been developed to stabilise unstable modes and enable the imposition of a new desired attitude. This approach allowed for the simulation of plausible regatta conditions and the assessment of **performance and athlete effort**.

Contents

1	Introduction	12
1.1	Thesis structure	13
2	iQfoil class overview	14
2.1	Class equipment	14
2.1.1	Components	14
2.1.2	Control system	16
2.1.3	Settings	17
2.2	Class race	18
3	Geometric modellization	20
3.1	Foils 3D scanning and CAD reconstruction	20
3.2	Board geometric survey	22
3.3	Other components CAD models	23
3.4	Centre of gravity measurement	23
3.5	Effective rake measurement problem	25
4	Aerodynamic characterisation	27
4.1	Foils	27
4.1.1	XFLR5: geometries reconstruction	27
4.1.2	XFLR5: analysis settings and results	28
4.1.3	STAR CCM+: mesh	30
4.1.4	STAR CCM+: analysis setting and results	32
4.1.5	STAR CCM+ and XFLR5: results comparison and conclusion	37
4.2	Board	37
4.2.1	STAR CMM+: mesh and analysis setting	38
4.2.2	STAR CMM+: results	40
4.3	STAR CCM+: convergence analysis	41
5	3DOF static model	45
5.1	Structure	45
5.2	Regulations and controls	46
5.3	Magnitude and angle of the airflow	46
5.4	Equilibrium equations	47
5.5	Results	49
5.5.1	tail rake's effects	49
5.5.2	Flight height effect	51
5.5.3	Board rake effect	52

6	6DOF static model	58
6.1	Structure	58
6.2	Sail model	59
6.2.1	Sail power control	60
6.2.2	Sail force coefficient	60
6.3	Attack angles determination	61
6.4	Foil's lateral-directional coefficients	62
6.5	Equilibrium equations	63
6.6	Solution method	64
6.7	Results	66
7	6DOF dynamic model: Plant	68
7.1	Structure	68
7.2	Dynamic system solution	69
7.3	Inertia matrix	71
7.3.1	Inertia update function	72
7.3.2	Interpolating inertia matrices	73
7.4	Model linearisation	75
7.4.1	Linearisation validation	81
8	Control system	83
8.1	Structure	83
8.2	Gains matrix choice	85
8.3	Open loop state-space model	86
8.4	Q and R weights definition	87
8.5	Case studies	90
8.5.1	Disturbance on true wind angle	90
8.5.2	Disturbance on wind intensity	91
8.5.3	Disturbance due to sea waves	92
8.6	Results	94
8.6.1	Wind angle disturbances	94
8.6.2	Wind speed disturbances	96
8.6.3	Sea waves effect	98
8.6.4	Roll step command effect	99
8.6.5	Yaw step commands effect	102
8.6.6	descending step command effect	104
8.6.7	Graphical representation	108
9	Conclusion and Future Works	110
A	6DOF static model solution method	113

B state space models **115**
 B.1 Plant state-space model 115
 B.2 Open loop state-space model 117

C Linearisation validation **118**

List of Tables

1	Foil’s aerodynamic derivatives and constant terms extrapolated from XF5 analysis.	30
2	Foil’s requested reports.	33
3	Foil’s aerodynamic derivatives and constant terms extrapolated from CFDs.	34
4	Board’s required reports.	39
5	Convergence trend in function of R	43
6	p and R parameters for foil and board.	43
7	Error and uncertainty of foil and board analysis.	43
8	Aerodynamics coefficients dependencies and sources.	48
9	Aerodynamics lateral-directional coefficients derivatives [17].	62
10	Aerodynamics lateral-directional coefficients derivatives (numerical values).	62
11	Components’ force vector in the flow reference system and the angles to rotate them in body axis.	63
12	Comparison between the results obtained through GA and gradient based algorithm.	66
13	Comparison between four cases study.	66
14	Effect in macro-changing in Q matrix.	87
15	Effect in macro-changing in R matrix.	87
16	Waves assumed specifications.	93
17	Time domain specification about a 30° roll step command.	101
18	Time domain specification about a two turn step command.	103
19	Time domain specification about a descending step command.	105
20	Solutions for the underdetermined equilibrium problem starting from twenty different points and with no criteria of selection.	113
21	Solutions for the underdetermined equilibrium problem starting from twenty different points and with the selection criteria based on the weighted objective function.	114

List of Figures

1	Iqfoil in regatta[5].	14
2	Board and sail nomenclature.	15
3	Strut and foil nomenclature.	16
4	<i>Starboard</i> convention for tail rakes[5]. Later, 0.5 rake has been added.	17
5	Centre of gravity displacement due to board rake.	18
6	Possible course racing courses.	19
7	Original mainfoil <i>iges</i> model made of 7474 surfaces (a) and a close-up of the mainfoil tip and elementary surfaces dimensions (b)	20

8	Edge and sections duplication process (a) , and input and output of the curve rebuilding process (b)	21
9	Final results of hydrodynamic surfaces scanning and rebuilding.	22
10	Board upper (a) and lower (b) surfaces.	22
11	IQfoil assembly and athlete.	23
12	Synthetic scheme of the experimental centre of gravity method.	24
13	Mainfoil's rake measurement tool CAD (a) and the 3D printed prototypes (b)	25
14	Demonstration of mainfoil's tool at work.	26
15	<i>Grasshopper</i> graphical algorithm for interpolating point extraction (a) and its operating point views on <i>XFLR5</i> (b)	27
16	IQfoil's foils in XFLR5 environment.	28
17	Mainfoil (a) and tail (b) polar graphs.	29
18	Whole foil polar graphs.	29
19	Pitch torque VS Lift force at different speed and for different tail rakes.	30
20	Foils whole mesh lateral (a) and around the components' (b) view.	31
21	Close-up of the mesh around the mainfoil wall.	31
22	Close-up on the prism layer mesh around the tail wall.	32
23	Foil simulation boundaries.	32
24	Foil mesh lateral view at 0° of incidence.	33
25	Comparison between CL from CFD simulations and the relative regression for the mainfoil (a) and for the tail (b)	35
26	Comparison between CD from CFD simulations and the relative regression for the mainfoil (a) and for the tail (b)	35
27	Comparison between CM from CFD simulations and the relative regression for the mainfoil (a) and for the tail (b)	36
28	Close-up of velocity field around the mainfoil.	36
29	Pressure field around the foil (a) and a close up around the tail (b)	37
30	Board simulation boundaries.	38
31	Mesh for board aerodynamic simulation.	38
32	Close-up of the mesh around the board.	39
33	Pressure field on the board.	39
35	Velocity field around the board.	40
34	Pressure field near the board.	40
36	Comparison between CFD results and the implemented regression for CL($AWA = 30^\circ$) (36a) and CL($AWA = 60^\circ$) (36b)	41
37	Comparison between CFD results and the implemented regression for CD($AWA = 30^\circ$) (a) and CD($AWA = 60^\circ$) (b)	41
38	Mesh for board simulation with base size 1.1 (a) , 2.2 (b) and 4.4 (c)	42
39	Error (a) and uncertainty (b) on foil lift.	44
40	Error (a) and uncertainty (b) on board drag.	44
41	3DOF static model structure.	45

42	True and apparent wind.	47
43	3DOF model's reference system.	48
44	Tail rake effect on longitudinal control.	50
45	Flight height effect on strut drag.	51
46	Flight height effect on strut drag.	52
47	Board rake effect on drag when sailing upwind.	53
48	Board rake effect on drag when sailing beam reaching.	53
49	Board rake effect on drag when sailing downwind.	54
50	Board rake effect on longitudinal control when sailing upwind.	55
51	Board rake effect on longitudinal control when sailing beam reaching.	55
52	Board rake effect on longitudinal control when sailing downwind.	56
53	6DOF static model structure.	59
54	Sail power logic.	60
55	Sail CL- α curve [4].	61
56	Comparison between empirical and numeric iQfoil polar graph.	67
57	6DOF plant dynamic model structure.	69
58	Inertia update function structure.	72
59	Inertia interpolating matrices generator structure.	73
60	Athlete movement representation.	74
61	Comparison between the CAD computed inertias and the resulting interpolation as a function of a 100Kg athlete position.	75
62	A and B matrices linearisation script structure.	77
63	Root locus of the system linearised for $U = 31.5kn$, $TWS = 25kn$, $TWA = 60^\circ$	78
64	Argand diagram for the first oscillatory mode	78
65	Argand diagram for the second oscillatory mode.	79
66	Argand diagram for the third oscillatory mode	79
67	Root locus of the complete and of the decoupled systems superimposed (a) and a close-up on the poles nearer to the origin (b)	80
68	Physical representation of the yaw and roll moments caused by a $\Delta\alpha$	81
69	Measurement of the period of the second mode of the system	82
70	Control system block diagram.	83
71	Actuators' Bode diagram (a) and outputs to three unit sine waves: $\omega_{cut-off}$, $0.1\omega_{cut-off}$ and $10\omega_{cut-off}$ (b)	84
72	response to roll step command and the sail power trend for the optimised and refined controllers.	88
73	Evolution through time of an irregular wind direction.	91
74	Evolution through time of wind direction doublet.	91
75	Evolution through time of an irregular wind intensity.	92
76	Evolution through time of an wind intensity doublet.	92
77	Sea waves evolution through time (a) and the induced $\Delta\alpha$ (b)	93
78	AWA (a) and ψ (b) evolution under a random wind angle variation.	94

79	z (a) and ϕ (b) evolution under a random wind angle variation.	94
80	AWA (a) and ψ (b) evolution after a doublet wind angle variation.	95
81	z (a) and ϕ (b) evolution after a doublet wind angle variation.	96
82	ϕ (a) and ψ (b) evolution during a random wind speed variation.	96
83	z evolution during a random wind speed variation.	97
84	z (a) and ψ (b) evolution after a doublet wind speed variation.	97
85	ϕ evolution after a doublet wind speed variation.	98
86	Sea waves effect on flight height.	99
87	z (a) and ψ (b) evolution after a 30° roll step command.	100
88	ϕ evolution after a 30° roll step command.	100
89	β evolution after a 30° roll step command.	101
90	z (a) and ϕ (b) evolution after a two turn step command.	102
91	ψ evolution after a two turn step command.	102
92	x_{sail} evolution after a two turn step command.	104
93	ϕ (a) and ψ (b) evolution after a descending step command.	104
94	Altitude through time after a descending step command.	105
95	x_{ath} evolution after a descending step command.	106
96	α and θ evolution after a descending step command.	106
97	Graphical representation tool flowchart.	108
98	Graphical representation of the roll manoeuvre treated in par. 8.6.4 (a) and the frame structure (b).	109
99	Screenshot of the output video.	109
100	Responses comparison between analytic linearised model and numeric non-linear one - z	118
101	Responses comparison between analytic linearised model and numeric non-linear one - ϕ	119
102	Responses comparison between analytic linearised model and numeric non-linear one - θ	119
103	Responses comparison between analytic linearised model and numeric non-linear one - ψ	120
104	Responses comparison between analytic linearised model and numeric non-linear one - U	120
105	Responses comparison between analytic linearised model and numeric non-linear one - α	121
106	Responses comparison between analytic linearised model and numeric non-linear one - β	121
107	Responses comparison between analytic linearised model and numeric non-linear one - $\dot{\phi}$	122
108	Responses comparison between analytic linearised model and numeric non-linear one - $\dot{\theta}$	122

109	Responses comparison between analytic linearised model and numeric non-linear one - $\dot{\psi}$	123
-----	--	-----

1 Introduction

In November 2019 the World Sailing Council approved the iQFoil as the equipment for windsurfing events at the 2024 Olympic games in France, replacing the RS:X [1]. The new format will make its first appearance at the leading international sporting event on July 28th 2024 at the opening series [2]. The transition to foiling technology has already happened for *Nacra XVII* and will happen for kitesurfing events too, suggesting the direction that the world of sailing is taking.

At that time, I was involved in *PoliTo Sailing Team* [3] activities as head of *Glaros'* project, a two-person foiling dinghy. Thanks to this incredibly formative work, the Italian Sail Federation's president, Francesco Ettorre, and the Turin-based student team met at Polytechnic on January 19th 2022. On that occasion, the groundwork for a relationship has been laid. Specifically, the FIV asked for a consultancy about the aforementioned windsurfing class. The principal issue they were facing then concerned the so-called over-lift phenomenon. It happens at high speed, especially downwind, when a disturbance can cause the lift to increase much over the total weight and the foil to emerge out of the water. Moreover, they guessed the role of each regulation in retarding the over-lift, but they wanted a more quantitative analysis to achieve a functional setting method. They asked, in addition, to investigate the board and tail aerodynamics, to better understand the effect on their rake. In the first stages of the collaboration, we decided by mutual agreement that the output of the work would have been a set of graphs. Unfortunately, a lot of unknown variables undermined the chances of obtaining affordable values, but, as they emphasized, the greater support we could provide to them was the order of magnitude and the trends. For this reason, a 3DOF static model has been developed at first, ignoring the inertial coupling but excluding a lot of unknown variables, such as the sail. For each setting, the longitudinal athlete position has been plotted, to understand under which conditions there was a margin to compensate for the over-lift. In addition, every graph they expressively asked for has been realised and supplied to them.

The last part of this work consisted of a 6DOF static and dynamic model. They necessitated much more assumptions, reason why they were not used in the collaboration with the FIV. On the other side, this was a necessary step to evaluate the inertial and cinematic coupling. Moreover, to find eigenvalues and modes of the system, it had to be dynamically modeled. The greater assumptions regarded the sail coefficients and the *stability augmentation* and *pilot* system. The sail coefficients have been determined from an article reported in the bibliography ([4]) which doesn't fit exactly with the object of this thesis. The stabilisation and control system, instead, has been designed without the intention of exactly emulating human behavior, because of the impossibility of achieving such an ambitious goal. Nevertheless, a realistic description of the iQfoil-athlete couple has been reached, where unrealistic sailing points could not be navigated and too intense or weak wind did not allow the flight.

1.1 Thesis structure

This thesis begins with an overview of the iQfoil class, to get into the physics of the problem and the rules which justify the goals set. In the following sections 3 and 4 each component and the whole assembly is geometrically and aerodynamically characterised.

Then, the 3DOF model used for FIV consultancy and its responses are treated. Subsequently, the complete model is described, from the free response analysis to the effect of a double loop system effect on a realistic regatta's situation.

At last, results are resumed and some possible next steps are exposed.

2 iQfoil class overview

The iQfoil belongs to the wind-foil family, which is composed of all those windsurf equipped with foils. They differ from traditional windsurf in the ability to fly above the water free surface instead of planning. To describe it thoroughly and understand its operating in the next sections the role of each component will be explained. Then, an overview of settings and maneuverability will be provided.



Figure 1: Iqfoil in regatta[5].

2.1 Class equipment

2.1.1 Components

- **Sail, mast and boom:** the sail is a deformable wing that operates in the airflow due to the wind and the iQfoil velocity. Its function is to provide the system with the thrust necessary to overcome the aero-hydro-dynamic drag. The sail is constrained to

the board with a spherical hinge which allows the rotation around all three axis. Its pressure centre and incidence are determined by the athlete through the **boom**, a curved rigid beam that identifies the longer chord. The shape of the wing is given by the **mast**, a beam that goes from the board to the tip, the boom and the sticks, some flexible beams necessary to stiffen the sail.

- **Board:** the board is the component responsible for the hydrostatic force necessary before and during the take-off. Moreover, it connects the sail, the strut head and the **straps**, where the athlete keeps his feet. the forces between sail, athlete and board determine the relative positions of these three, which have various consequences on the iQfoil's aerodynamics and centre of gravity.

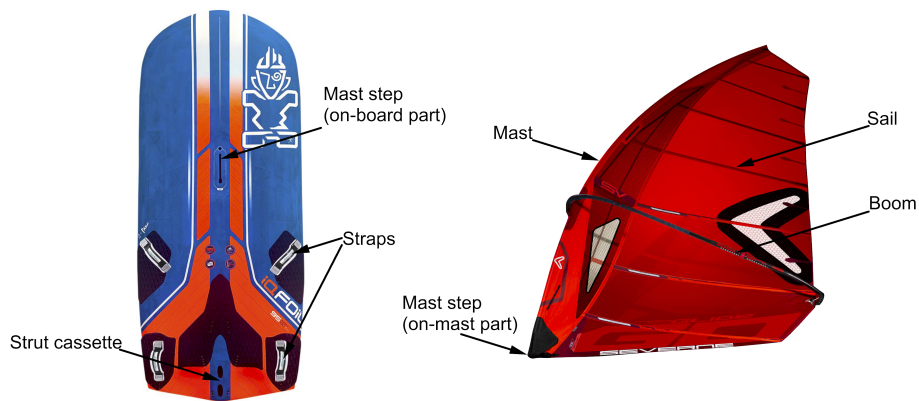


Figure 2: Board and sail nomenclature.

- **Strut:** the strut is that carbon wing with a vertical spanwise axis that transmits the loads between the foil and the board. Moreover, its section is a symmetric airfoil thanks to which the strut produces a lateral force and reduces the sideslip angle.
- **Foil:** the foil is a complex structure composed by **mainfoil**, **tail** and **fuselage**. The assembly works likewise in a plane where the mainfoil has the same function as the

wing and ensures the translational equilibrium along the vertical axis, the tail assumes the role of the elevator and the fuselage is the liaison body between the first two and the strut.



Figure 3: Strut and foil nomenclature.

2.1.2 Control system

As aforementioned, the foil works as a plane without moving surfaces. It flies underwater while the payload flies above the water with the sail which generates the trust. Different equilibrium points can be found for different attitudes and speeds moving the centre of gravity of the athlete, like a hang gliding. Moreover, the free body diagram shows a force asymmetry with respect to the longitudinal plane, which means that the athlete must appropriately move his weight laterally too. No rudder ensures the rotational equilibrium around the z-axis, but the sail can be rotated around the y-axis, moving back and forward its pressure centre. At last, the throttle can be controlled by modifying the incidence of the sail.

In this way, the rotational equilibrium can be imposed, while the translational ones are controlled by the athlete choosing the best attitude to maintain constant speeds along the three axis at the desired value. Usually, the desired vertical speed is null, while the lateral one is negative (the velocity vector lies between the longitudinal axis and the wind direction when sailing upwind) and as small as possible.

2.1.3 Settings

- **Tail rake:** angle between tail and mainfoil. In *Starboard*[®] convention, 0 is equivalent to a geometric rake of -2° . Positive rotations according to this convention are negative according to the aeronautical one.

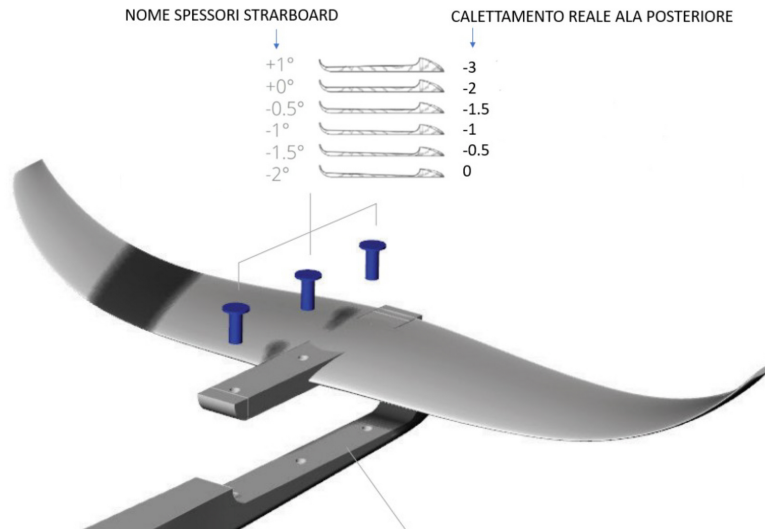


Figure 4: *Starboard* convention for tail rakes[5]. Later, *0.5* rake has been added.

- **Straps position** Straps position along the longitudinal axis. Moving the straps in the right place allows the athlete to work in a comfortable position. This setting will not be treated in this work because of its subjective nature.
- **Mast step:** mast step position along the longitudinal axis. The zero is placed at 114,5 cm from the aft. The setting range goes from 0 to 10 cm. The main effects of this regulation regard the sail's aerodynamics and the athlete's comfort. For different centres of rotation of the sail, the aerodynamic centre assumes different positions along both the vertical and longitudinal direction, and so do the pitch and the yaw moments. In addition, if the straps are near the aft, the mast cannot be too forward without decreasing the athlete's agility and vice versa. This setting will not be treated in this work too because of its subjective nature and dependence on sail aerodynamics.
- **board rake:** angle between the board and the strut. This setting modifies relative positions between the gravity and pressure centre of hydrodynamic surfaces. Often called **strut's rake**.

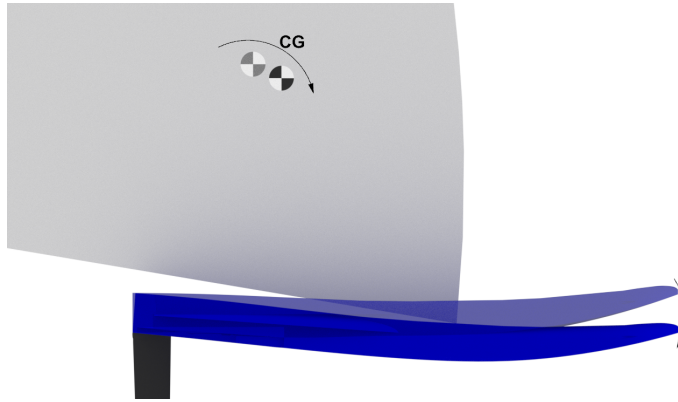


Figure 5: Centre of gravity displacement due to board rake.

2.2 Class race

It is advisable to know some notions about iQfoil's races. The goal of the collaboration with FIV is, indeed, to increase athletes' performances in regattas. First of all, there are three types of races: *Slalom sprint*, *course racing* and *marathon*. The course racing will be now considered because of its meaningfulness.

In the *iQfoil class race management guidelines* [5] the wind lower limit for the course racing format is 9 knots, while the upper is chosen by the regatta committee according to safety considerations. For what concerns the race path, it is defined by some buoys: iQfoils must turn around them, but they have not any constraints in between. The guideline reports four possible courses that require the athletes to sail upwind, downwind and, sometimes, beam reaching. This means that the path is composed of two or more segments that are parallel or nearly perpendicular to the wind direction. This kind of sailboards cannot move parallel to the wind, reason why, to reach the buoy, it is necessary to make a *zig-zag* path, introducing a variable due to different possible strategies. The distance between the buoys is about 0.85 – 1.05 nautical miles, meaning about 1.5 – 2km.

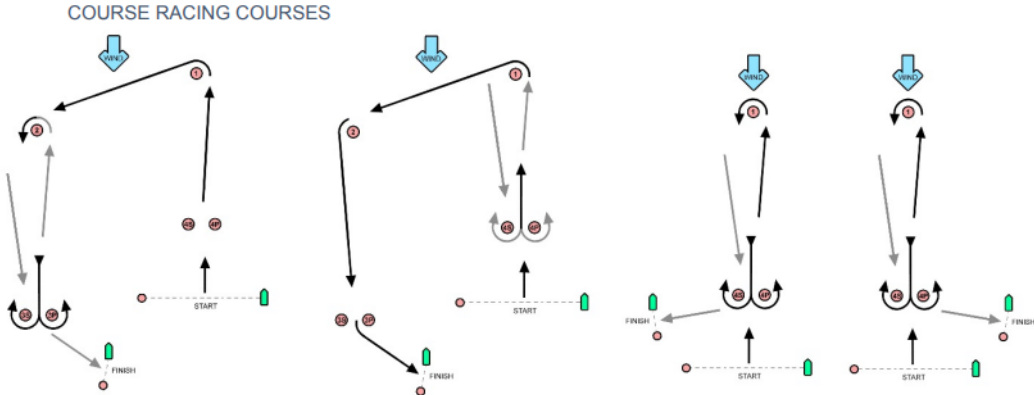


Figure 6: Possible course racing courses.

3 Geometric modellization

To effectively model such a complex system, it is essential to comprehensively describe each component from both inertial and fluidynamic perspectives. This approach allows for the holistic treatment of the entire system as an integrated assembly, which represents the ultimate objective of this work.

The initial phase of this endeavor involves the geometric reconstruction of the IQfoil, from one individual of FIV's fleet. In the following section, we will explore various methodologies employed for this purpose, including 3D laser scanning techniques for the foils and geometric surveys of the board, to obtain those CAD files necessary to characterise the fluidynamic properties of the components and their distribution in the space.

3.1 Foils 3D scanning and CAD reconstruction

The most critical components to replicate within the CAD environment were the foils, given their significant influence on the primary aerodynamic derivatives of the system. Consequently, it was imperative to ensure the utmost precision in reproducing these components, as even a slight deviation could significantly impact the resulting aerodynamic values. To address this, a brief investigation led to the selection of 3D laser scanning as the most suitable compromise between precision and economic viability. The task of 3D laser scanning was outsourced to an external consultant. The service provider's precision specifications guaranteed an error of less than $0.02mm$, well within the construction tolerances.

The outcomes of this scanning effort yielded both a mesh and a mathematical model for each component, encompassing the mainfoil, tail, fuselage, and strut. The latter format proved to be the most practical for subsequent processing. On the other hand, *iges* files were composed of thousands of elementary surfaces, resulting cumbersome.

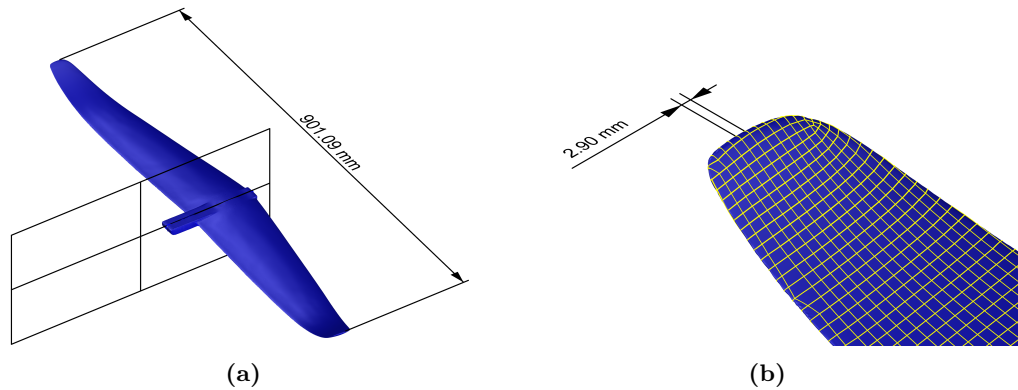


Figure 7: Original mainfoil *iges* model made of 7474 surfaces (a) and a close-up of the mainfoil tip and elementary surfaces dimensions (b).

To streamline management and facilitate further analysis, new files were created with *Rhinoceros* [6], a *McNeel* CAD software, with each element represented by a limited number of NURBS surfaces. The procedure to draw the three wings, meaning mainfoil, tail and strut, started duplicating the leading and trailing edges. This has been possible assuming that the deviations between the vertical tangent points loci and the real leading edges were negligible. This assumption was substantiated by the minimal geometric rake of the sections, which were $+2^\circ$, -2° and 0° for mainfoil, tail and strut respectively. This helped to automatise the duplication process. To individuate the trailing edge, instead, it was just necessary to identify the discontinuity between lower and upper surfaces.

Subsequently, the sections were produced just intersecting the geometries with a vertical plane, which was positioned at defined intervals along the spanwise axis.

The result of this process has been a set of curves as complex as the input polysurfaces. Thanks to an automated command these curves could be further refined by specifying the number of control points and the degree needed to accurately describe the output, while always considering the offset from the input.

Following this stage, the original polysurfaces have been replicated as the sweep given two binaries and an arbitrary number of sections. A correct rebuilding of geometries is often necessary to improve the quality of subsequent steps such as meshing and, consequently, the analysis. Moreover, it is a chance to make any necessary adjustments based on the specific objectives of the CAD model, such as tailoring the training edge for files intended for CFD simulations.

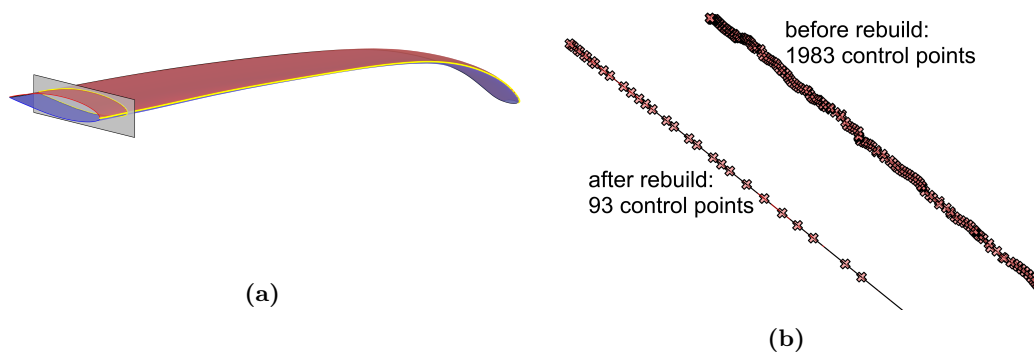


Figure 8: Edge and sections duplication process (a), and input and output of the curve rebuilding process (b).

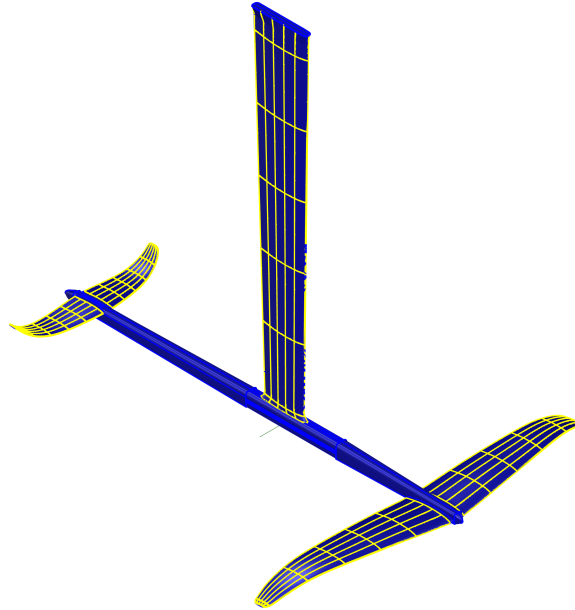


Figure 9: Final results of hydrodynamic surfaces scanning and rebuilding.

3.2 Board geometric survey

The Board geometric survey has been faced manually because of the simple lines and the great dimensions. The procedure exploits the physical individual made available by FIV and graphic material found on the web. The production of a 3D model starting from the orthogonal views without any dimensions has been possible thanks to the chance of measuring any detail on the real board with a measuring stick and a caliber. The cleanliness of the results has been a goal of the process in this case too.

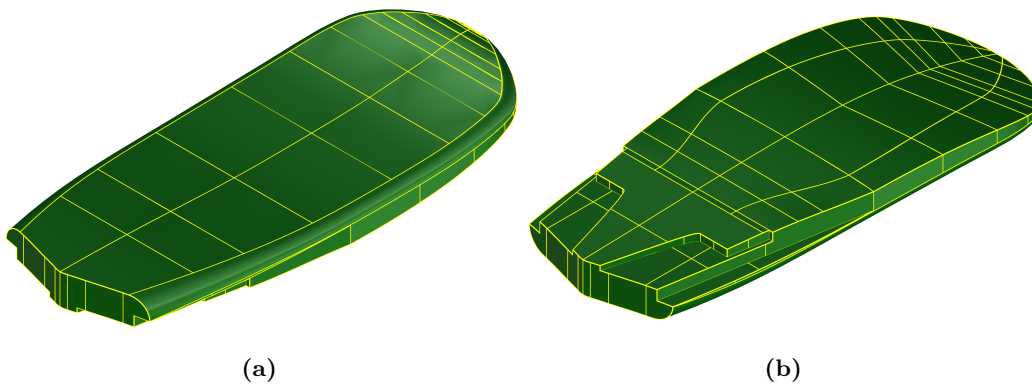


Figure 10: Board upper (a) and lower (b) surfaces.

3.3 Other components CAD models

A few words must be spent about components such as sail, mast, boom and athlete. For the first three, the rough assumption of 2D planar geometry or curved beam has been made. The reason for this is that just the mass distribution of these objects was relevant for the aim of this work, which had to be symmetrical too. The athlete CAD, on the other hand, was found on *Grabcad.com* [7] and the limbs position has been subsequently changed.

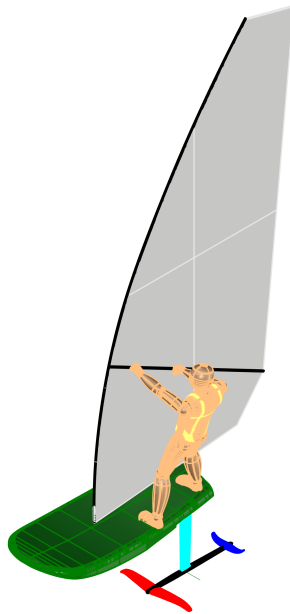


Figure 11: IQfoil assembly and athlete.

3.4 Centre of gravity measurement

The first output obtained after the CAD modelisation is the position of all components' centre of gravity. For a closed polysurface, *Rhino* can provide the centre of the volume. For some components, such as the foils, the assumption that they match with the centre of mass is weak. Although, those, such as mast and boom, which are composed of CFRP pipes equipped with steel and aluminium features, among which the mast step, cannot be considered homogeneous. This is the reason why each centre of gravity has been measured experimentally too. In this way two positions have been compared: one owed its uncertainty to the hypothesis made upstream to an affordable computation, the second to the hardship of the measuring process, even if its fundamental principles are strong.

The empirical search has been carried out constraining the object of analysis in a known point, such as fixing translation and allowing rotations around all axis. To another known point, a dynamometer has been connected. If the mass of the component is known too, it is

possible to determine the position of the centre of gravity with respect to one of the points starting from the percentage of weight sustained by the dynamometer.

$$\begin{aligned} F_{dyn}L &= Wx_{cg}; \\ x_{cg} &= F_{dyn}\frac{L}{W}; \end{aligned} \quad (1)$$

Where F_{dyn} is the load felt by the dynamometer, W is the total weight of the object, L is the distance between constrain and measure points, and x_{cg} is the mass centre position respect to the first one. The procedure has been repeated more times changing the constraint and measure points to test the method's reliability. The output has been compared with those of *Rhino* computation, validating those regarding mainfoil, fuselage, tail, strut, and board. For mast and boom the empirical results have been taken into account, while for sail and athlete, since they are effectively quasi-homogeneous and their CG could not be measured, its numerical location was the best option.

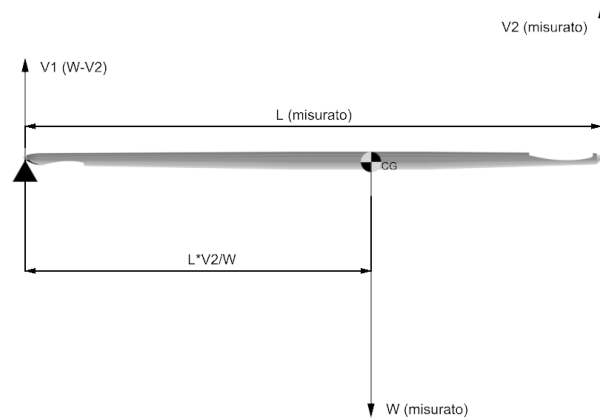


Figure 12: Synthetic scheme of the experimental centre of gravity method.

After that, the overall centre of gravity was needed, among all the reasons, to verify that the centre of gravity computed on *Matlab*[8] considering settings and athlete movements matched with that determined numerically. This precaution necessity is better explained in par. 7. Since *Rhino* calculated the volume centre only, a *Python* [9] script has been written so that, starting from the objects' geometry and their masses, it determined the centre of mass of each one and made the weighted average.

3.5 Effective rake measurement problem

During the *CICO* (*Campionato Italiano Classi Olimpiche*) events in Formia in November 2023, FIV's Coaches explained the issues due to the great tolerances in Starboard's foil production. Athletes perceived the differences between different mainfoils, tails and fuselages too, reason why they asked for a tool that could standardise the rakes' measurement in order to point out, for example, a curved fuselage.

Looking at foils it is possible to notice that they were laminated in closed mould and tip, leading and trailing edges were hand-refined after the polymerisation, so they are the features where the bigger errors were expected. Hence, the requested tool needed to firmly grasp the wings but without touching the hand-treated edges. Three key arrangements have been taken in the design phase:

1. The tool had to grab the foil above and below the leading edge;
2. It had to be large enough to dampen the difference between the CAD and each different individual;
3. It had to be easy to use by athletes and coaches;

On the other hand, the production has been entrusted to a 3D printing company which carried out the work for free ensuring a maximum tolerance of $0.1mm$. The output is shown in the figures below:

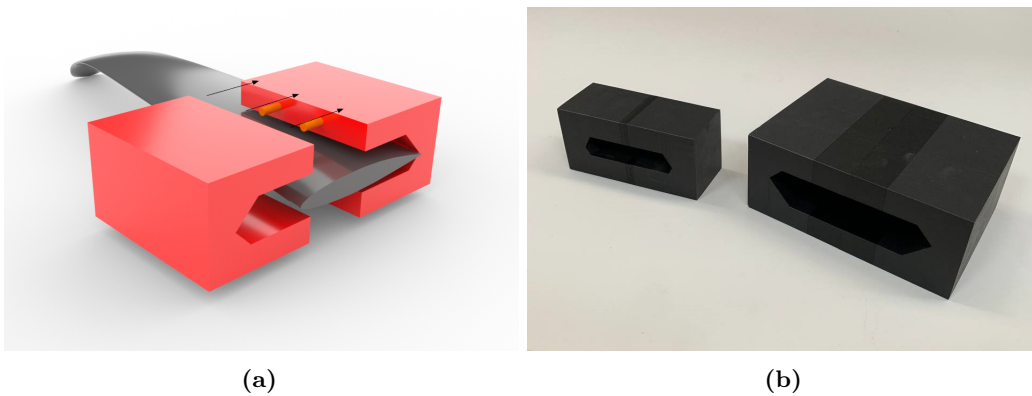


Figure 13: Mainfoil's rake measurement tool CAD (a) and the 3D printed prototypes (b).



Figure 14: Demonstration of mainfoil's tool at work.

In the next stage, three-dimensional wings have to be built. Measuring geometrical data on CAD files, it was possible to model mainfoil and tail, as in the following figure:

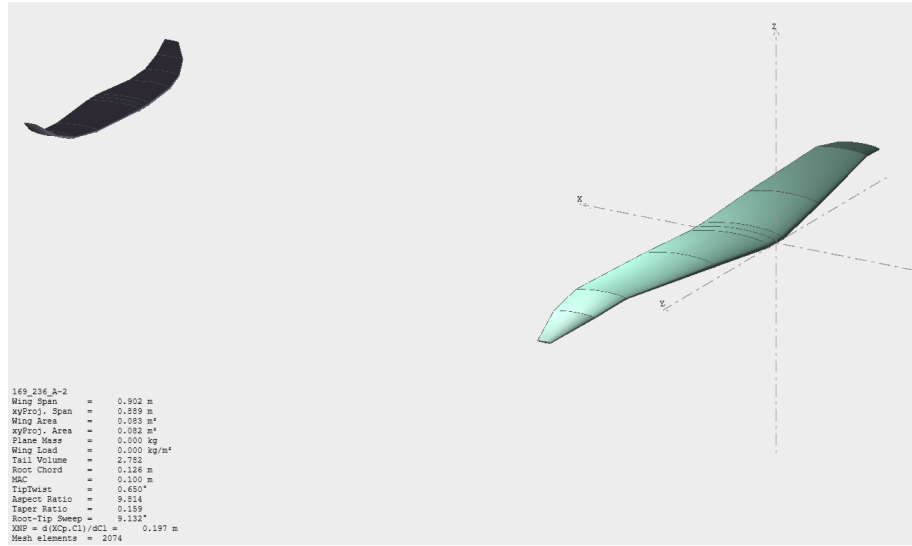


Figure 16: IQfoil's foils in XFLR5 environment.

4.1.2 XFLR5: analysis settings and results

Single wings and the whole plane have been analysed with the same settings. The ring vortex method was chosen method with the viscosity option checked on. The set boundaries conditions are:

- $V_\infty = 10\text{m/s}$;
- $\beta = 0^\circ$;
- $\rho = 1000\text{kg/m}^3$;
- $\nu = 8.8e^{-7}\text{m}^2/\text{s}$;
- $Mach = 0$ (incompressible flow);

The incidence range used to create polar graphs was $[-5^\circ; 7.5^\circ]$.

The subsequent figures report polar, CL/α , Cm/α and E/α for mainfoil, tail and whole plane. To better understand the graphs, it is necessary to specify that *XFLR5* used an inverted convention for tail CL.

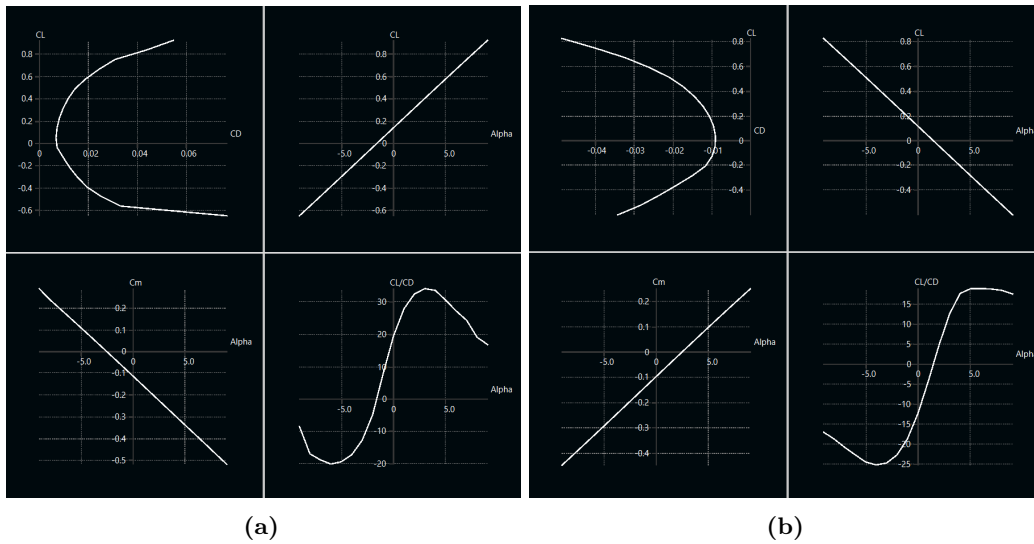


Figure 17: Mainfoil (a) and tail (b) polar graphs.

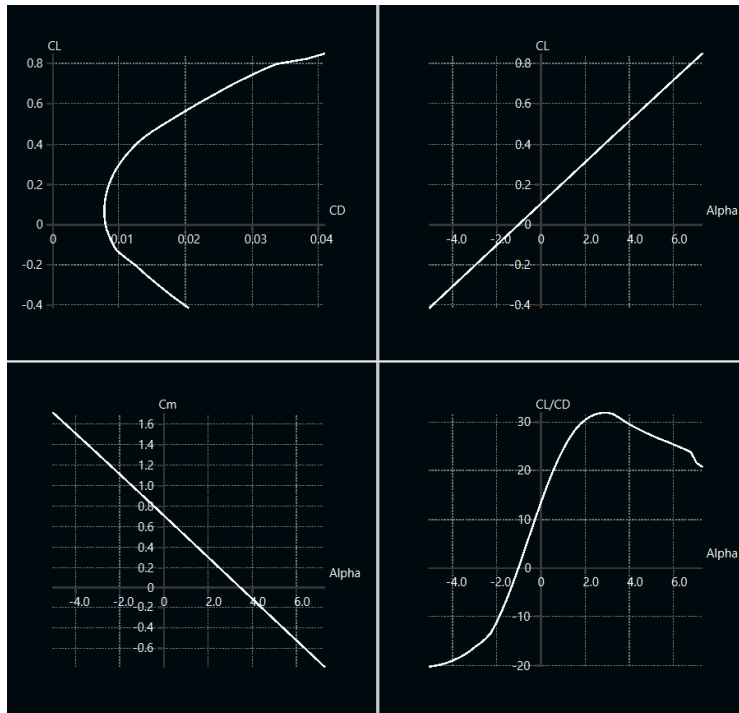


Figure 18: Whole foil polar graphs.

	Mainfoil	Tail (<i>Starboard's rake</i> = 2°)
$CL_{(\alpha = 0)}$	0.142	-0.115
CL_{α}	0.089	0.0793
$CD0$	0.0068	0.009
$\alpha_{(CL=0)}$	-1.60°	.45°

Table 1: Foil's aerodynamic derivatives and constant terms extrapolated from XFLR5 analysis.

Thanks to the data we collected, we were able to find the relationship between speed, tail rake, vertical hydrodynamic force and the relative pitch torque. Consequently, FIV Olympic coaches could choose the best foil setting in order to balance its pitching action at the highest possible speed. In addition, the graph shown to them and below reports how different tail rakes increase their effect on the equilibrium point at higher speeds.

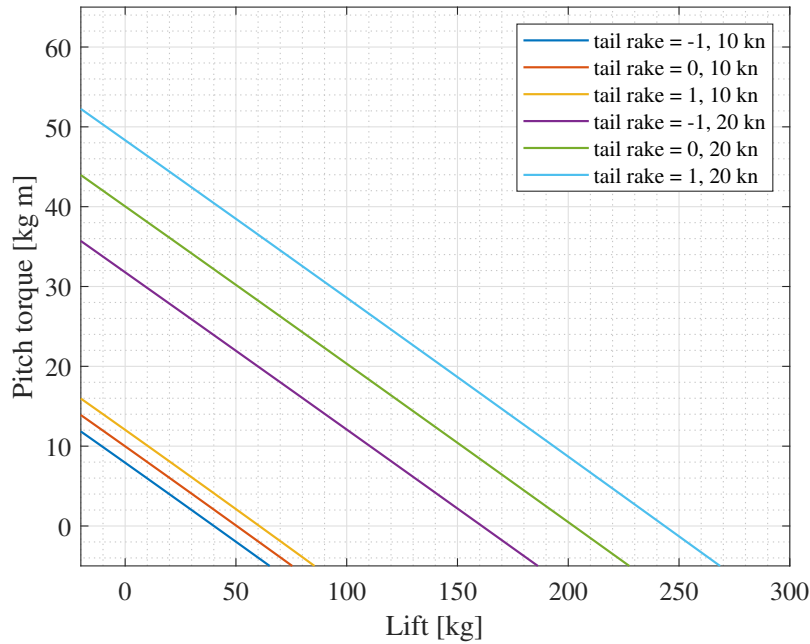


Figure 19: Pitch torque VS Lift force at different speed and for different tail rakes.

4.1.3 STAR CCM+: mesh

We carry out a more reliable in-depth CFD analysis using *STAR CCM+*. The input geometries are those treated in section 3. The first step to take is meshing them. Among the

precautions necessary to automatise the meshing process we emphasise the parametrization of all the default controls with respect to the base size and the introduction of two custom control to thicken the mesh around the training edges and to disable the prism layer option near the bottom surface of the numerical tank. Moreover, the parametrization of mesh settings allows to change the settings in a macro script.

To decrease computational effort, under the assumption of low sideslip, just half geometry was simulated.

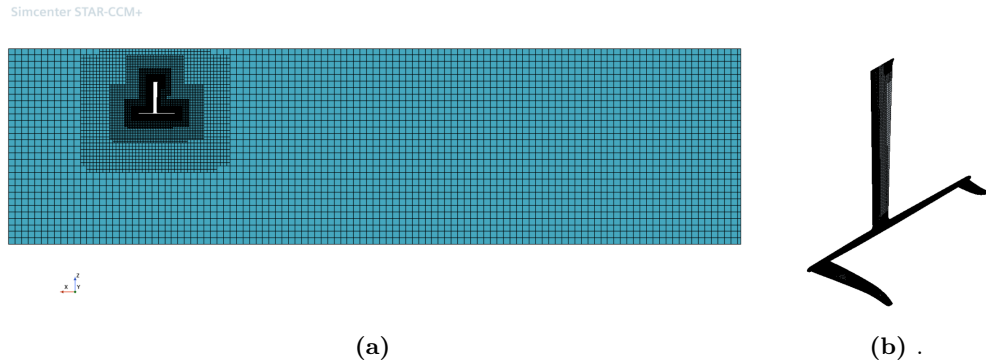


Figure 20: Foils whole mesh lateral (a) and around the components' (b) view.

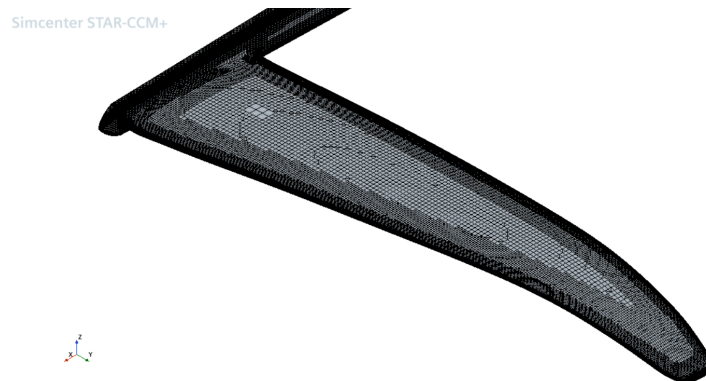


Figure 21: Close-up of the mesh around the mainfoil wall.

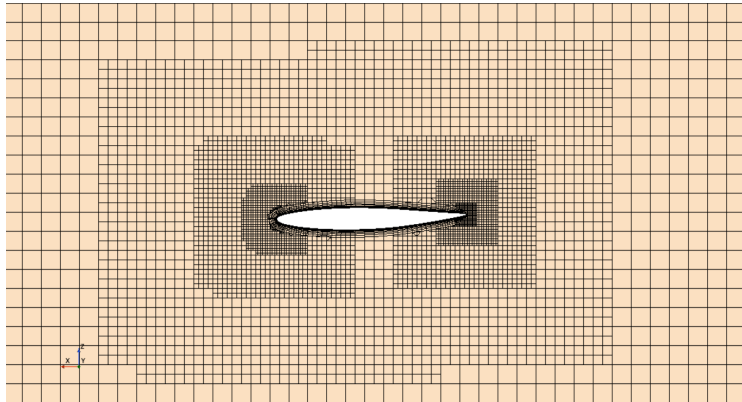


Figure 22: Close-up on the prism layer mesh around the tail wall.

4.1.4 STAR CCM+: analysis setting and results

The carried out analysis were steady and considering the density constant. Even though the strut works above and below the water free surface, just the liquid phase has been considered. To not compromise the results, we computed the strut coefficients considering just a portion far from its head.

For what it concerns the boundary regions, an explanatory scheme is reported below:

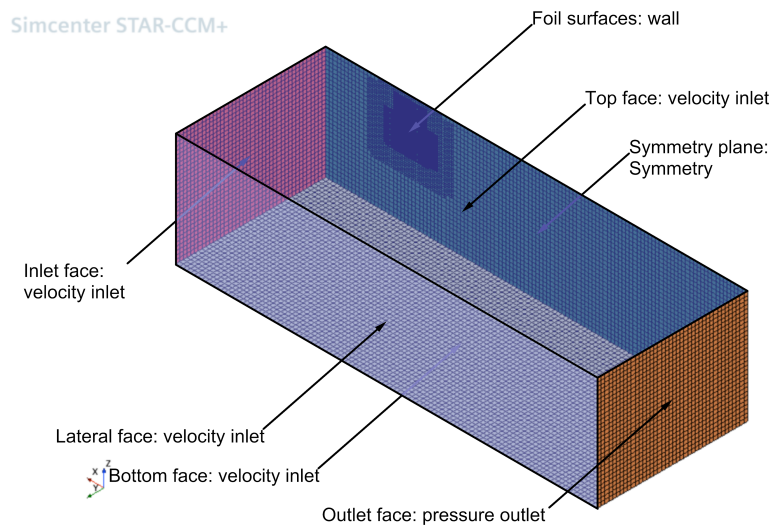


Figure 23: Foil simulation boundaries.

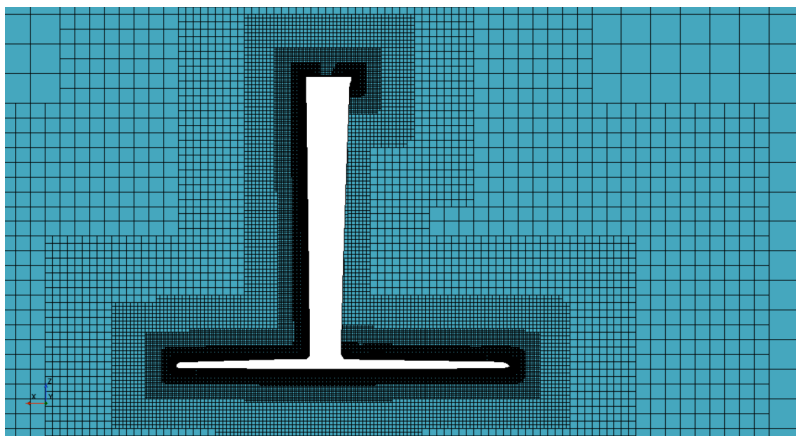


Figure 24: Foil mesh lateral view at 0° of incidence.

The latter two parameters to set were the water speed and the Attack angle. The first one has been set at $10m/s$, while the incidence is defined through a macro written in *Java* language. Additionally, the mesh base size too was changed in the macro, so that the convergence analysis could be made.

The aforementioned macro is a script compiled by the CFD software through which it is possible to automatise a command sequence. In this case, it was used for running a set of simulations that differed for a limited number of parameters. Therefore, two *for-cycle* which changed respectively α and the base size were implemented. At each iteration, the foil was rotated around the y-axis and the meshing operation was re-computed. After that, the CFD analysis was performed and various reports were printed on a *csv* file, which name identified the present case so that the data elaboration could be automatized. Among the printed report we notice:

mainfoil pitch torque	total lift
tail pitch torque	mainfoil drag
total pitch torque	tail drag
mainfoil lift	strut drag
tail lift	total drag

Table 2: Foil's requested reports.

Once simulations have been computed, we ordered the results in the *csv* files using *Matlab* [8]. Rough Data have been used to find aerodynamic derivatives and zero-lift angle of attack through linear or quadratic regression. Indeed, the output of this approximation

has the following form:

$$\begin{aligned} CL(\alpha) &= a_{0l} + a_{1l}\alpha; \\ CD(\alpha) &= a_{0d} + a_{1d}\alpha + a_{2d}\alpha^2; \\ CM(\alpha) &= a_{0m} + a_{1m}\alpha; \end{aligned} \quad (2)$$

The analytic form, whereas, is:

$$\begin{aligned} CL(\alpha) &= CL_{(\alpha=0)} + CL_{\alpha}\alpha; \\ CD(\alpha) &= CD0 + \frac{CL^2}{\pi e\lambda}; \\ CM(\alpha) &= CM0 + CM_{\alpha}\alpha; \end{aligned} \quad (3)$$

Hence it can be deduced that:

$$\begin{aligned} CL_{(\alpha=0)} &= a_{0l}; \\ CL_{\alpha}\alpha &= a_{1l}; \\ CD0 &= a_{0d} + \frac{CL_{(\alpha=0)}^2}{\pi e\lambda}; \\ CM_{(\alpha=0)} &= a_{0m}; \\ CM_{\alpha} &= a_{1m}; \\ \alpha_{(CL=0)} &= -\frac{a_{0l}}{a_{1l}}; \end{aligned} \quad (4)$$

	Mainfoil	Tail (<i>Starboard's</i> rake = 0)
$CL_{(\alpha=0)}$	0.110	-0.209
CL_{α}	0.0659	0.0497
$CD0$	0.007230	0.0101
$CM_{(\alpha=0)}$	0.0948	0.236
CM_{α}	0.0607	-0.0554
$\alpha_{(CL=0)}$	-1.66°	4.21°

Table 3: Foil's aerodynamic derivatives and constant terms extrapolated from CFDs.

In the following figures, the graphs concerning mainfoil and tail obtained through the simulations and the regressions are compared. It has to be minded that the plotted CMs aren't focal moment coefficients, but the coefficients of the moment measured in the origin of the CFD reference system normalised by a $1m$. This choice is due to an ease and error minimisation motivation.

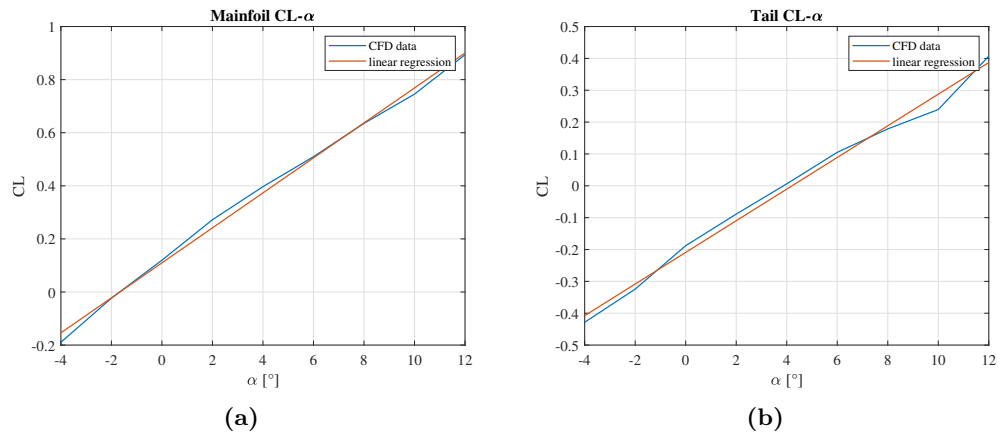


Figure 25: Comparison between CL from CFD simulations and the relative regression for the mainfoil (a) and for the tail (b).

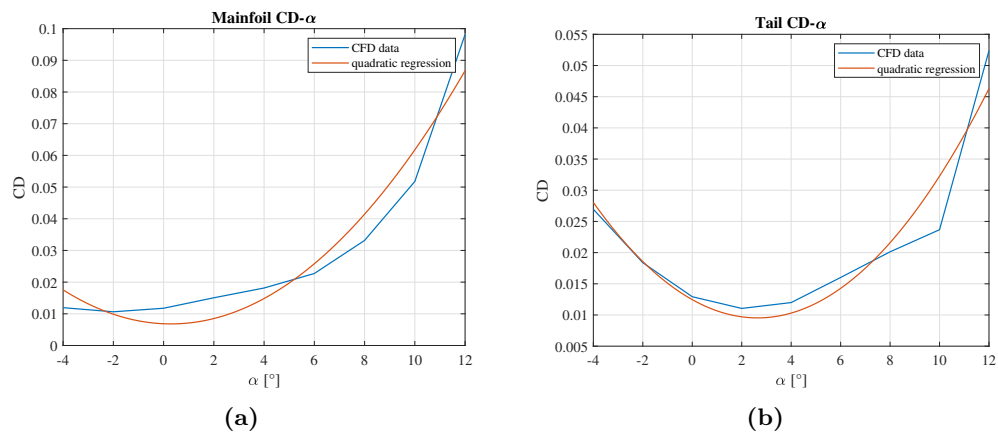


Figure 26: Comparison between CD from CFD simulations and the relative regression for the mainfoil (a) and for the tail (b).

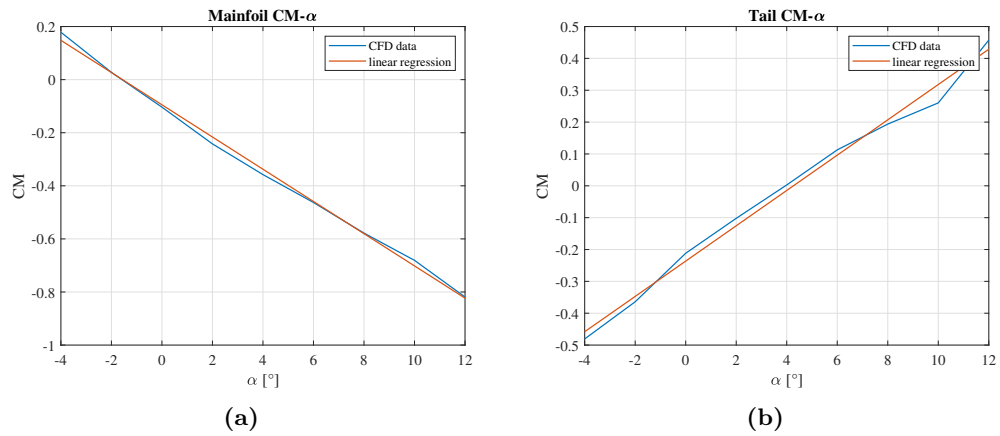


Figure 27: Comparison between CM from CFD simulations and the relative regression for the mainfoil (a) and for the tail (b).

In conclusion, some *STAR CCM+* scenes which shows pressure and velocity fields are reported.

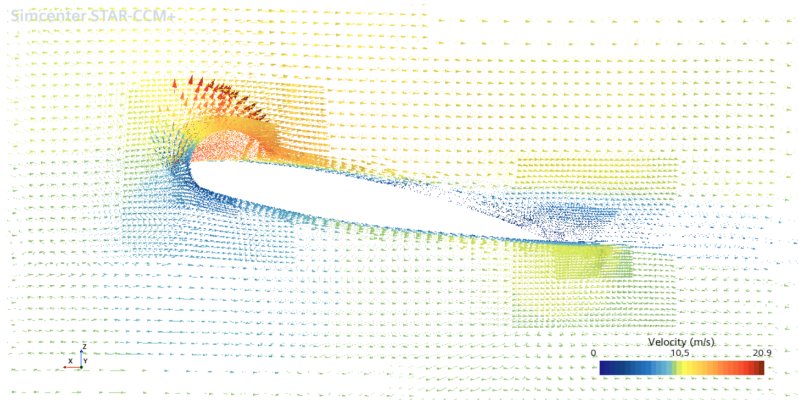


Figure 28: Close-up of velocity field around the mainfoil.

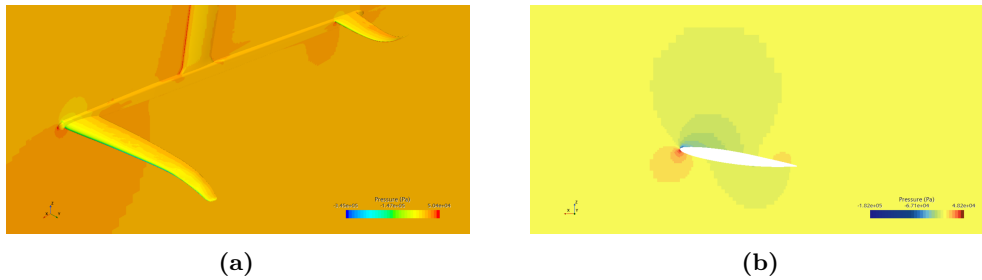


Figure 29: Pressure field around the foil (a) and a close up around the tail (b).

4.1.5 STAR CCM+ and XFLR5: results comparison and conclusion

Looking at graphs in figures 17a,17b,25a,25b,26a, and 26b, a great significant disparity becomes evident. In particular, the main foil exhibits less lift and more drag than what was estimated by the VLM (Vortex-Lattice Method). Nevertheless, the most relevant differences are noticed when considering the tail. The CFD method is more reliable for this application, so its results will be taken into account in subsequent sections. Nonetheless, it is important to understand the source of such a great error in XFLR5 estimations.

First and foremost, we must consider that XFLR5 operates at low Reynolds numbers, primarily due to its inability to consider turbulence effects on three-dimensional wings [11], while this foil operates at over $Re = 1.5 \cdot 10^6$. Moreover, the panels which discretise the surfaces are flats [11]. Although, taking four points on two parallel cords and two spanwise isocurves, the distance between one among them is often far from the plane identified by the other three. This is caused by the strong irregularity of the dihedral angle in function of the spanwise coordinate. Another noteworthy point concerns the taper sharp of the wings. Indeed, the vortex-lattice method appears more reliable on wings with a low taper ratio[14]. At last, in XFLR5, the wake is modeled as a straight extension of flat panels or vortex lines behind the wing's trailing edge, without accounting for the *wake roll up*. The consequences encompass an overestimation of the lift and an underestimation of the induced drag for the stand-alone wing. Furthermore, this phenomenon can lead to an unwanted numerical interaction between mainfoil and tail [11], warranting the greater error detected on the latter's values.

4.2 Board

The board was a much more complex component to study because of the environment where it worked. The airflow direction, indeed, could differ a lot from 0° with respect to the longitudinal axis. For this reason, it became necessary to express its coefficients in function of attack angle, apparent wind angle and roll angle. In addition, its shape could not be assimilated to a wing. Only CFD simulations have, afterward, been conducted and, once again, the work exploited the chance of using a macro script.

4.2.1 STAR CMM+: mesh and analysis setting

Simulations were steady and considering the density constant this time too. The modeled fluid was the air this time, but the Mach number was small enough to consider the flow incompressible. Setting customs controls, it was necessary to consider the automatic rotation the board would perform. Hence a volume bigger than usual has been predisposed for a mesh refinement.

For what it concerns the boundary regions, an explanatory scheme is reported below:

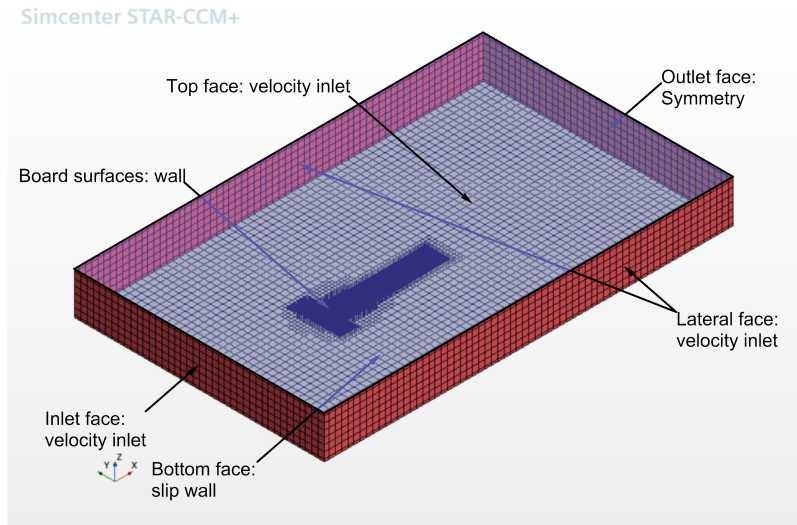


Figure 30: Board simulation boundaries.

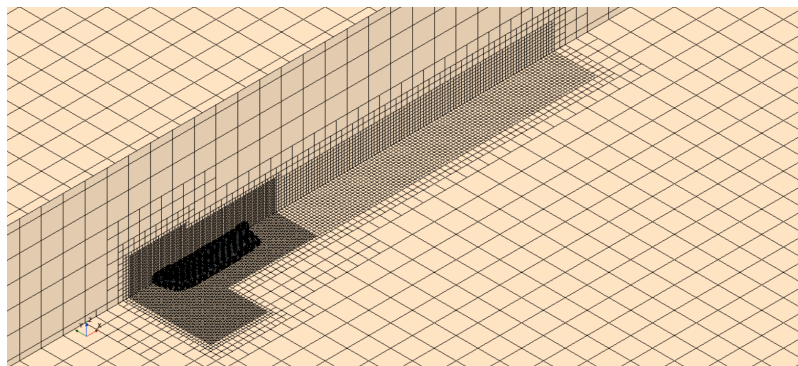


Figure 31: Mesh for board aerodynamic simulation.

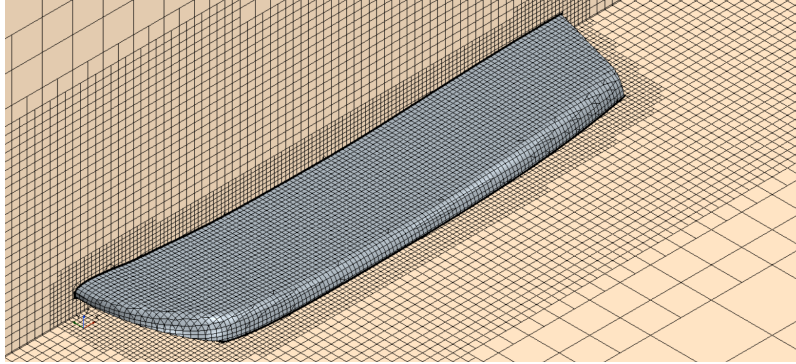


Figure 32: Close-up of the mesh around the board.

The orientation of the board in the tank was imposed through the macro, which was composed of four *for-cycle* which change α , AWA , ϕ plus the base size allowing a following convergence analysis.

The requested reports at each iteration of the script were:

pitch torque
 lift
 total drag
 longitudinal drag
 transversal drag

Table 4: Board's required reports.

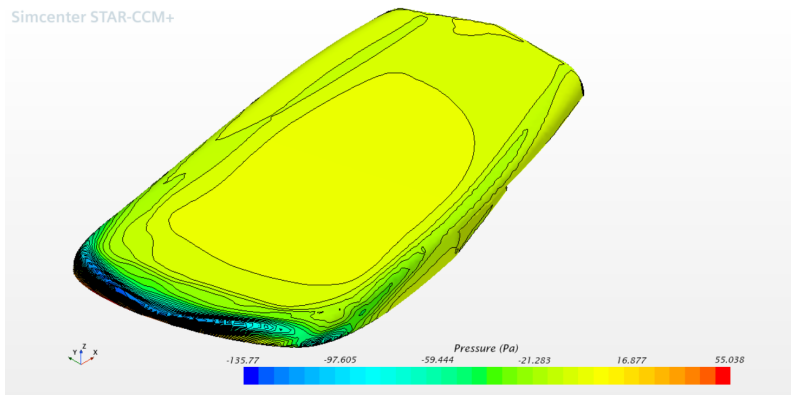


Figure 33: Pressure field on the board.

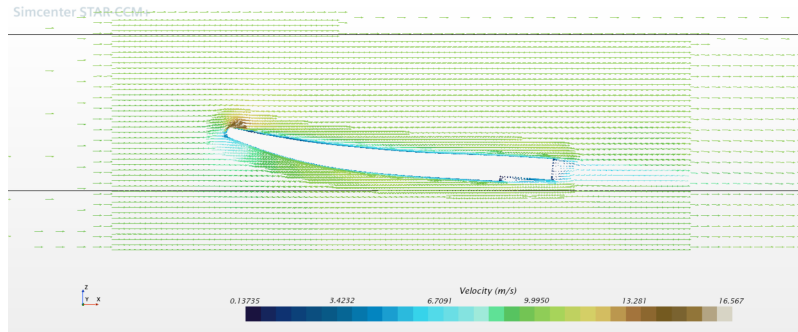


Figure 35: Velocity field around the board.

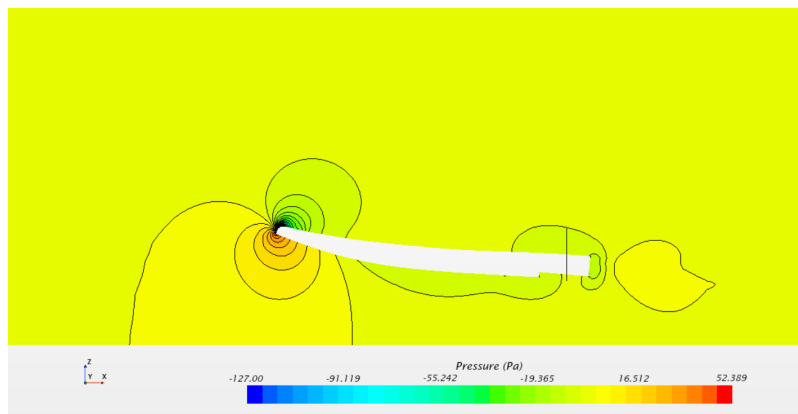


Figure 34: Pressure field near the board.

4.2.2 STAR CMM+: results

The raw data collected through the analysis were treated likewise those of the foil. The most relevant difference lay in the multidimensionality of the problem, reason why the *polyfitn toolbox* was used: it computes a multidimensional polynomial regression via the least square method the same way as *polyfit* command.

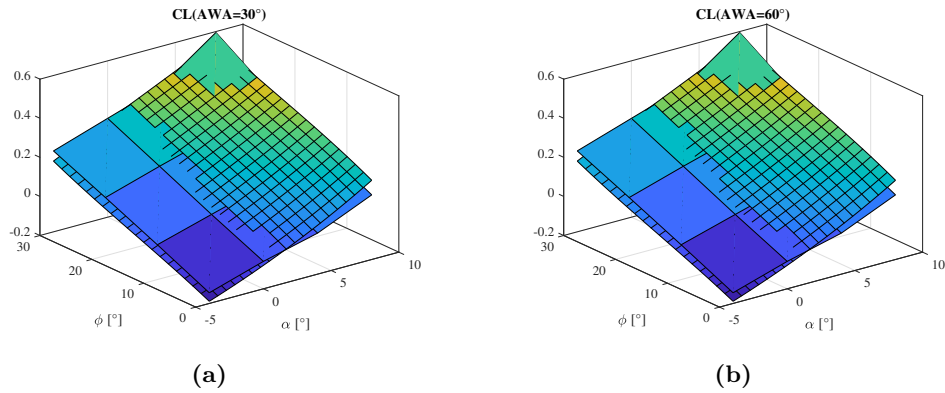


Figure 36: Comparison between CFD results and the implemented regression for $CL(AWA = 30^\circ)$ (36a) and $CL(AWA = 60^\circ)$ (36b).

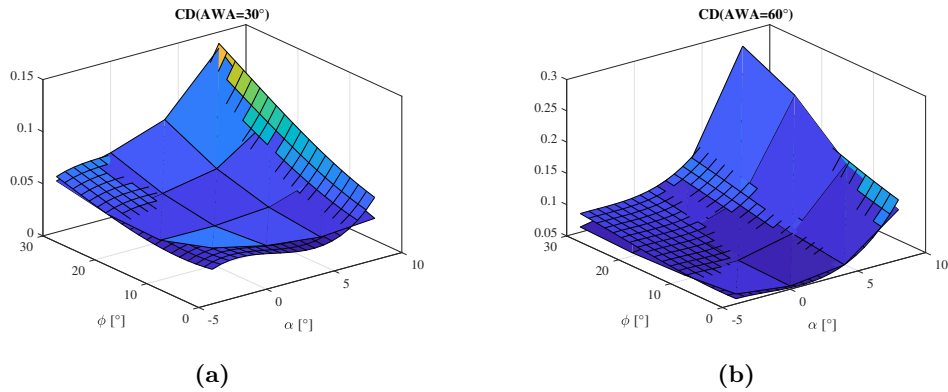


Figure 37: Comparison between CFD results and the implemented regression for $CD(AWA = 30^\circ)$ (a) and $CD(AWA = 60^\circ)$ (b).

4.3 STAR CCM+: convergence analysis

To qualify the reported work, the convergence analysis was carried out on both the study objects. As already mentioned, for each simulation three meshes were computed with different base sizes, more precisely, related by a constant factor. For the foil, indeed, they were 100, 150 and 225, while for the board they were 1.1, 2.2 and 4.4.

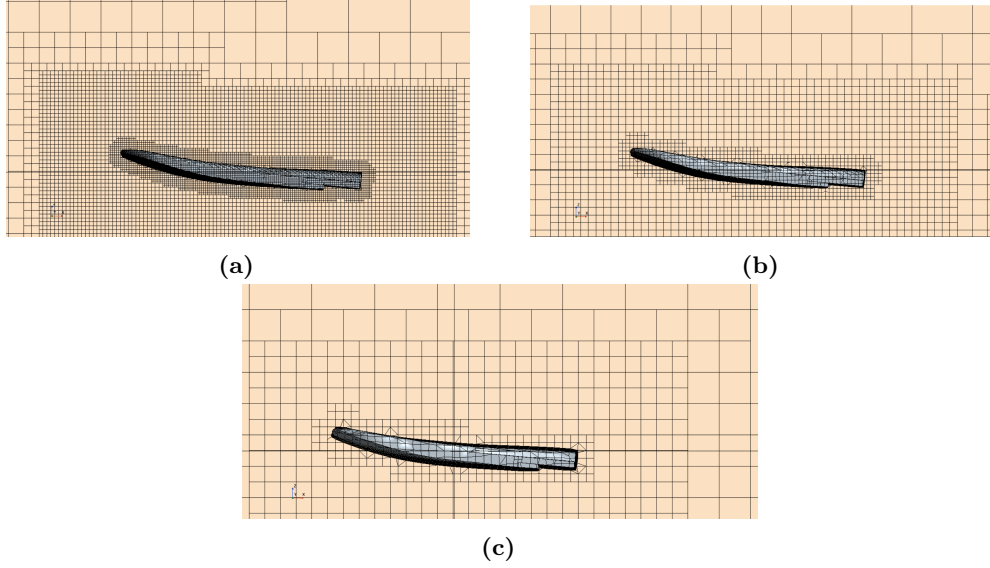


Figure 38: Mesh for board simulation with base size 1.1 (a), 2.2 (b) and 4.4 (c).

Since we would estimate the discretization error, we would refer to following equation:

$$\varepsilon_h^d \sim \alpha h^p + H; \quad (5)$$

Where ε_h^d is the error between the real solution and the one of the discretized problem, α is a term that depends on the derivatives at the given point, but it is independent of mesh size h and H stands for higher order terms. At last, p is the convergence order, which is often an indicator of solution quality. However, its estimation assumes that the terms in H are much smaller than the previous ones as their orders increase. This condition can be ensured only if the convergence is monotonic and the solution is smooth, excluding turbulent flows[15]. The latter hypothesis is evidently not verified.

Nonetheless, a different equation can be used to estimate the error [16]:

$$\begin{aligned} \varepsilon_\phi &\sim \delta_1 = \phi_i - \phi_0 = \alpha h_i; \\ \varepsilon_\phi &\sim \delta_2 = \phi_i - \phi_0 = \alpha h_i^2; \\ \varepsilon_\phi &\sim \delta_{12} = \phi_i - \phi_0 = \alpha_1 h_i + \alpha_2 h_i^2; \end{aligned} \quad (6)$$

Where ϕ_i is an interest function as determined using the i^{th} grid and ϕ_0 is the same quantity theoretical estimation. These three alternatives are only used if eq. 5 is not reliable, and, precisely, the first two are suitable for monotonically converging solutions, while the third can be used with non-monotonics ones. Following the present procedure for error estimation, the parameter p has to be determined:

$$\begin{aligned}
 p &= \frac{\ln(R)}{\ln(k)}; \\
 R &= \frac{\phi_h - \phi_{kh}}{\phi_{kh} - \phi_{k^2h}};
 \end{aligned}
 \tag{7}$$

R is a more intuitive parameter to hand with, as it is shown in the table:

Oscillatory Divergence	$R < -1$
Oscillatory convergence	$-1 < R < 0$
Monotonic convergence	$0 < R < 1$
Monotonic divergence	$R > 1$

Table 5: Convergence trend in function of R

For each component ϕ has been chosen as the most impacting quantity: the lift for the foil and the drag for the board.

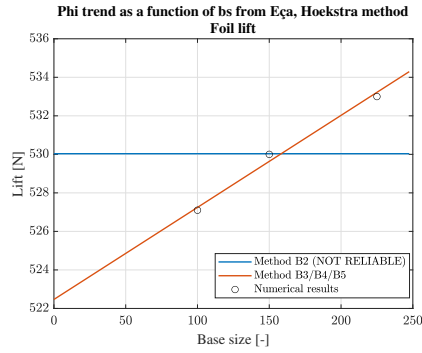
	p	R
Foil	0.084	0.97
Board	1.23	0.42

Table 6: p and R parameters for foil and board.

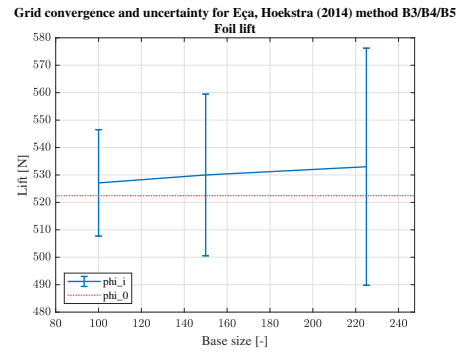
Hence, both simulation sets converge. To estimate the error and the uncertainty, an algorithm exploiting the least squares method and evaluating the standard deviation σ has been used [16]. In the subsequent table and graphs, the results are shown:

	Foil	Board
ϕ_i	527.1N	2.93N
ϕ_0	522.47N	2.43N
ε	4.8	0.49
Δ	19.4N	2.01N

Table 7: Error and uncertainty of foil and board analysis.

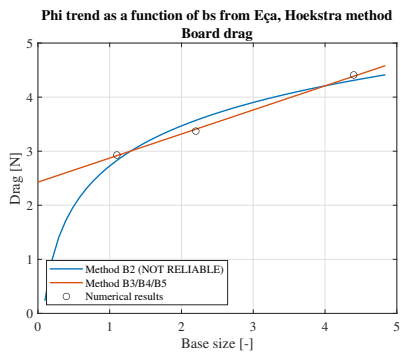


(a) Error on foil lift.

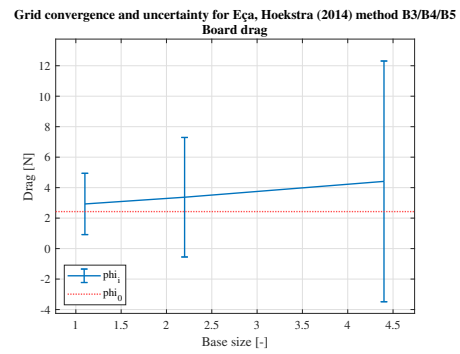


(b) Uncertainty on foil lift.

Figure 39: Error (a) and uncertainty (b) on foil lift.



(a)



(b)

Figure 40: Error (a) and uncertainty (b) on board drag.

5 3DOF static model

In the 3DOF static model, the longitudinal mechanics is analysed. In particular longitudinal, vertical and pitch degrees of freedom are considered. Ignoring the lateral-directional mechanics removes the necessity of a sail model, but it prevents to study of the degrees of freedoms' coupling. This tool has been developed according to FIV's necessities and requests. Moreover, it represents the first step for a more complete model.

5.1 Structure

The 3DOF static model has been written on *Matlab* and it is composed by two principal files: the main and the core. The main is that script which contains the user interface, call the solver in order to find the equilibrium points and, if necessary, print graphs and results. The core is called *3DOF_static_model* and asks the independent variables α , sail trust and athlete's centre of gravity longitudinal position, implements the physics of the problem and returns the resultants, which must be zero. In the following flow-chart can be noticed the principal step of the model and in the following paragraphs will be explained.

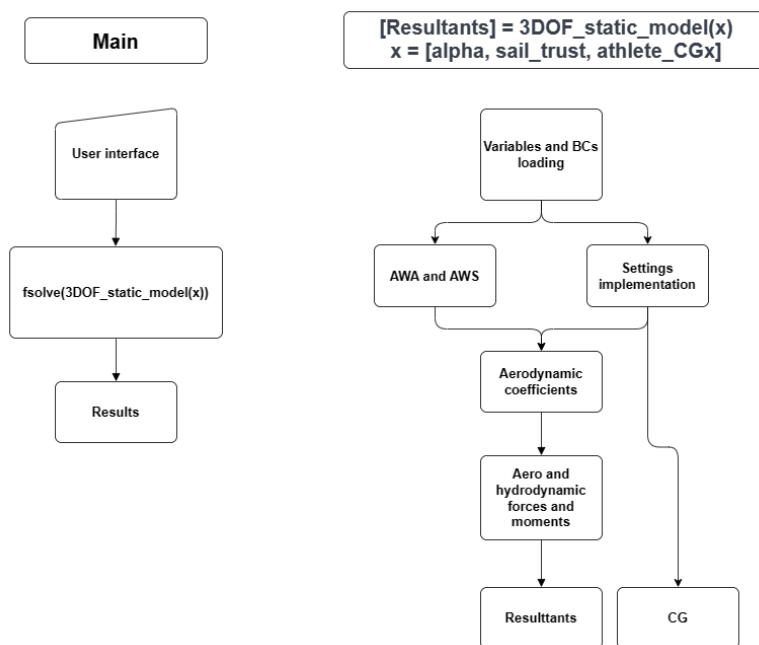


Figure 41: 3DOF static model structure.

5.2 Regulations and controls

The regulations studied in this work are tail and board rakes. Both have aerodynamic consequences, reason why they are summed to the incidence before the relative coefficients interpolation. To simplify the interface, the tail rake has to be given in *Starboard* convention, so it is converted in the CFD's one immediately after the variables loading.

Since the board rake has a more important geometrical effect, it has to be considered in the forces arms calculation. To model it, a rigid rotation is performed for all components above the boards, that are sail, mast, boom, sailor and the board itself. This causes a non negligible centre of gravity displacement. The rotation is implemented through matrix product, for example:

$$CG_{comp.} = \begin{bmatrix} \cos(i_b) & 0 & \sin(i_b) \\ 0 & 1 & 0 \\ -\sin(i_b) & 0 & \cos(i_b) \end{bmatrix} (CG0_{comp.} - O_r) + O_r \quad (8)$$

Where i_b is the board rake, $CG0_{comp.}$ and $CG_{comp.}$ are the centre of gravity of a generic component before and after the rotation and O_r is the centre of rotation placed in the strut cassette.

For what it concerns the controls, the only one which operates in this model is the longitudinal position of the athlete and it is a dependent variable of the model.

5.3 Magnitude and angle of the airflow

Given that there are two wind reference systems, the one defined by the water flow on the foil will be adopted. The air flow reference system has however to be defined so that board aerodynamic coefficients can be determined. Wind speed and angle respect a fixed reference system, ex. a shut down dinghy, will be called *TRUE* or *TWS* and *TWA*. The perceived wind speed and angle, instead, will named *APPARENT* or *AWS* and *AWA*.

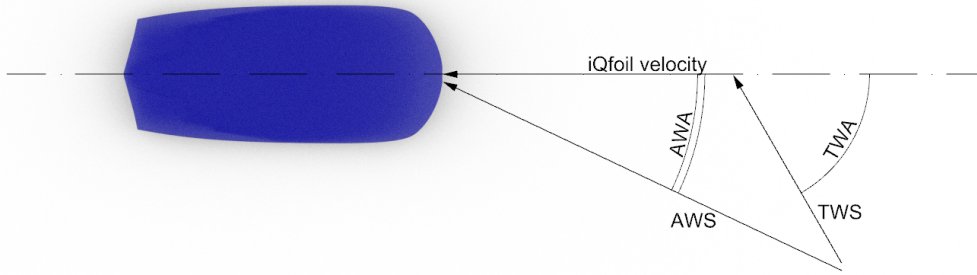


Figure 42: True and apparent wind.

As it can be deduced from the previous figure, the apparent wind speed and angle can be calculated as it follow:

$$\begin{aligned} AWS &= \sqrt{(TWS \sin(TWA))^2 + (TWS \cos(TWA) + U)^2}; \\ AWA &= \operatorname{atg} \left(\frac{TWS \sin(TWA)}{TWS \cos(TWA) + U} \right); \end{aligned} \quad (9)$$

5.4 Equilibrium equations

At this point it is possible to write the non-linear equilibrium system:

$$\tau = \begin{Bmatrix} F_x \\ F_z \\ M_y \end{Bmatrix} = 0 \quad (10)$$

$$\begin{cases} F_x = T_{sail} + D_{aero} \cos(AWA) + D_{hydro} \\ F_z = W + L_{board} + L_{hydro} \\ M_y = T_{sail} z_{sail} + W_{iQ} x_{iQ} + W_{ath} x_{ath} + \sum_{aero} (D_i z_i \cos(AWA)) + \sum_{hydro} (M_i) \end{cases} \quad (11)$$

Where T_{sail} is determined so as to ensure that $F_x = 0$, while the other fluidynamic forces and moment can be calculated as:

$$\begin{aligned}
 F_i &= \frac{1}{2} \rho V^2 S C_F \\
 M_i &= \frac{1}{2} \rho V^2 S C_{Mc}
 \end{aligned}
 \tag{12}$$

The fluidynamic force and moment coefficients are reported in the following table with the relative coefficients source and dependencies.

	source	CL	CD	CM
Mainfoil	CFD	α	α	α
Tail	CFD	α	α	α
Strut	CFD	0	const.	0
Board	CFD	AWA, α , ϕ	AWA, α , ϕ	AWA, α , ϕ
Athlete	Bib.	0	const	0

Table 8: Aerodynamics coefficients dependencies and sources.

As it can be noticed in eq. 11, hydrodynamic lift and drag moments are embedded with the focal moments in the M_i terms. This is a consequence of the overlap between the foil CFD model and static model reference systems, reason why the relative reports include all the components. In order to reduce the interpolation error the focal moment coefficients have been found, but not used in this context.

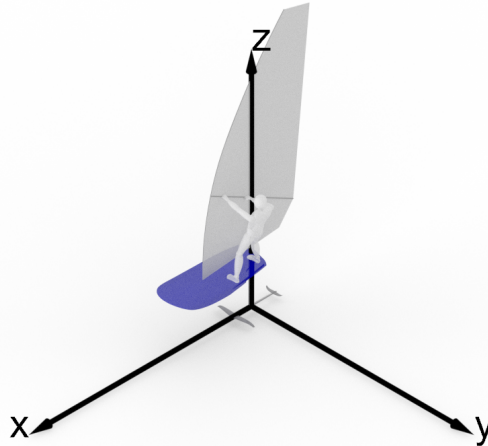


Figure 43: 3DOF model's reference system.

5.5 Results

The model described above has been used to provide to FIV's coaches a tailored consultancy. Specifically, they asked for a set of graphs which showed these trends:

- **iQfoil's speed VS athlete position along x-axis** for various **tail rakes**;
- **iQfoil's speed VS strut's drag** for various **flight height**
- **iQfoil's speed VS athlete position along x-axis** for various **flight heights**;
- **iQfoil's speed VS board's drag** for various **board rakes** when sailing **upwind, downwind** and **beam reaching**;
- **iQfoil's speed VS athlete position along x-axis** for various **board rakes** when sailing **downwind**.

In the following paragraphs these graphs will be reported.

5.5.1 tail rake's effects

In aeronautics, the tail's moving surface is used for pitch motion control. In this case, however, the tail rake has to be chosen on the ground and the primary control is entrusted to the athlete's longitudinal motion. Nevertheless, the tail rake maintains a deep impact on the longitudinal equilibrium. Indeed, by choosing its value, the athlete moves the zero of the control back or forward. This changes the outcome of the compromise between the manoeuvrability at higher or lower speeds, and, above all, increases or decreases the athlete's ability to react to overlifting phenomena.

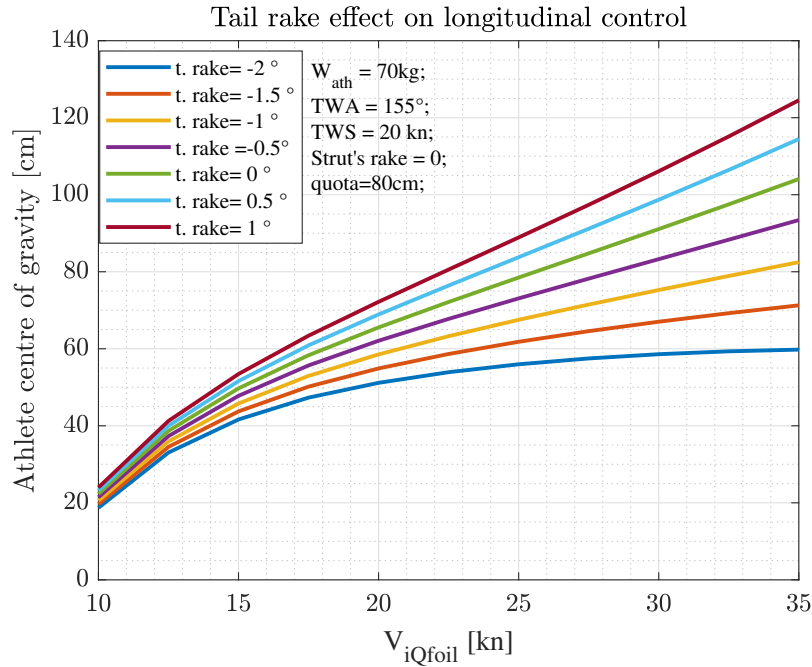


Figure 44: Tail rake effect on longitudinal control.

In the previous graph, the *Starboard* convention for tail rake is used. It shows that, by increasing the tail lift magnitude, the athlete must move his weight more forward. On the other hand, the $t.rake = -2^\circ$ curve, meaning the one with the greater tail incidence, presents a constant sign curvature, while the $t.rake = 1^\circ$'s one has a point of inflection. This implies that, for high speeds, the first requires the overall centre of gravity to overcome the neutral point, causing a static instability condition. The second curve, with the same boundary condition, requires the athlete to move his weight to an impossible position. Moreover, to find the optimum setting, low-speed conditions have to be considered too. In the same way, as at high speeds, an incorrect choice can lead the athlete to keep its weight too back or to an impossible position this time too. A heavy athlete, who can easily avoid the overlift but makes a greater effort at the take-off, will probably prefer a more raked tail. In contrast, the female athletes of Italian teams, who are lighter than male ones and than many of their stranger colleagues, will choose a less delifting tail, to reach higher speeds downwind.

The last consideration about this setting regards its implementation. *Starboard* provides seven angle spacers and each differs of 0.5° from the others. Hence, the feeling with the foil can change radically between two consecutive spacers. This issue will be resumed again, after the other graphs analysis.

5.5.2 Flight height effect

Another difference between planes and iQfoils flight mechanics lies in dependence of some loads, meaning the strut drag, on the flight height. In particular, its immersed surface varies linearly with it and, consequently, its centre of pressure. This causes some consequences on longitudinal and pitch equilibrium. The firsts are explained by the next graph:

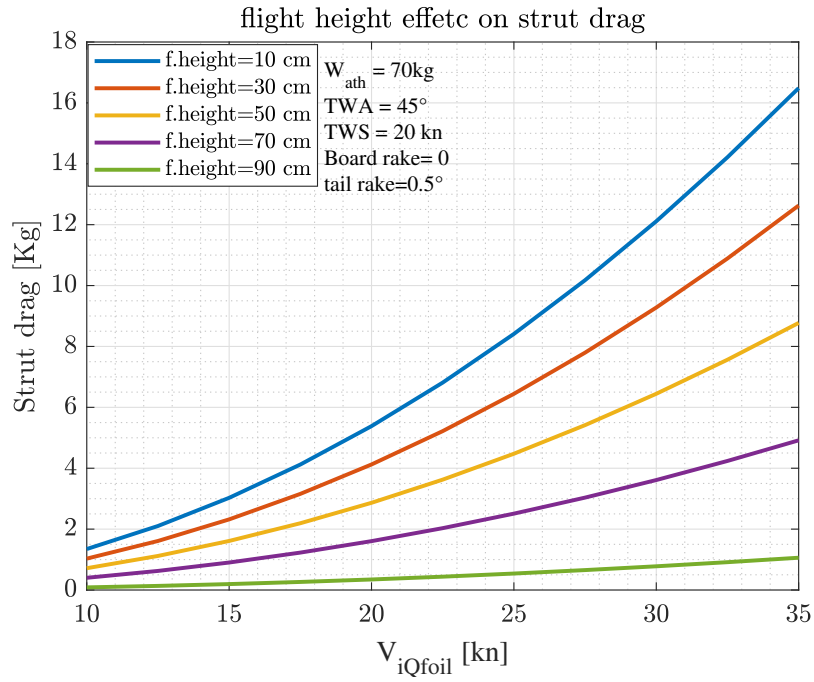


Figure 45: Flight height effect on strut drag.

Resuming the analogy with planes, the spatial distribution of the forces differs too. While planes aeroloads acts approximately at the same height, iQfoils' ones are distributed along the z axis, implying a pitch moment due to the sail trust and the aerodynamic drag of each component. If the strut drag and its application point vary, the relative pitch moment cannot be constant. This phenomenon is investigated below:

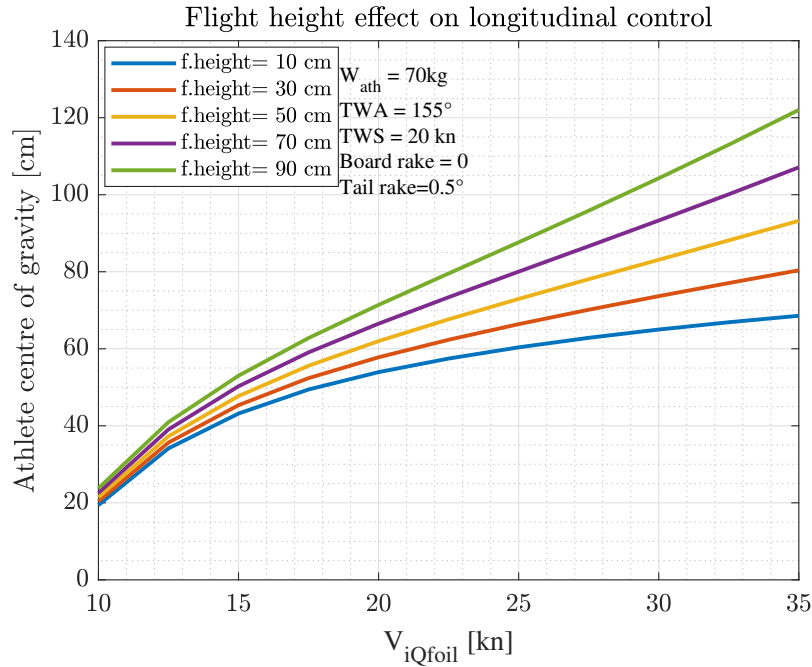


Figure 46: Flight height effect on strut drag.

In graph 45 and 46 we find the reasons for flying both high and low. As for tail rake, the better flight height for all the possible situations does not exist. However, in this case the investigated parameter can be changed during a race. For example, after a manoeuvre the major interest is to accelerate as fast as possible, reason why to reduce the overall drag is a priority. In this condition, flying high is advisable. At high speed, instead, the overlift issue must be considered this time too. When the effort of the athlete in keeping the foil pitched down becomes excessive, decrease the altitude can be a winning choice.

5.5.3 Board rake effect

Between the graphs requested by the coaches some concern the board's drag, which is almost negligible, as it can be noticed in chapter 4. However, their questions have been answered, first of all, plotting the drag for various board rakes and wind angles.

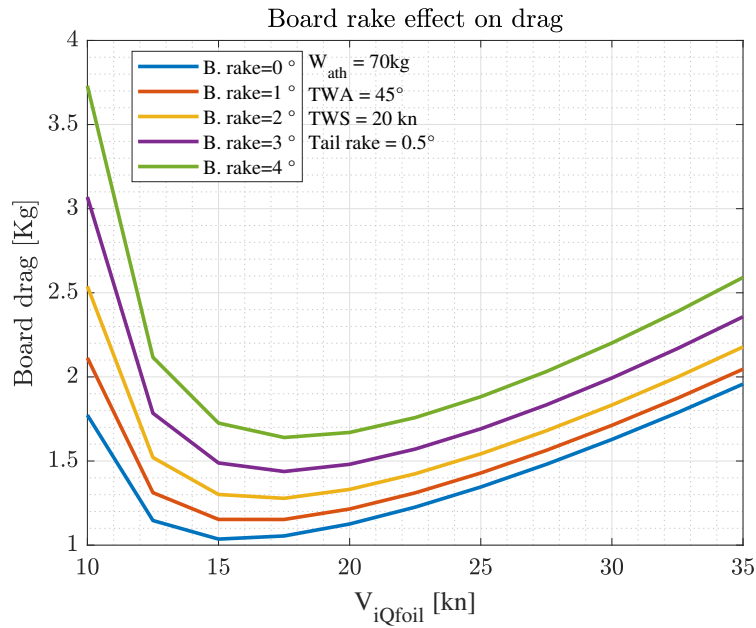


Figure 47: Board rake effect on drag when sailing upwind.

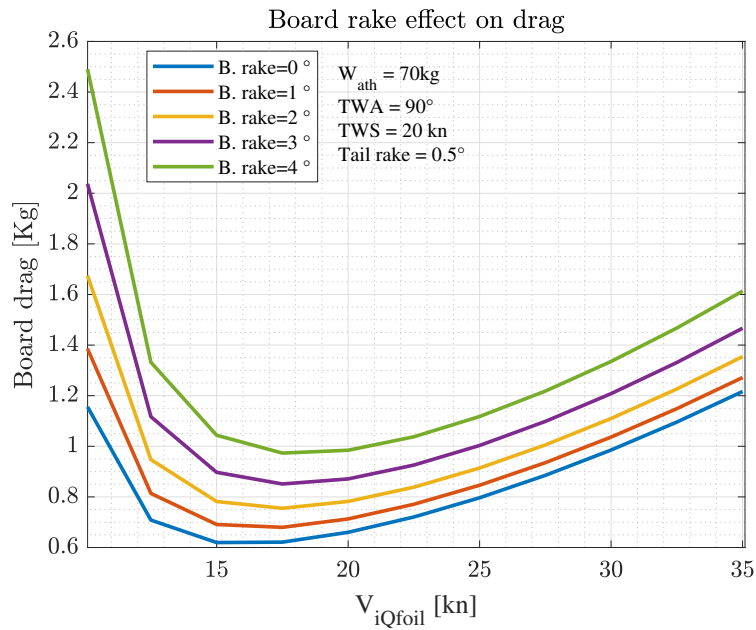


Figure 48: Board rake effect on drag when sailing beam reaching.

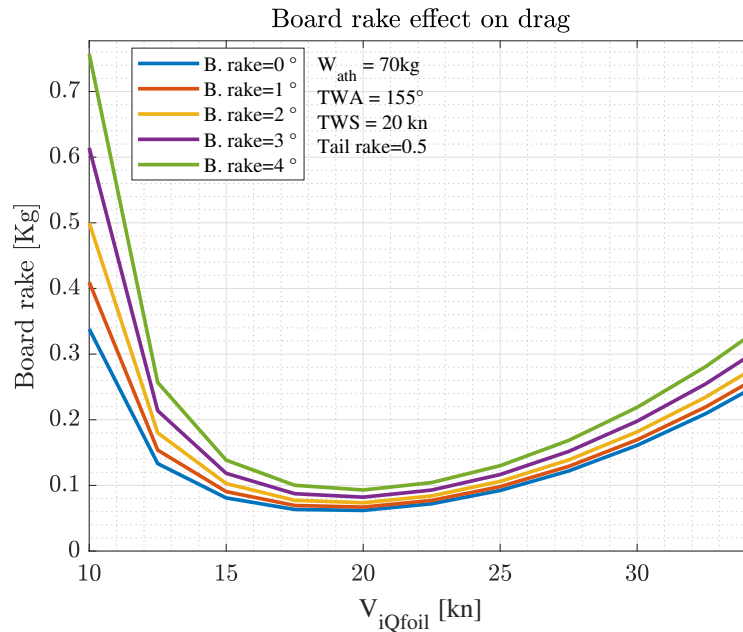


Figure 49: Board rake effect on drag when sailing downwind.

The most interesting thing in these graphs is the existence of a minimum of the drag module increasing the speed, a uncommon behavior in aeronautics. This trend is due to the relationship between the apparent wind speed and the iQfoil's one. For example, downwind the drag is less than one kilograms because the longitudinal component of wind velocity goes from the aft to the bow. When sailing upwind, instead, not only the drag is higher, but the board rake becomes much more impacting respect to the iQfoil speed and the minimum occurs before. This is due to the fact that, for very high flight velocity, the apparent wind angle tends to zero, becoming reducible to a wind tunnel situation. The closer the true wind angle is to zero, the smaller will be the difference between the ideal and the real case. If it were zero, the minimum would occur at zero knots.

For what it concerns the aims of the coaches, the next graph has been more relevant. Indeed, as it has been explained in chapter 2, the main effect of this setting is a geometrical modification of the system and, consequently, of all the forces' arms. In order to observe this aspect, the athlete longitudinal position has to be analysed again.

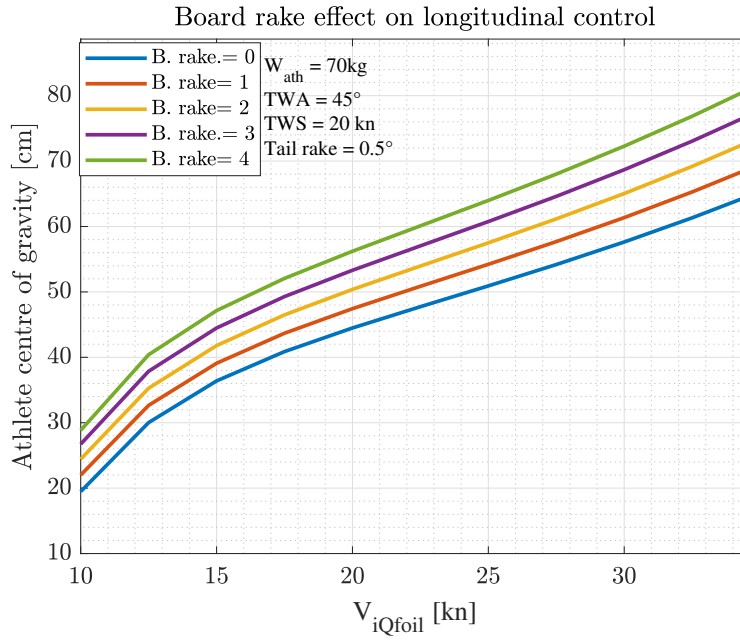


Figure 50: Board rake effect on longitudinal control when sailing upwind.

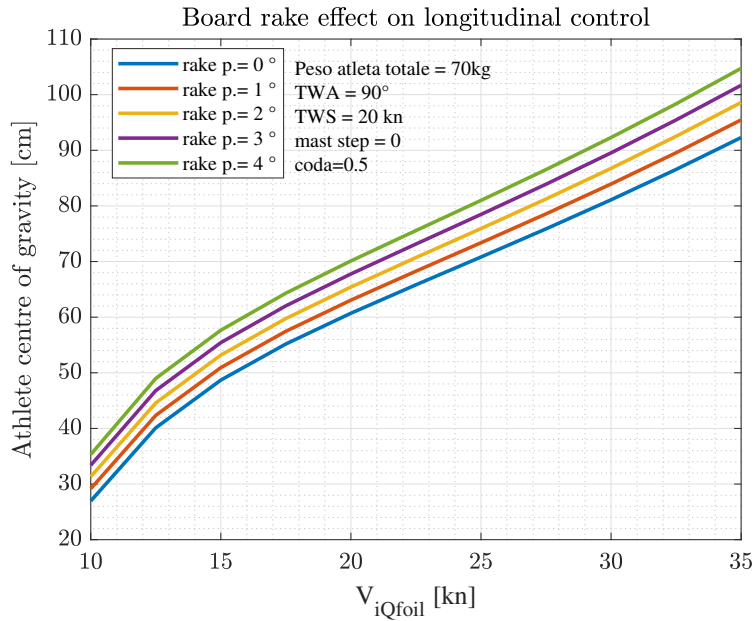


Figure 51: Board rake effect on longitudinal control when sailing beam reaching.

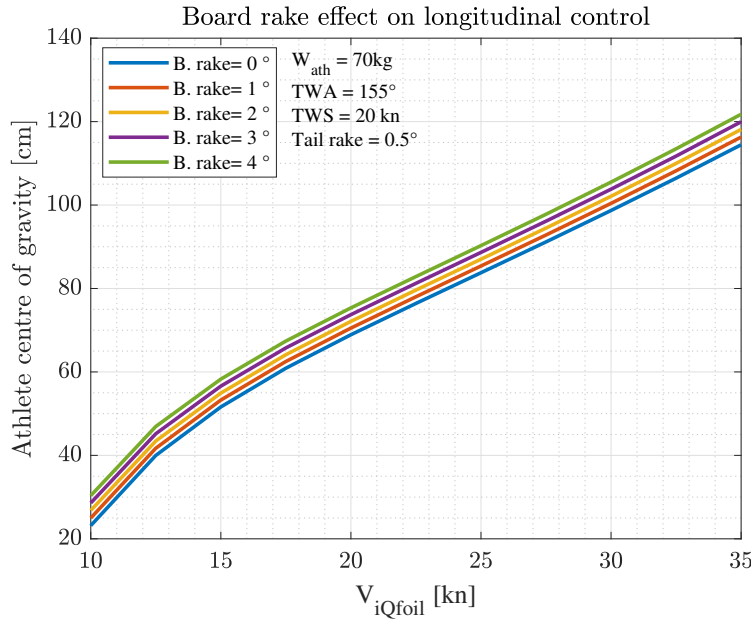


Figure 52: Board rake effect on longitudinal control when sailing downwind.

As it emerges, the more negative the rake is and the smaller is the effort required to the athlete. This effect has been felt by the Italian team already before of this analysis. When the board is pitched down respect to the foil, the centre of gravity of the higher components, meaning athlete, sail, boom and mast, is translated forward without any effort, with an observable advantage in the overlift control.

Because of its geometrical nature, this setting has the same impact for all the wind angles, but the three previous graphs are still different. The difference lies in the position of the athlete at the same velocity: when sailing downwind he must keep his weight forward. The cause is imputable to the aerodynamic drag and to the sail trust. Indeed, the latter has to be the sum of the first one and the foil drag, which is constant with the wind angle. So, when the wind angle is high, the board and the athlete's drags decrease and, with them, the sail trust. The moment produced by the sail pitches down the iQfoil, while the aerodynamic drags pitch it up. If the modules of the forces decrease, the more impacting consequences are imputable to the component with the longer arm from the overall centre of gravity, which is always the sail. This explains why the athlete effort increase with the wind angle.

In paragraph 5.5.1, while the tail rake effect was analysed, the macro-setting issue has been mentioned, meaning the plausible necessity of reaching an intermediate setting between

two consecutive angle spacers. The same problem does not arise when talking about the board rake or the flight height, which are micro-settings, because both they are continuous regulations and their effect is much smaller. This means that, with a correct combination of micro and macro settings, including straps and mast step positions, it is possible to reach many more compromises than using each setting separately.

Moreover, even if it should be obvious, the training sessions keep playing a fundamental role in increasing performance. Indeed, the more the athlete can control the flight height precisely, for example, the better he can exploit the consequences of a winning choice. If he appears inaccurate, instead, a good intuition can lead to clumsy results, such as a drastic deceleration or, worse, a touchdown.

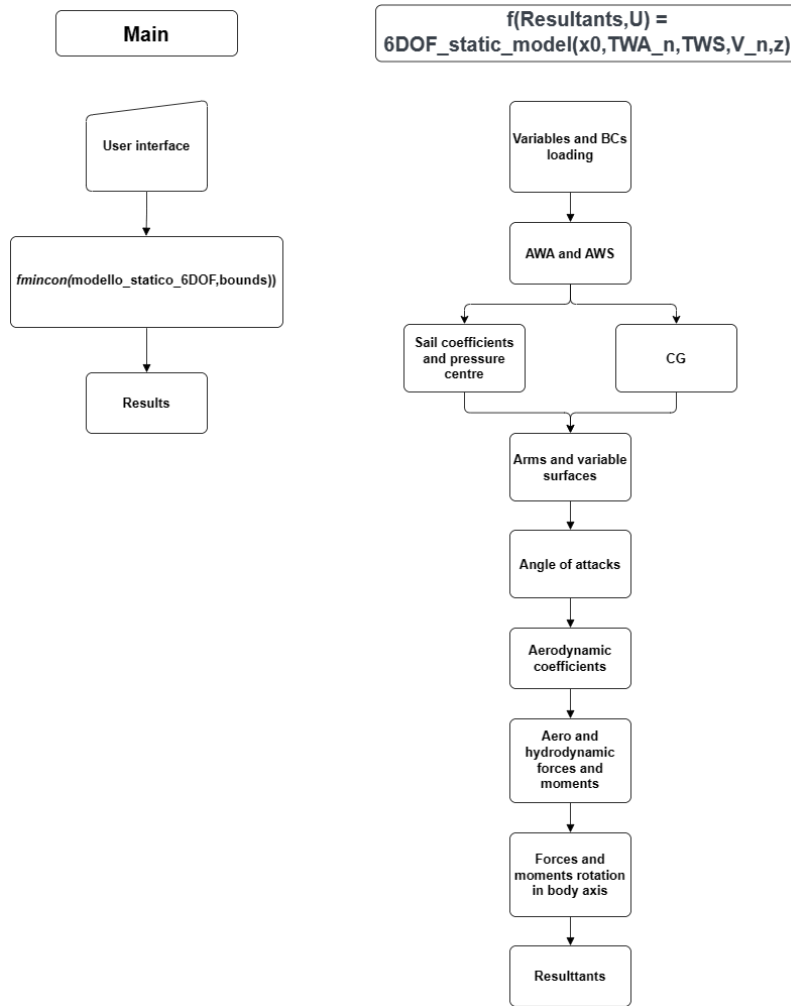


Figure 53: 6DOF static model structure.

Those boxes of the previous figure which introduce new elements will be taken into account in the following paragraphs.

6.2 Sail model

Another novelty of this model respect to the previous lies in the sail modelisation. Instead of determining the sail trust which ensures the equilibrium, this time the lift of the sail is calculated the same way as the other aerodynamic ones. The sail has been treated as a wing in the airflow, so the force is transversal to the apparent wind direction and its modulus depends quadratically on the apparent wind speed and the sail incidence with a

trend reported in the already mentioned bibliography [4].

6.2.1 Sail power control

First of all, it is necessary to determine the sail incidence AWA_{sail} , which is decided by the athlete through the boom. As it will be shown in the following paragraph 6.2.2 the sail lift coefficient varies in a range of $[0, 1.4]$ with $0 < AWA_{sail} < 32^\circ$ and over 32° decrease, so it is assumed that:

- the maximum realistic AWA_{sail} is the apparent wind angle felt by the board;
- if AWA is greater than 32° , the maximum realistic AWA_{sail} is 32° ;
- the choice of AWA_{sail} is made by the sailor which is emulated by *fmincon* algorithm in order to maximise U without exceeding the bounds.

These assumption are implemented through the parameter $sail_p$ which stands for *sail power*: it varies between 0 ($AWA_{sail} = 0$) and 1 ($AWA_{sail} = AWA \vee 32^\circ$):

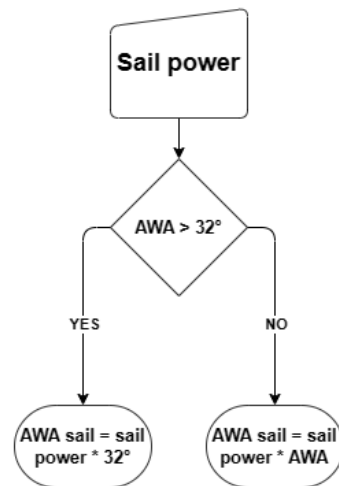


Figure 54: Sail power logic.

6.2.2 Sail force coefficient

The lift coefficient of the sail represents one of the most difficult parameters to be determined. Since the problem has been circumvented in the 3DOF model providing an affordable tool for the consultancy to the FIV, in this step a greater error on some parameters is acceptable, as long as the trends were correct.

However, the job of Keith Alexander can be taken into account, providing a useful source to

draw from. In his paper, he tested experimentally some sail models which emulated various rig conditions. As a result, he obtained the relative CL-AWA curves. The same interpolation points have been used to create a *dat* file with the sail aerodynamic derivatives.

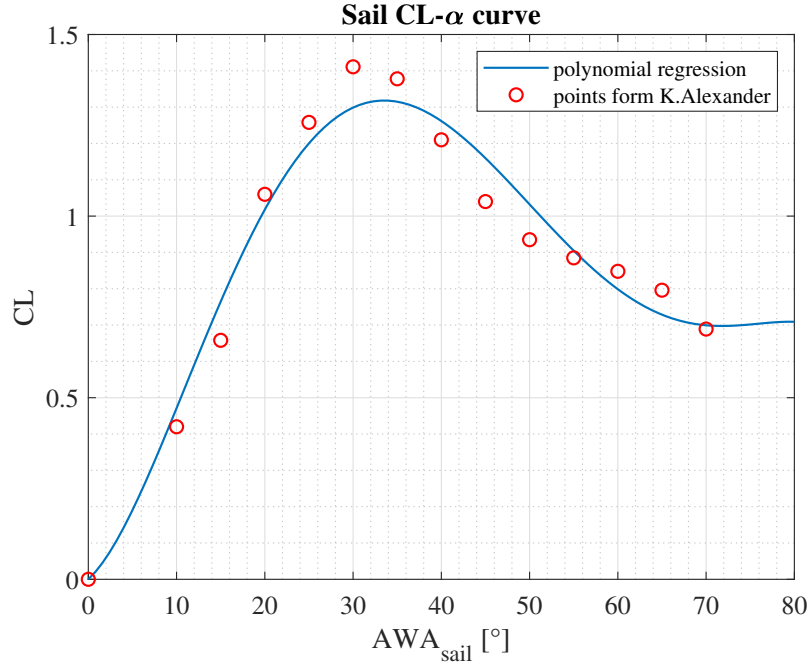


Figure 55: Sail CL- α curve [4].

So that the sail depowering model can work, the sail CL for $AWA_{sail} = 0$ must be 0 too. This assumption agrees with the real state of things, given that a sail disposed parallel to the wind direction produces no lift. Therefore, *polyfit* function has not been used this time, but a polynomial interpolation through the least square algorithm implemented in *linsolve* has been performed. In this way, the regression terms were a user choice and the vertical intercetta could be imposed equal to zero upstream from the minimisation problem.

6.3 Attack angles determination

In order to take into account the angular velocity aerodynamic derivatives, the relationship between them and the relative attack angle has been modeled. The trigonometric epitome of functions used for this goal is:

$$\alpha_i = \alpha + atg\left(\frac{(x_{cg} - x_i)\omega}{u}\right) \quad (14)$$

Where α_i is the incidence felt by the i^{th} component, α is the iQfoil incidence, $x_{cg} - x_i$

is the arm of the component respect to the centre of gravity, along the same direction of u and transversal to ω rotation axis. In this step, the angular velocity is still set to 0 because of the stationary of the problem, but the same functions have been used in the dynamic model provided in the following paragraphs for a communication issue. For this reason, the attack angles are already computed as the Euler angles rate could be non-null.

6.4 Foil's lateral-directional coefficients

As explained in paragraph 4, The CFD analysis on the foil exploited the geometrical symmetry to reduce the computational effort of the study. However, the symmetry on boundaries conditions had to be imposed to, deleting the chance of determining the lateral-directional aerodynamic coefficients. In order to workaround, the empirical equations for their estimation have been implemented in a dedicated *Matlab* function. Some contributions are null in this stage, because the rotational velocities are set to zero. However, the static model will be embedded in the following dynamic models, reason why they were determined since the static model and the angular speeds set to zero.

	Y-forces der.	Yaw. moment der.	Roll. moment der.
β	$C_{y\beta} = alr.$	$C_{n\beta} = C_{n\beta wb} + alr.$	$C_{l\beta} = \left(\frac{C_{l\beta}}{\Gamma}\right) \Gamma + \Delta C_{l\beta}$
p	$C_{yp} = C_L \frac{AR + \cos\Lambda}{AR + 4\cos\Lambda} tg\Lambda$	$C_{np} = -\frac{C_L}{8}$	$C_{lp} = -\frac{C_{L\alpha}}{12} \frac{1+3\lambda}{1+\lambda}$
r	$C_{yr} = alr.$	$C_{nr} = alr.$	$C_{lr} = \frac{C_L}{4} + alr.$

Table 9: Aerodynamics lateral-directional coefficients derivatives [17].

Where *alr.* stands for *already considered* as it happened for those derivatives which treated the aerodynamics of the vertical which has been studied with *Star ccm+* and *Xflr5*. The numerical values found with the equation above are:

	Y-forces der.	Yaw. moment der.	Roll. moment der.
β	$C_{y\beta} = alr.$	$C_{n\beta} \approx 0 + alr.$	$C_{l\beta} \approx 0$
p	$C_{yp} = 0.014$	$C_{np} = -0.21$	$C_{lp} = -0.01$
r	$C_{yr} = alr.$	$C_{nr} = alr.$	$C_{lr} = 0.03 + alr.$

Table 10: Aerodynamics lateral-directional coefficients derivatives (numerical values).

6.5 Equilibrium equations

At this point, each force component can be determined, and so the relative vectors. The resulting forces and moments vector has been written as the sum of all the forces concatenated with the sum of all the moments, both previously rotated in the body reference system. The complete rotation matrix is the product of the same around each axis[18]:

$$\bar{F}_{body} = \begin{Bmatrix} F_{xb} \\ F_{yb} \\ F_{zb} \end{Bmatrix} = \bar{\Psi} \bar{\Theta} \bar{\Phi} \bar{F}_{flow} \quad (15)$$

Where Ψ , Θ and Φ are the rotation matrix around the z, y and x axis with the structure presented in eq. 8:

$$\bar{\Psi} = \begin{bmatrix} \cos\psi & -\sin\psi & 0 \\ \sin\psi & \cos\psi & 0 \\ 0 & 0 & 1 \end{bmatrix}; \bar{\Theta} = \begin{bmatrix} \cos\theta & 0 & \sin\theta \\ 0 & 1 & 0 \\ -\sin\theta & 0 & \cos\theta \end{bmatrix}; \bar{\Phi} = \begin{bmatrix} 1 & 0 & 0 \\ 0 & \cos\phi & -\sin\phi \\ 0 & \sin\phi & \cos\phi \end{bmatrix} \quad (16)$$

Moreover, the following property of the rotation matrix will be used in the exposed models [18]:

$$\begin{aligned} \bar{\Psi} \bar{\Theta} \bar{\Phi} &= \bar{R}_b^a(\Theta_{ab}); \\ \bar{R}_a^b(\bar{\Theta}_{ab}) &= \bar{R}_b^a(\bar{\Theta}_{ab})^{-1} = \bar{R}_b^a(\bar{\Theta}_{ab})^T \end{aligned} \quad (17)$$

In eq: 17, $\bar{\Theta}_{ab} = \{\phi\theta\psi\}^T$ and \bar{R}_b^a stands for the matrix which rotate a vector from the reference system b to the a .

In the following table, the initial force vector and the rotation angles are reported:

	flow v.	x	y	z
Mainfoil	$\{-D, Y, -L\}^T$	ϕ	α	β
Tail	$\{-D, 0, -L\}^T$	ϕ	α	β
Strut	$\{-D, L, 0\}^T$	ϕ	0	β
Board	$\{-D, 0, -L\}^T$	ϕ	α	AWA
Athlete	$\{-D, 0, 0\}^T$	0	0	AWA
Sail	$\{0, L, 0\}^T$	ϕ	0	AWA

Table 11: Components' force vector in the flow reference system and the angles to rotate them in body axis.

For what it concerns the moments, focal yaw and roll moments have been obtained as the forces. Pitch focal moments of mainfoil, tail and board have been determined as the intercetta of the line which describes the total pitch moment in function of the lift arm.

$$M_i = M_{0i} + L_i(x_i - x_{cg}) \quad (18)$$

Where M_i is the pitch moment obtained in paragraph 4 centred the CFD origin, M_{0i} is the focal component and $L_i(x_i - x_{cg})$ is the moment due to the lift arm.

Then a moment vector has been written for each component, summing the component due to forces arms to the eventual focal one.

The external forces and moments vector assume the same form as in paragraph 5 but expanded:

$$\tau = \begin{Bmatrix} F_x \\ F_y \\ F_z \\ M_x \\ M_y \\ M_z \end{Bmatrix} \quad (19)$$

6.6 Solution method

In section 6.1, the under-determination of the equilibrium problem and the existence of infinite solutions were mentioned. In this paragraph, the solution method will be explained. First of all, it is necessary to recall the dependent variables adding the relative boundaries:

$$x_0 = \begin{cases} x_{athlete} & \text{bounds: } [0; 1] & [m] \\ y_{athlete} & \text{bounds: } [0.4; 2] & [m] \\ x_{sail} & \text{bounds: } [-1; 1] & [m] \\ sail_p & \text{bounds: } [0, 1] & [] \\ U & \text{bounds: } [0, 40] & [kn] \\ \phi & \text{bounds: } [0, 0.5] & [^\circ] \\ \theta & \text{bounds: } [-5, 5] & [^\circ] \\ \psi & \text{bounds: } [-0.5, 0.5] & [^\circ] \\ \beta & \text{bounds: } [-5, 2] & [^\circ] \end{cases} \quad (20)$$

Since now, the choice criteria of the most interesting solution will be such as to maximise U , but the following arguments are valid for every other condition which occurs in this thesis.

The existence of more solutions can be demonstrated by running *fmincon* function from several random points. The function to be minimised is the τ vector, which is null in the equilibrium condition. In appendix A table 20 can be noticed that, starting from twenty

random points, it is possible to find several different solutions. Then the objective function has been changed as follows:

$$f_{obj}(x) = \tau + w \frac{1}{U} \quad (21)$$

Where w is a weight chosen to ensure the convergence in all those situations the iQfoil can fly. As an indication of the effectiveness of this method, the model has been solved starting from another twenty points, and the same solution has been obtained each time. The results of this try are reported in appendix A table 21. At this point, there are two issues to face: the determination of a weight w that fits with the problem and a more formal verification that the weighted objective function method has only one minimum and that it is actually the equilibrium point with the greater value of U .

The weight w determination will be quickly faced. *Fmincon* is a gradient method function which minimises a provided non-linear function. Likewise all the gradient-method based functions, it is fast, but it risks incurring local minimums if they exist. For $w \rightarrow 0$, indeed, any equilibrium condition can be found depending on the starting point. On the other side, if the maximisation of U is too awarded, the new solutions for the limit flying conditions will present a τ vector too far from zero. The better compromise has been found for $w = 1000$, which is a value largely sufficient to ensure the results shown in table 21, but small enough so that the solver converges for each angle in the TWA range specified by FIV as plausible. For what it concerns the validation of the method, a much more time-consuming analysis has been carried out, but based on *genetic algorithm*, which can find the global minimum without incurring in local ones. Moreover, the objective function has been re-defined as dependent on the speed only and a nonlinear constraint has been imposed:

$$\begin{aligned} f_{obj}(x) &= 1/U \\ f_{nonlinear\ constraint}(x) &= \tau - 0.01 < 0 \end{aligned} \quad (22)$$

from eq. 22 appears that the residual can be much greater than they resulted in the solution found through the gradient-method, then the same solutions or better are expected this time. Between the options, *population size = 200, max. generations number = 100* have been set, as the *Matlab guide* advises [19], and the solution found by *fmincon* has been provided as initial population:

	GA algortihm	Gradient method (<i>fmincon</i>)
x_{ath}	0.91476	0.91476
y_{ath}	1.4955	1.4955
x_{sail}	0.21755	0.21755
$sail_p$	0.19992	0.19992
U	29.521	29.521
ϕ	0.42486	0.42486
θ	0.72276	0.72276
ψ	-0.88829	-0.88829
β	-1.3689	-1.3689
res_{max}	0.00052035	0.00052035

Table 12: Comparison between the results obtained through GA and gradient based algorithm.

In the previous table, we can see the two algorithms found the same solution, this indicates that minimising a weighted objective function through the gradient-method is a valid procedure to solve the equilibrium system.

6.7 Results

The static model has been used to obtain some data to compare with what FIV coaches told us in the previous stage of this work. In particular, three more conditions have been computed: higher flight, heavier athlete and different tail rake. According to what they told us, in all these cases the speeds should be higher than in table 12, and so it is:

	$z = 0.7m$ $W_{ath} = 70kg$ $rake_{tail} = 0.5$	$z = 0.8m$ $W_{ath} = 70kg$ $rake_{tail} = 0.5$	$z = 0.7m$ $W_{ath} = 90kg$ $rake_{tail} = 0.5$	$0.7m$ $W_{ath} = 70kg$ $rake_{tail} = -1$
x_{ath}	0.91476	0.99166	0.83754	0.71817
y_{ath}	1.4955	1.4955	1.4946	1.4962
x_{sail}	0.21755	0.22162	0.22989	0.23009
$sail_p$	0.19992	0.20038	0.22834	0.19874
U	29.521	30.0654	31.6968	30.4748
ϕ	0.42486	0.45181	0.4081	0.44883
θ	0.72276	0.67077	0.77385	0.38057
ψ	-0.88829	-0.9047	-0.89559	-0.92057
β	-1.3689	-2.1139	-1.4894	-1.2862
res_{max}	0.00052035	0.00075706	0.0022536	0.00068929

Table 13: Comparison between four cases study.

Indeed, a higher flight causes less drag and then it is necessary a higher speed to balance the sail trust. The heavier athlete, however, can balance a greater pitching-up moment, keeping the foil flat in more extreme conditions. The last case study regards the tail rake, which reduces the pitching-up moment of the foil, as reported in par. 5, with the same consequences explained above.

At last, two polar graphs obtained by FIV data and through the model have been compared. About the software with which the empirical graph has been plotted, it is necessary to know that it works on only one training day. It is, therefore, not generated from a statistically relevant number of data. Moreover, the true wind direction is automatically set depending on the shape of the polar rather than on a direct measure. On the other hand, the plot realised on *Matlab* is affected by the assumption on the sail and shows the maximum speeds which can be reached. If the two graphs were equal it would mean that FIV athletes already sail as fast as possible. The most important aspect is the shape of the polar, which validates the sail aerodynamic derivatives and the whole static model too.

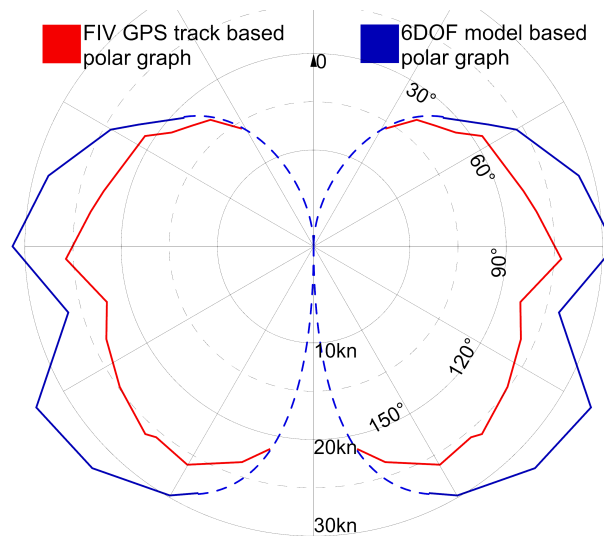


Figure 56: Comparison between empirical and numeric iQfoil polar graph.

7 6DOF dynamic model: Plant

The dynamic analysis of the iQfoil is a powerful tool that allows the study of its stability and modal coupling. In this paragraph, the plant model implementation and linearisation will be faced. The linearised system is a fundamental output of this stage, because, besides the aforementioned considerations, it allows the development of a *stability augmentation system* which emulates the ability of the athlete to nullify the effect of unstable modes, as treated in the section ??.

7.1 Structure

For the dynamic model implementation, *Simulink* has been exploited, a *Matlab* plug-in. It is a block diagram environment useful to design and simulate system[20]. As already explained in the previous paragraph, the 6DOF static model is embedded in the dynamic one. During a time step, in fact, the external forces vector τ and other parameters as CG , R_b^n and V_b , have to be determined in the same way by both the tools. Then, instead of nullifying τ in order to search an equilibrium point, it becomes part of a linear system where the independent variable is the acceleration vector. Once it is found, through integrations and rotations it is possible to determine the next time step's initial condition.

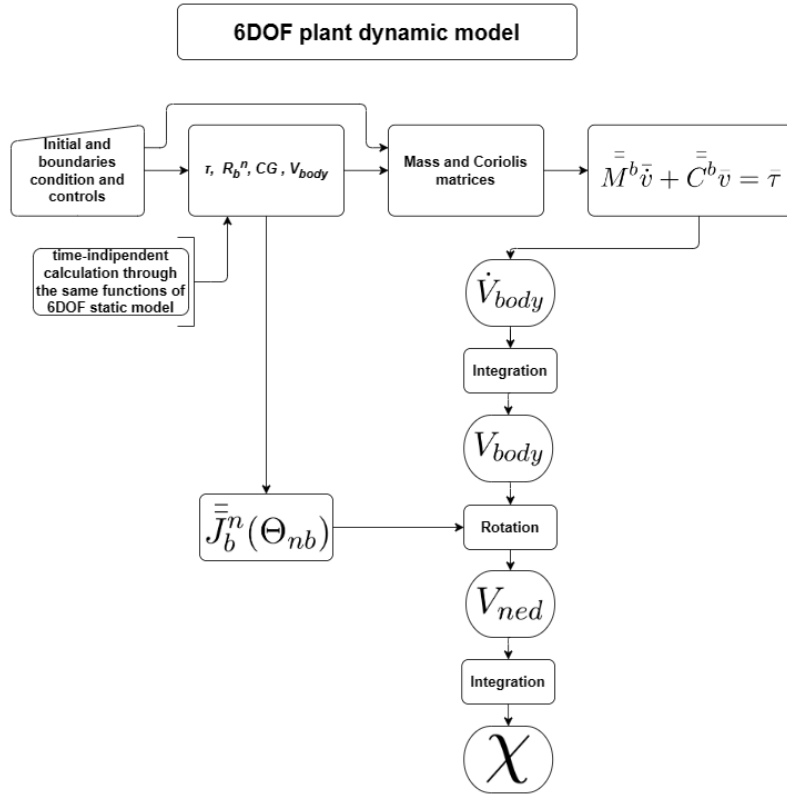


Figure 57: 6DOF plant dynamic model structure.

Particular attention will be paid to the linear system $M\dot{v} + Cv = \tau$ and to the computation of M and C matrices. In addition, the inertia update in function of the sailor position and mass deserves a particular focus. Then, the rotation matrices' composition and their usage will be treated.

7.2 Dynamic system solution

Once determined the external actions vector, the dynamic system can be written to find the acceleration vector. Considering no assumption the expanded form system appears as it follow[18]:

$$\begin{cases}
m \left[\dot{u} - vr + wq - x_g^b (q^2 + r^2) + y_g^b (pq - \dot{r}) + z_g^b (pr - \dot{q}) \right] & = \tau_1^b \\
m \left[\dot{v} - wp + ur - y_g^b (p^2 + r^2) + z_g^b (rq - \dot{p}) + x_g^b (pq - \dot{r}) \right] & = \tau_2^b \\
m \left[\dot{w} - uq + vp - z_g^b (q^2 + p^2) + x_g^b (pr - \dot{q}) + y_g^b (qr - \dot{p}) \right] & = \tau_3^b \\
I_x^b \dot{p} + \left(I_z^b - I_y^b \right) qr - (\dot{r} + pq) I_{xz}^b + (r^2 - q^2) I_{zy}^b + (pr - \dot{q}) I_{xy}^b + \\
\quad + m \left[y_g^b (\dot{w} - uq + vp) - z_g^b (\dot{v} - wp + ur) \right] & = \tau_4^b \\
I_y^b \dot{q} + \left(I_x^b - I_z^b \right) rp - (\dot{p} + qr) I_{xy}^b + (p^2 - r^2) I_{xz}^b + (qp - \dot{r}) I_{yz}^b + \\
\quad + m \left[z_g^b (\dot{u} - vr + wq) - x_g^b (\dot{w} - uq + vp) \right] & = \tau_5^b \\
I_z^b \dot{r} + \left(I_y^b - I_x^b \right) pq - (\dot{q} + rq) I_{yz}^b + (q^2 - p^2) I_{xy}^b + (rq - \dot{p}) I_{zx}^b + \\
\quad + m \left[x_g^b (\dot{v} - wp + ur) - y_g^b (\dot{u} - vr + wq) \right] & = \tau_6^b
\end{cases} \quad (23)$$

To simplify the debug process, the previous equations have been written in matrix form instead of the expanded one[18].

$$\bar{M}^b \bar{\dot{v}} + \bar{C}^b \bar{v} = \bar{\tau} \quad (24)$$

With:

$$\begin{aligned}
\bar{M}^b &= \begin{bmatrix} m \bar{I}_{3 \times 3} & -m \bar{S}(\bar{r}_g) \\ m \bar{S}(\bar{r}_g) & \bar{I}^b \end{bmatrix}; \\
\bar{C}^b &= \begin{bmatrix} m \bar{S}(\bar{v}) & -m \bar{S}(\bar{v}) \bar{S}(\bar{r}_g) \\ m \bar{S}(\bar{v}) \bar{S}(\bar{r}_g) & -\bar{S}(\bar{I}^b \bar{v}) \end{bmatrix}; \\
\bar{S}(\lambda) &= \begin{bmatrix} 0 & -\lambda(3) & \lambda(2) \\ \lambda(3) & 0 & -\lambda(1) \\ -\lambda(2) & \lambda(3) & 0 \end{bmatrix}; \quad (25)
\end{aligned}$$

$$\bar{I}^b = \begin{bmatrix} I_{xx} & I_{xy} & I_{xz} \\ I_{xy} & I_{yy} & I_{yz} \\ I_{xz} & I_{yz} & I_{zz} \end{bmatrix}$$

$$\bar{v} = \begin{Bmatrix} p \\ q \\ r \end{Bmatrix}$$

Where $I_{3 \times 3}$ is the 3×3 identity matrix, m the mass of the system and r_g the centre of gravity vector. If a new reference system is defined, with the axis aligned with the body's ones and the origin centered in the CG, then r_g becomes a null vector and $S(r_g)$ an empty matrix. Hence the mass and Coriolis matrices become symmetrical:

$$\begin{aligned}\bar{M}_{CG}^b &= \begin{bmatrix} m\bar{I}_{3\times 3} & 0 \\ 0 & \bar{I}^b \end{bmatrix}; \\ \bar{C}_{CG}^b &= \begin{bmatrix} m\bar{S}(\bar{\nu}) & 0 \\ 0 & -\bar{S}(\bar{I}^b\bar{\nu}) \end{bmatrix};\end{aligned}\tag{26}$$

It is, actually, of easy comprehension that, if the reference system is centered in the CG, an inequality in forces equations will not cause an angular acceleration and vice-versa.

7.3 Inertia matrix

Once the reference system is centered in the CG, the effect of controllers as the athlete's position lies in the origin displacement and the consequent variation of all force's arms. This concept was already behind the equilibrium point search through the static model. However, now it implies the need for additional consideration. Indeed, as the centre of gravity is computed at each time step, the same must happen for each term represented in eq.26. Although for ν it happens spontaneously, the same argument cannot be applied to I^b , reason why a specific function has been implemented. In the next paragraphs will be explained at first how the inertia update function works, and then how the interpolation coefficients behind it have been found.

7.3.1 Inertia update function

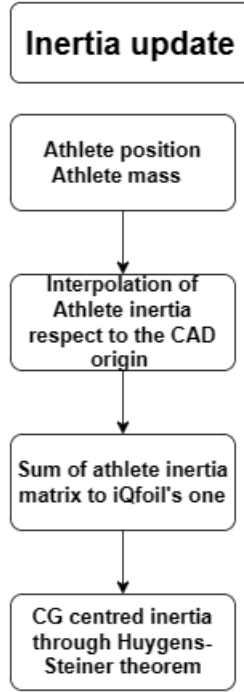


Figure 58: Inertia update function structure.

As it emerges in fig. 59, this function's structure is simple. Only two aspects deserve attention: the coincidence of iQfoil and athlete inertias origins before their sum and that of the CGs computed by *Simulink* and by *Rhino*. The last hypothesis is fundamental for the Huygens-Steiner theorem application.

$$\bar{\bar{I}}_{CG} = \bar{\bar{I}}_O - m [(\bar{r} \cdot \bar{r}) I_{3x3} - \bar{r} \times \bar{r}] \quad (27)$$

In eq. 27 it can be noted that the inertia computed in the CG must be alternatively the base or the destination of the process. However, the inertias used to find the coefficients pertain to a system and so it is after the interpolation. Therefore the r in the previous equation must refer to its centre of gravity, even if it is calculated starting from the one calculated at each time step by *Simulink*, reason why they have to be exactly the same point.

7.3.2 Interpolating inertia matrices

It has been mentioned that the athlete inertia matrix is calculated through an interpolation which depends on the athlete's position and its weight. The relative coefficients have been found thanks to *polyfitn*, likewise the board's aerodynamic derivatives. The interpolating data, instead, are the results of a process implemented in *Python*[9] and run on the *Rhino* internal compiler.

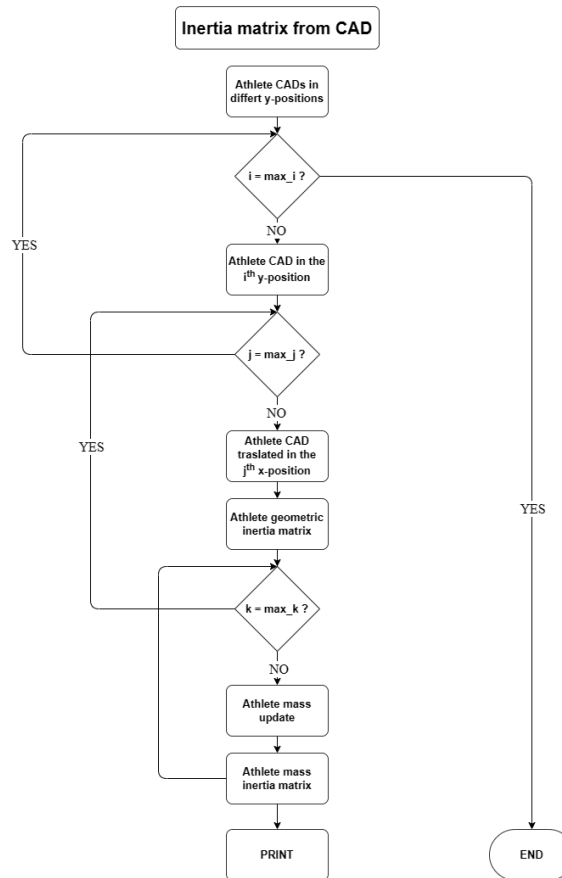


Figure 59: Inertia interpolating matrices generator structure.

The Python script is composed of 3 nested for-cycles. The indices that control them correspond to four y-positions, four x x-positions and 3 weights. This means that, at the end of the run, 48 inertia matrices have been printed, while the interpolating coefficients are 10. The program takes in input the Athlete CADs already disposed in all the y-positions. Depending on the first index, it moves one of them along the x direction and assigns to him a weight according to the for-cycles logic. At each iteration, the inertia matrix is printed.

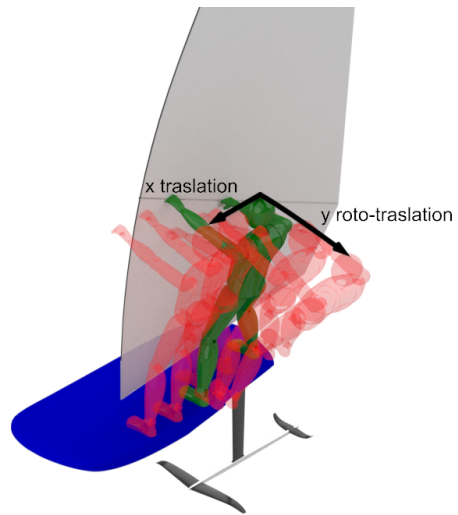


Figure 60: Athlete movement representation.

As an example of the results, various inertia moments have been represented for a 100kg athlete as a function of x_{ath} and y_{ath} .

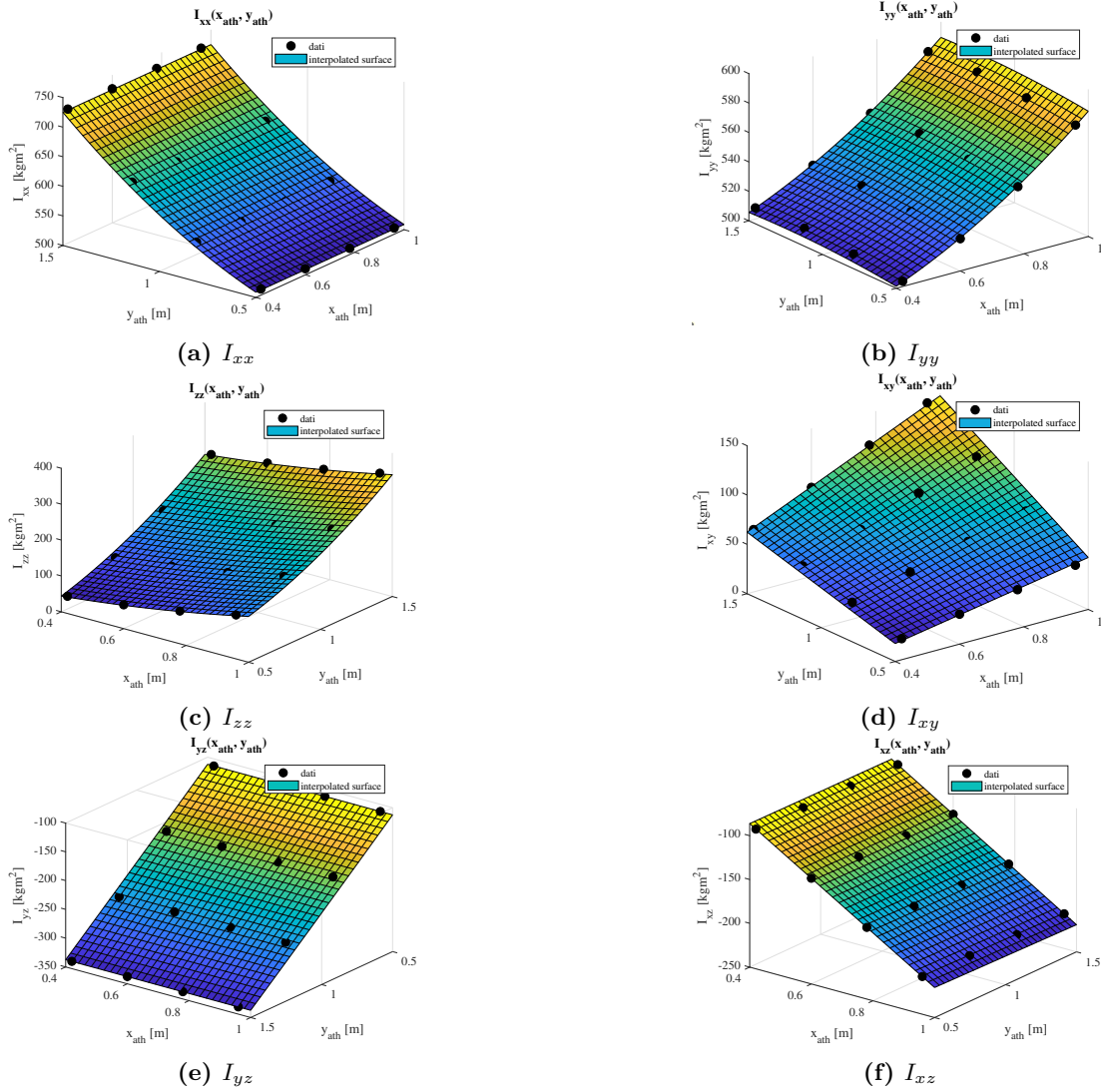


Figure 61: Comparison between the CAD computed inertias and the resulting interpolation as a function of a 100Kg athlete position.

7.4 Model linearisation

Once completed the plant dynamic model an issue arises: the system is not stable and each random disturbance or initial condition supposedly affects the unstable modes too. Since the equilibrium condition found in chapter 6 ensures the τ vector magnitude to be smaller than tolerance, it is impossible to provide as an initial condition a fully clean equilibrium point. Moreover, the divergence due to unstable modes is exponential with time, so, even

if the initial error is apparently negligible, the system will relentlessly diverge. The same argument if an initial condition with the same shape of a stable mode is provided.

This issue imposes the implementation of a linearised model. The final output required in this step is a space-state model, meaning a description of the system in the following form:

$$\begin{aligned}\dot{\bar{x}} &= \bar{A}\bar{x} + \bar{B}\bar{u}; \\ \bar{y} &= \bar{C}\bar{x} + \bar{D}\bar{u};\end{aligned}\tag{28}$$

$$x = \begin{Bmatrix} z \\ \phi \\ \theta \\ \psi \\ U \\ \alpha \\ \beta \\ p \\ q \\ r \end{Bmatrix}; \quad u = \begin{Bmatrix} x_{ath} \\ y_{ath} \\ x_{sail} \\ p_{sail} \end{Bmatrix}\tag{29}$$

Given that y is an arbitrary combination of x and u , the same applies to C and D . To A and B , however, the following relationships are applied:

$$\dot{\bar{x}}_i = \bar{A}_{ij}\bar{x}_j + \bar{B}_{ij}\bar{u}_j\tag{30}$$

Which means:

$$\begin{aligned}\bar{A}_{ij} &= \frac{\partial \dot{\bar{x}}_i}{\partial \bar{x}_j} \\ \bar{B}_{ij} &= \frac{\partial \dot{\bar{x}}_i}{\partial \bar{u}_j}\end{aligned}\tag{31}$$

Since the non-linear plant model cannot diverge in zero seconds, the variation of a $\dot{\bar{x}}$ element as a result of a perturbation of a \bar{x} element can be easily determined. This argument is the basis of the numeric linearisation script in *Matlab* language reported in Stevens, Lewis and Johnson's job [21]:

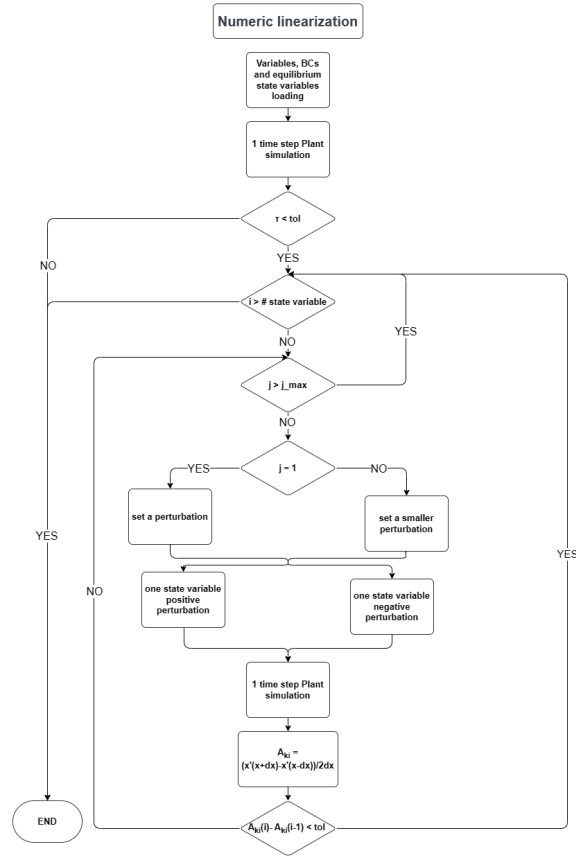


Figure 62: A and B matrices linearisation script structure.

Using this type of algorithm, it is important to not forget that the linearisation hypothesis must still be respected. In this case, the assumptions imposed on the static model to have a linearizable condition were those of *steady level flight*:

$$\begin{aligned}
 \dot{\phi} &\equiv 0; \\
 \dot{\phi} &\equiv 0; \\
 \dot{\theta} &\equiv 0; \\
 \dot{\psi} &\equiv 0;
 \end{aligned} \tag{32}$$

The same process has been repeated to determine both A and B , which are reported in appendix B eq. 51. The first output that can be produced starting from A matrix lies in its eigenvalues and vector. Below the plant root locus is shown.

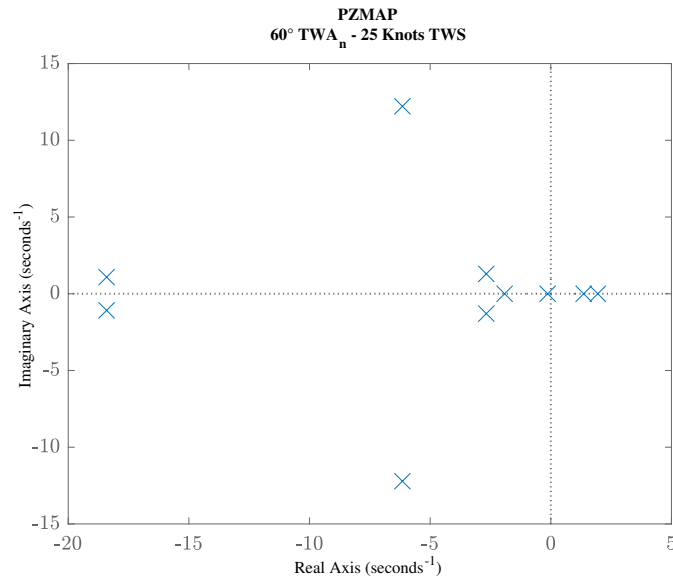


Figure 63: Root locus of the system linearised for $U = 31.5kn$, $TWS = 25kn$, $TWA = 60^\circ$.

In this condition, there are only three oscillating modes, whose *Argand diagrams* are reported below.

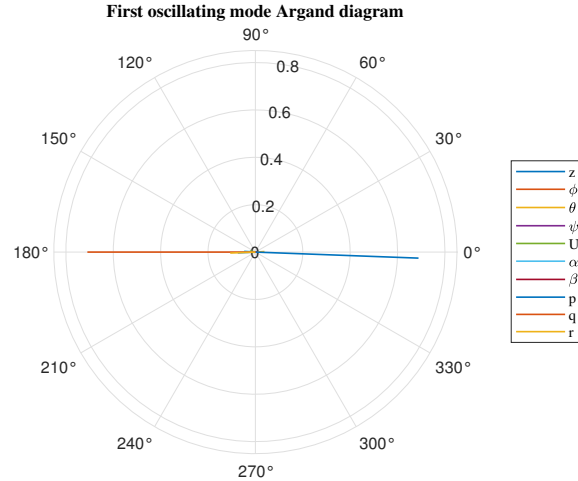


Figure 64: Argand diagram for the first oscillatory mode .

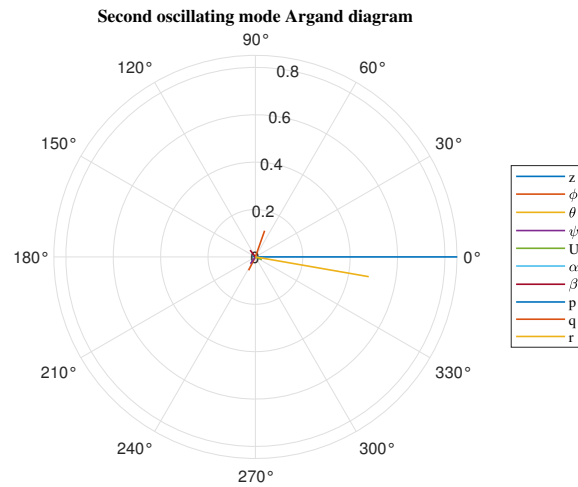


Figure 65: Argand diagram for the second oscillatory mode.

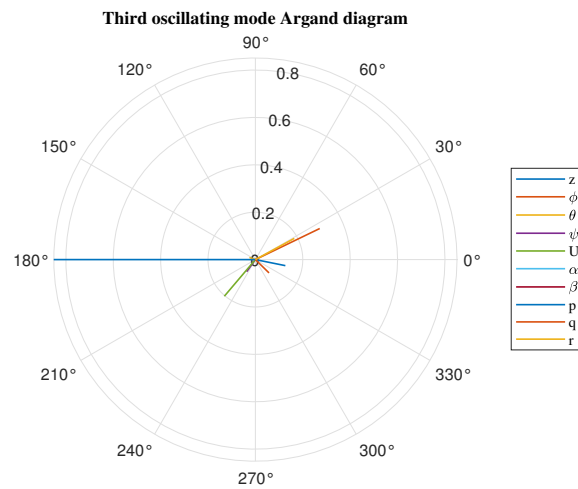


Figure 66: Argand diagram for the third oscillatory mode .

Now a more complete explanation can be given about the modal coupling. When an aircraft is modeled, in several conditions it is possible to uncouple the motion, meaning to build longitudinal and lateral-directional models whose modes are exactly the same of the original ones. This can happen if the linearisation happen under this hypothesis [22]:

- Mass and geometry symmetry respect with the XZ plane;
- The linearisation of the equation (small attack angles and small perturbation);

Since the mass is strongly asymmetrical, it is possible to affirm that the system is coupled. Moreover, a simple test has been conducted: the root locus of the uncoupled system has been superimposed on that of the complete one. The longitudinal and the lateral-directional models have been obtained by neglecting the coupling terms of the A matrix:

$$\bar{A} = \begin{bmatrix} \bar{A}_{long.} & Negl. \\ Negl. & \bar{A}_{lat-dir} \end{bmatrix}; \quad \text{with } x \text{ rearranged as: } x = \begin{pmatrix} z \\ \theta \\ U \\ \alpha \\ q \\ \phi \\ \psi \\ \beta \\ p \\ r \end{pmatrix} \quad (33)$$

Where *Negl.* stands for *neglected terms*. The result is shown by the following root locus:

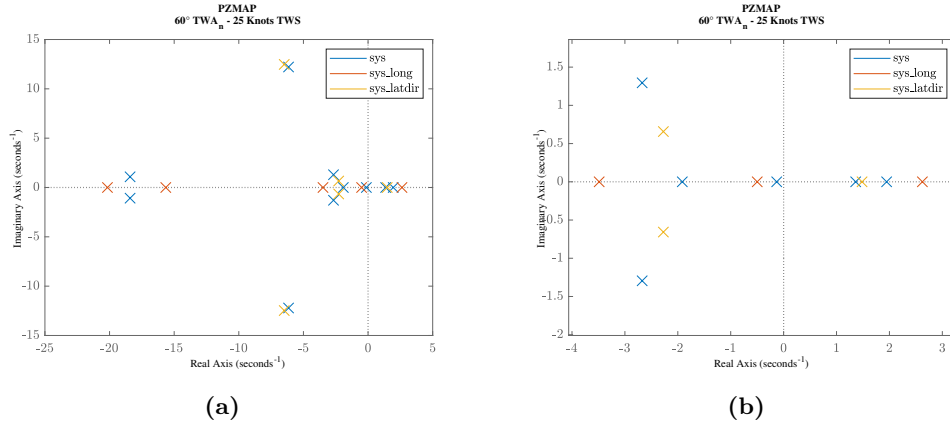


Figure 67: Root locus of the complete and of the decoupled systems superimposed (a) and a close-up on the poles nearer to the origin (b).

How much they have to differ in order to choose if the system can be uncoupleable is a complex argument that deserves a deeper study. In this work, however, the analysis is limited to notice that the difference between the poles in terms of ω and ζ is too great to be neglected. Moreover, the number of conjugate-complex eigenvalues of the complete system is different than the sum of those of decoupled ones. These arguments are enough to define the system as non-uncoupleable.

A physical example of what it means can be made by multiplying A with a null vector

except for one term, which can be α .

$$A\Delta x = \begin{pmatrix} -0.12 \\ \mathbf{0} \\ 0 \\ \mathbf{0} \\ -0.21 \\ -0.23 \\ -\mathbf{0.00015} \\ \mathbf{2.4} \\ -1.3 \\ \mathbf{0.47} \end{pmatrix}; \quad \bar{A}_{uncoup.}\Delta x = \begin{pmatrix} -0.12 \\ \mathbf{0} \\ 0 \\ \mathbf{0} \\ -0.21 \\ -0.23 \\ \mathbf{0} \\ \mathbf{0} \\ -1.3 \\ \mathbf{0} \end{pmatrix}; \quad \Delta x = \begin{pmatrix} 0 \\ 0 \\ 0 \\ 0 \\ 0 \\ \frac{\alpha}{2} \\ 0 \\ 0 \\ 0 \\ 0 \end{pmatrix}; \quad (34)$$

From eq 34 it appears that, if a disturb is applied on a longitudinal dynamic quantity, the lateral-directional angle rates are affected too, and not in a negligible way. This happens because if the incidence increases, the foil produces both more drag and lift. Since the centre of gravity does not lie on the XZ plane, the forces on the foil act distant from it along the y-direction causing non-negligible yaw and roll moments to arise.

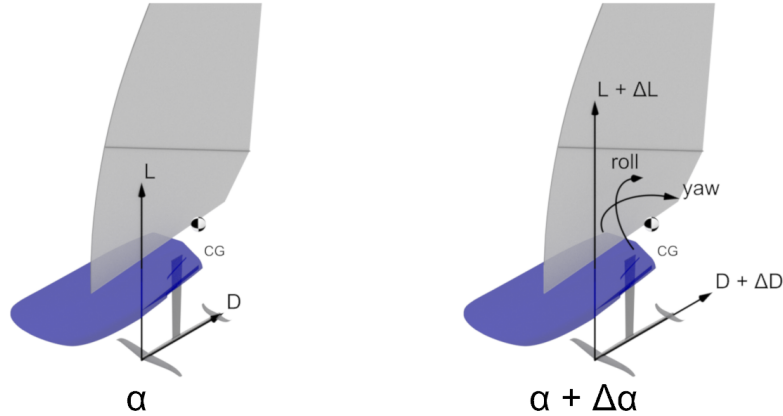


Figure 68: Physical representation of the yaw and roll moments caused by a $\Delta\alpha$.

7.4.1 Linearisation validation

At last, the linearised model has to be verified. the simplest method consists of applying an initial condition next to the equilibrium point and superimposing the responses of non-linear and linearised models. However, the issue of the fast divergence induced by the numerical error keeps standing. So a way to work around the problem has been developed: applying

as an initial condition a faster stable mode the response of the non-linear system will be the sum of the chosen modal response and the aforementioned divergence. The modal response has to be separated to compare it with that of the linearised system, and this is possible thanks to a wise choice of the mode and measuring if the frequency oscillation matches to that determined from the pole imaginary part.

$$\begin{aligned}\lambda &= -6.15 - 12.2i; \\ \omega &= 12.2 \frac{rad}{s}; \\ \zeta &= 0.45; \\ T &= \frac{2\pi}{\omega} = 0.515s;\end{aligned}\tag{35}$$

A brief anticipation of the results exposed in appendix C is reported below in order to show the matching of periods determined from the pole and measured on the response graph:

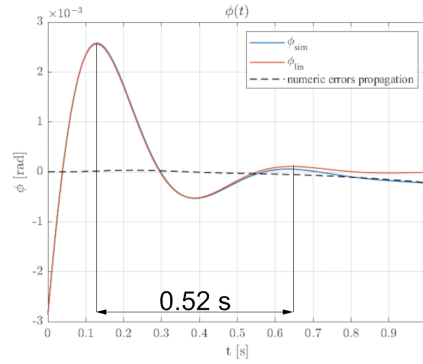


Figure 69: Measurement of the period of the second mode of the system

8 Control system

In the last part of this thesis, a control system able to emulate the athlete function of stabilising and piloting the iQfoil has been implemented. The human brain cannot be optimised and, even if it were, it would be much above the ambitions of this job. For this reason, the design of the *SAS* and the autopilot does not follow exactly the brain logic, but it has, instead, the purpose of allowing the iQfoil's flight simulation.

In the next paragraphs, the general structure will be explained and then the design process. At last, some realistic disturbances have been modeled, which, together with some plausible step commands, constitute various case studies. The results will be exposed subsequently.

8.1 Structure

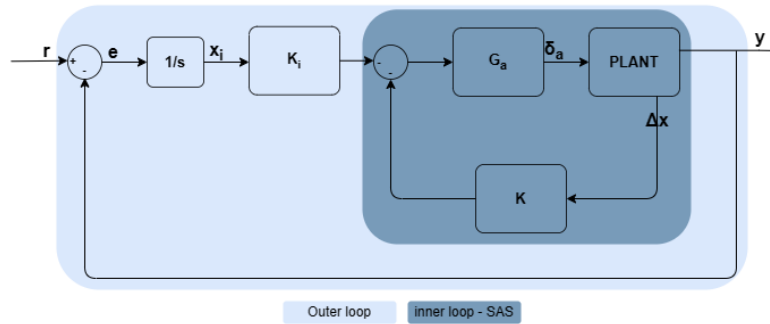


Figure 70: Control system block diagram.

Where r is the desired state vector, composed by the 4 quantities from x the athlete can and wants control: $\{z \ \phi \ \psi \ \beta\}^T$. This vector has been defined considering that some states, like θ , are controlled to ensure the equilibrium and stability of the system, so they are processed by the *SAS* only, and others do not have a specifically desirable value, as U , which is to maximise by optimising r . Finally, the angle rates are not included in r because they must be zero in the steady state.

In figure 70, K and K_i are systems' gains, *Plant* is the block that represents the non-linear system implemented previously and G_a is the actuator transfer function. Likewise the human brain's ability to elaborate inputs and outputs is not the aim of this job, the same is true for the modelisation of the neural and muscular systems transfer functions, which has been written with the only purpose of preventing any excessively fast actuator responses. A good compromise is represented by a low-pass filter with a cut-off frequency plausible and coherent with the performances expected from an Olympic athlete. So a first order system with a time constant $\tau_a = 0.1s$ has been written, which means a cut-off frequency of $10Hz$.

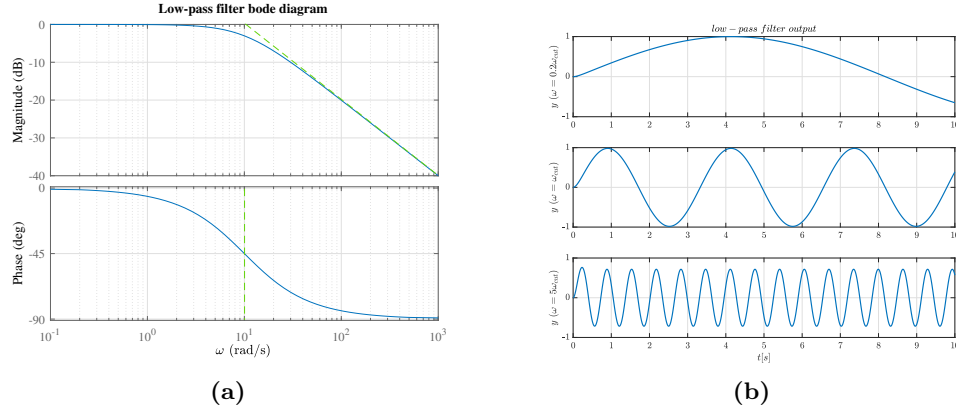


Figure 71: Actuators' Bode diagram (a) and outputs to three unit sine waves: $\omega_{cut-off}$, $0.1\omega_{cut-off}$ and $10\omega_{cut-off}$ (b).

Since now, the general aim has been to design a type 1 control system, that stabilises and allows the control of the iQfoil. This justify the double loop chosen structure which is inspired by a common scheme for aircraft autopilots [21]. The inner loop is optimised to stabilise the unstable modes and to increase performances in reaching the set point. While the outer loop allows to define more than one desired condition and to reach it with a steady-state error equal to zero. This last affirmation is supported by Murray's job [23] and it can be easily demonstrated.

Form Figure 70 the following expressions can be deduced:

$$\begin{aligned}
 \bar{y} &= \bar{C}\bar{x}; \\
 \bar{x}s &= \bar{A}\bar{x} + \bar{B}\bar{G}_a\bar{u}; \\
 \bar{u} &= \bar{K}\bar{x} + \bar{K}_i\bar{x}_i; \\
 \bar{x}_i &= \frac{\bar{e}}{s}; \\
 \bar{e} &= \bar{r} - \bar{y}; \\
 \bar{G}_a &= \frac{1}{\tau_a s + 1};
 \end{aligned} \tag{36}$$

If K_i and B are invertible, the previous equations can be combined such as:

$$\begin{aligned}
 \bar{x}s &= \bar{A} + \bar{B} \left(\bar{K}\bar{x} + \bar{K}_i\bar{e}\frac{1}{s} \right) \\
 \bar{e} &= \bar{K}_i^{-1}\bar{B}_i^{-1} \left(\bar{I}s - \bar{A} - \bar{B}\bar{K} \right) s\bar{x};
 \end{aligned} \tag{37}$$

If the athlete is trying to reach an equilibrium point from another one, through a sequence of states described by finite variables only, which is a weak assumption, the final value theorem can be applied.

$$\begin{aligned}\lim_{t \rightarrow \infty} e(t) &= \lim_{s \rightarrow 0} e(t)s = \bar{K}_i^{-1} \bar{B}_i^{-1} (\bar{I}s - \bar{A} - \bar{B}\bar{K}) s^2 \bar{x} \\ \lim_{t \rightarrow \infty} e(t) &= 0;\end{aligned}\quad (38)$$

The value of the limits is null, and so the steady state error of the illustrated system.

8.2 Gains matrix choice

The choice of K and K_i has been influenced by the absence of handling performance data about the athletes. Moreover, the existence of ten state variables, and no evident uncoupling makes a pole placement process unsuitable. For this reason, a method that allowed to handle with quantities with a direct physical meaning has been chosen: the LQR control[24]. The LQR structure feeds back a full state vector and multiplies it by a gain matrix K optimised according to performance and actuators effort. What this means is defined by two arbitrary matrices, Q and R , which vary according to the admissible worst values of each state variable and control quantity. The minimised function is[24]:

$$J = \int_0^\infty \bar{x}^T \bar{Q} \bar{x} + \bar{u}^T \bar{R} \bar{u} dt \quad (39)$$

The matrix P is now defined such as $P^T = P$ and the term $\bar{x}_0^T \bar{P} \bar{x}_0$ is added and subtracted from eq 39:

$$\begin{aligned}J &= \bar{x}_0^T \bar{P} \bar{x}_0 - \bar{x}_0^T \bar{P} \bar{x}_0 + \int_0^\infty \bar{x}^T \bar{Q} \bar{x} + \bar{u}^T \bar{R} \bar{u} dt \\ J &= \bar{x}_0^T \bar{P} \bar{x}_0 + \int_0^\infty \frac{d}{dt} (\bar{x}^T \bar{P} \bar{x}) \bar{x}^T \bar{Q} \bar{x} + \bar{u}^T \bar{R} \bar{u} dt \\ J &= \bar{x}_0^T \bar{P} \bar{x}_0 + \int_0^\infty \left[(\bar{A} \bar{x} + \bar{B} \bar{u})^T \bar{P} \bar{x} + \bar{x}^T \bar{P} (\bar{A} \bar{x} + \bar{B} \bar{u}) \right] \bar{x}^T \bar{Q} \bar{x} + \bar{u}^T \bar{R} \bar{u} dt \\ J &= \bar{x}_0^T \bar{P} \bar{x}_0 + \int_0^\infty \bar{x}^T (\bar{A}^T \bar{P} + \bar{P}^T \bar{A} + \bar{Q}) \bar{x} + \bar{u}^T \bar{R} \bar{u} + \bar{x}^T \bar{R} \bar{u} + \bar{u}^T \bar{R} \bar{x} dt \\ J &= \bar{x}_0^T \bar{P} \bar{x}_0 + \int_0^\infty \bar{x}^T (\bar{A}^T \bar{P} + \bar{P}^T \bar{A} + \bar{Q} - \bar{P} \bar{B} \bar{R}^{-1} \bar{B}^T \bar{P}) \bar{x} + \\ &\quad + (\bar{u} + \bar{R}^{-1} \bar{B}^T \bar{P} \bar{x})^T \bar{R} (\bar{u} + \bar{R}^{-1} \bar{B}^T \bar{P} \bar{x}) dt\end{aligned}\quad (40)$$

Where the cost function J has been reordered taking into account that $\bar{x}_0^T \bar{P} \bar{x}_0 = -\int_0^\infty \frac{d}{dt} (\bar{x}^T \bar{P} \bar{x}) dt$ and completing the square at the last step.

The final form of eq.41 is composed by constant and quadratic terms, which means that it presents a minimum point where the second ones are null:

$$\begin{aligned}\bar{u} &= -\bar{R}^{-1} \bar{B}^T \bar{P} \bar{x} = -\bar{K} \bar{x} \\ 0 &= \bar{A}^T \bar{P} + \bar{P}^T \bar{A} + \bar{Q} - \bar{P} \bar{B} \bar{R}^{-1} \bar{B}^T \bar{P}\end{aligned}\quad (41)$$

The way these equations have been presented is such as to make explicit K and the *Riccati equation*. The $lqr()$ function asks in input the constant parameters A , B , Q , R and determines P and consequently K .

8.3 Open loop state-space model

If the actuators and the integrators in fig. 70 are considered, the A and B matrices in *Riccati equation* are not yet those of plant state-space model. Hence the need for an open-loop linear model arises. Unlike plant linearisation, the open loop system is better suited for an augmented matrix approach. First of all, the state variables vector is expanded as follows.

$$\bar{x}_a = \begin{Bmatrix} \bar{x} \\ \bar{\delta}_a \\ \bar{x}_i \end{Bmatrix} \quad (42)$$

At this point, the relationships in eq. 36 are to recall and the last one can be rewritten as:

$$\begin{aligned} \delta_a &= \bar{G}_a \bar{u} \\ &\Updownarrow \\ \dot{\delta}_a &= -\frac{1}{\tau_a} \delta_a + \frac{1}{\tau_a} \bar{u} \\ \bar{x}_i &= \frac{1}{s} (\bar{r} - \bar{y}) \\ &\Updownarrow \\ \dot{\bar{x}}_i &= \bar{r} - \bar{y} \end{aligned} \quad (43)$$

$$\begin{aligned} \dot{\bar{x}}_a &= \bar{A}_a \bar{x}_a + \bar{B}_a \bar{u} + \bar{G} \bar{r}; \\ \begin{Bmatrix} \dot{\bar{x}} \\ \dot{\delta}_a \\ \dot{\bar{x}}_i \end{Bmatrix} &= \begin{bmatrix} \bar{A} & \bar{B} & \bar{0}_{10 \times 4} \\ \bar{0}_{4 \times 4} & -\frac{1}{\tau_a} \bar{I}_{4 \times 4} & \bar{0}_{4 \times 4} \\ -\bar{C} & \bar{0}_{4 \times 4} & \bar{0}_{4 \times 4} \end{bmatrix} \begin{Bmatrix} \bar{x} \\ \bar{\delta}_a \\ \bar{x}_i \end{Bmatrix} + \begin{bmatrix} \bar{0}_{10 \times 4} \\ \frac{1}{\tau_a} \bar{0}_{4 \times 4} \\ \bar{0}_{4 \times 4} \end{bmatrix} \begin{Bmatrix} \bar{u} \end{Bmatrix} + \begin{bmatrix} \bar{0}_{10 \times 4} \\ \bar{0}_{4 \times 4} \\ \bar{I}_{4 \times 4} \end{bmatrix} \begin{Bmatrix} \bar{r} \end{Bmatrix} \end{aligned} \quad (44)$$

The open loop state-space model is now written and it can be computed and given in input to $lqr()$ to solve the *Riccati equation*. Augmented matrices A_a , B_a and G are reported in appendix B after the plant's ones.

8.4 Q and R weights definition

The next step in the control system design is the Q and R definition. the process has been iterative, so at first the goals were robustness and flexibility, then an optimisation process was carried out to achieve transients duration comparable to those of an Olympic athlete and, at last, it has been further refined.

Before of facing the effect of elements changing detected in the first phase are reported below:

		if increased	if decreased
$\bar{Q} = \begin{bmatrix} \bar{x} \\ \delta_a \\ \bar{x}_i \end{bmatrix}$		risk of saturation	more overshoot
		more abrupt response	interconnection between states
		0	0
		more abrupt response	less performance
		more overshoot	

Table 14: Effect in macro-changing in Q matrix.

		if increased	if decreased
$\bar{R} = \begin{bmatrix} \diagdown \\ \bar{u} \\ \diagup \end{bmatrix}$			more overshoot
		less performance	more abrupt response more interconnected states

Table 15: Effect in macro-changing in R matrix.

In table 14 two 0 appear due to the non-direct relationship between δ_a and performances. The only requirement on those state variables is actually imposed through the saturation blocks and R . It is advisable to act on u instead of δ_a because by penalising high values of the first, the actuators transfer function effect is damped.

How much to penalise the error on a variable with respect to another one is a more complex argument. For example, to ensure system stability it is important to assign a correct weight to the angle ratios p , q and r . On the other hand, it is necessary to reach the equilibrium independently by the velocity, so that it can increase without any constraint. The values of each element of Q matrix have been found by a *trial-error* method and, because of this, they were constantly in question. The choice is simpler when it regards R elements. It is

necessary to greatly penalise the athlete position displacement because the linearised model taken in input by $lqr()$ does not take into account the saturation eventuality. Due to the states' coupling, the sail position displacement must be low too, even if not in the same way. The power of the sail, instead, can vary without any specific requirement. Indeed, the linearised model considers that for too low values there is no trust enough and a fully powered sail is detrimental at high speeds.

The optimization has been carried out likewise in the previous stage, except that there was a robust starting point that allowed to handle the responses and their specifications.

The refinement phase has been brief and it caused only the increase of the R element associated with $power_{sail}$ from 0.01 to 1, because in one case study the sail was powered and depowered too abruptly. In the following figure, its behavior is reported before (*only optimised*) and after (*refined*) the intervention on R .

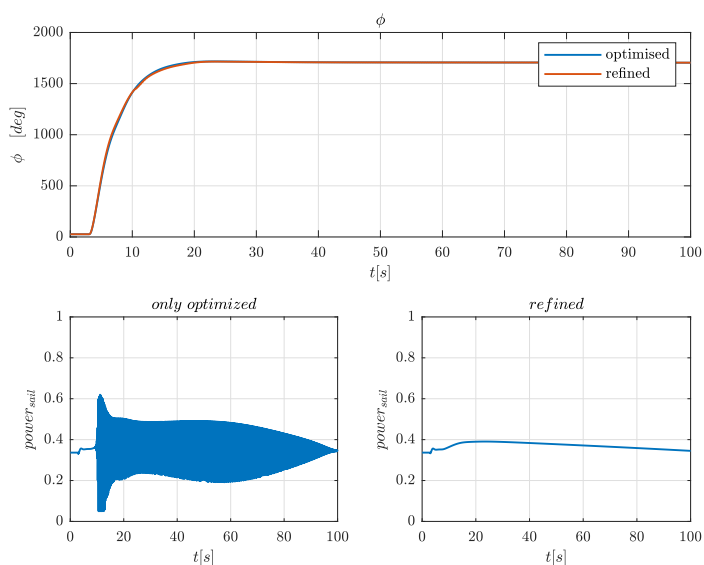


Figure 72: response to roll step command and the sail power trend for the optimised and refined controllers.

For a brevity issue, only two $Q - R$ matrices couples will be now reported: those of the first control system robust and flexible enough, which will be called A , and the refined one, meaning B .

8.5 Case studies

In the previous paragraph the *trial-error* method for the weights definition. What stands between the trial matrices and their valuation is a set of case studies based on plausible regatta commands and external disturbances which will be now explained.

First of all, the three commands involve an altitude change, a roll manoeuvre, and two subsequent turns. all of these are thought to be plausible but extreme so the control system was effectively challenged. For what concerns the roll manoeuvre, it is the only one that happens when sailing upwind, because in this condition is feasible to sail more rolled than in the others, for the model such as for the real athletes. So a wider maneuver could be required for the control system. The turn, instead, is thought to impose the control system to work in all the possible true wind angles to challenge the feasibility of using it for simulating all the regatta segments. The z variations, on the other hand, are not an effective maneuver for an athlete, but it was a necessary case study to test its ability to choose, reach, and keep a desired flight height. To the last element of the integral variables vector, meaning the sideslip angle β , no case studies have been assigned because is implausible that the athlete chose a specific sideslip angle, but it is necessary to observe that he could keep it during and after the aforementioned maneuvers.

The possible disturbances acting on an iQfoil regard wind magnitude and angle and sea waves. The wind can present both lack and gust, as well as its intensity can be strongly irregular. The angle too can vary randomly about mean values or feel abrupt radical changes. In the next list will be provided specifications and a demonstration of how these conditions have been modeled.

8.5.1 Disturbance on true wind angle

A kind of disturbance that can act on a sail is a sudden change of wind direction. It can vary continuously and randomly for a range of time or permanently. Both these two conditions have been simulated, the first through random distribution of TWA_n around a mean value μ in a range of $[\mu - 10^\circ ; +10^\circ + \mu]$. In the following graph, the evolution of the true wind angle through time when sailing beam reaching ($\mu = 90^\circ$) is reported.

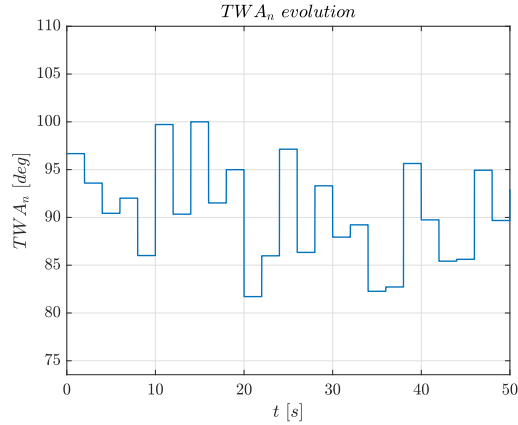


Figure 73: Evolution through time of an irregular wind direction.

The second kind of wind direction disturb has been simulated as a doublet on true wind angle. The ΔTWA_n is greater but more time passes between the wind rotations. In the modeled doublet the wind angle rotates from $TWA_n = 90^\circ$ to 70° , then to 110° and at last it returns to the initial values.

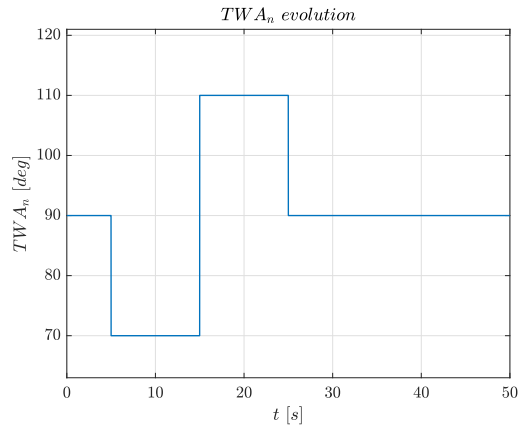


Figure 74: Evolution through time of wind direction doublet.

8.5.2 Disturbance on wind intensity

The model of wind angle disturbances has been repeated on its intensity too. The random distribution of wind speeds has a mean value $\mu = 20$ and varies in a range of $[-5Kn; +5Kn]$. The doublet, instead, imposes to the wind a change of $\pm 7.5^\circ$ with the same timing of that on TWA_n .

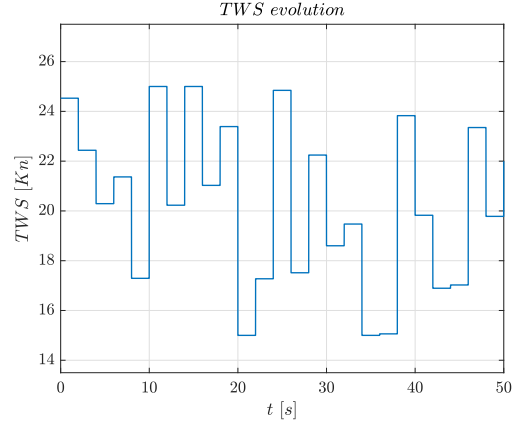


Figure 75: Evolution through time of an irregular wind intensity.

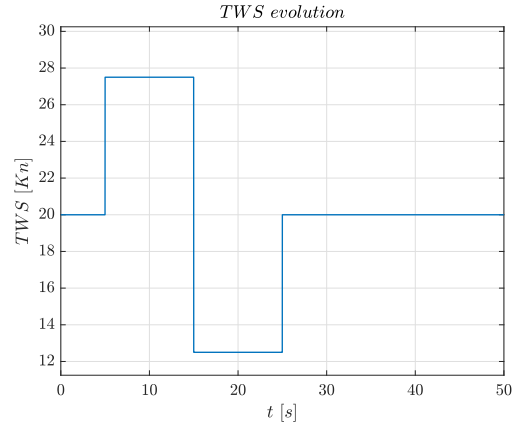


Figure 76: Evolution through time of an wind intensity doublet.

8.5.3 Disturbance due to sea waves

The model used in this section refers to the linear theory of ocean surface waves [25] and it describes the typical sea wave as a sine curve which depends on the considered moments and position of the measurement.

$$\zeta_{wave} = A \operatorname{sen} \left(\frac{2\pi}{\lambda} x - \frac{2\pi}{T} t \right); \quad (45)$$

The point x where it is interesting to measure the sea surface elevation ζ is the iQfoil position, which depends on its speed and time. Hence, if x can be expressed as a function of t , only one independent variable remains:

$$\zeta_{wave} = 2\pi A \operatorname{sen} \left(\left(\frac{1}{\lambda} U - \frac{1}{T} \right) t \right); \quad (46)$$

The waves have been introduced in the model as a disturbance summed to the incidence. Starting from eq. 46, it is possible to derivate and obtain the iQfoil's vertical velocity with respect to a sea surface fixed reference system.

$$\dot{\zeta}_{wave} = 2\pi A \left(\frac{U}{\lambda} - \frac{1}{T} \right) \operatorname{sen} \left(2\pi \left(\frac{U}{\lambda} - \frac{1}{T} \right) t + \frac{\pi}{2} \right); \quad (47)$$

In order to evaluate the scale of the disturbance, the specifications assumed in the simulations are now reported. They have been chosen as strictly conservative based on FIV coaches and bibliography[25].

λ	=	50m
T	=	6s
A	=	0.25m

Table 16: Waves assumed specifications.

The small angle assumption will be considered since now, at the end of the procedure it will verified:

$$\begin{aligned} \alpha &= \operatorname{arctg} \left(\frac{w+\dot{\zeta}}{u} \right) \approx \alpha_0 + \frac{\dot{\zeta}}{u}; \\ \Delta\alpha &= 2\pi A \left(\frac{1}{\lambda} - \frac{1}{TU} \right) \operatorname{sen} \left(\left(\frac{1}{\lambda} - \frac{1}{TU} \right) t + \frac{\pi}{2} \right); \end{aligned} \quad (48)$$

If the values in table 16 are inserted in eq. 48 the result is $\Delta\alpha = 0.183\operatorname{rad} = 10.44^\circ$, validating the previous hypothesis.

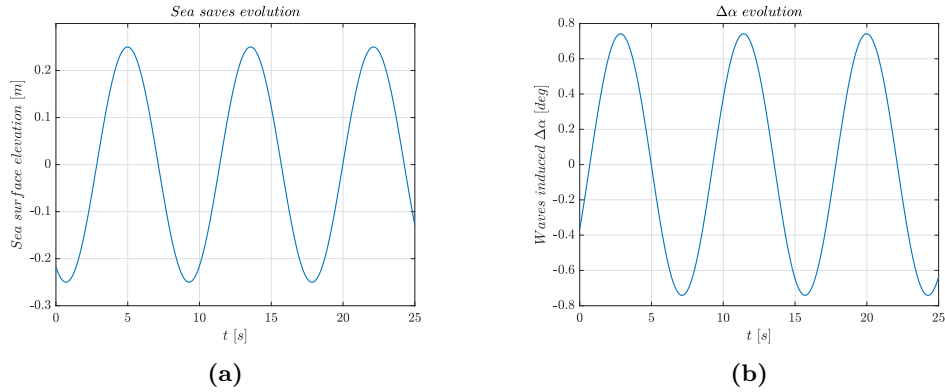


Figure 77: Sea waves evolution through time (a) and the induced $\Delta\alpha$ (b).

8.6 Results

In this section, all the aforementioned case studies' results will be discussed. For each of them z , ϕ e ψ will be exposed, to show the behavior of iQfoils. For the most interesting ones, eventual other quantities' evolution in time can be reported.

8.6.1 Wind angle disturbances

The results discussion starts with the application of a random oscillation of the wind angle about a mean value. As expected, the refined controller reduces the state variables variation due to the irregular external condition.

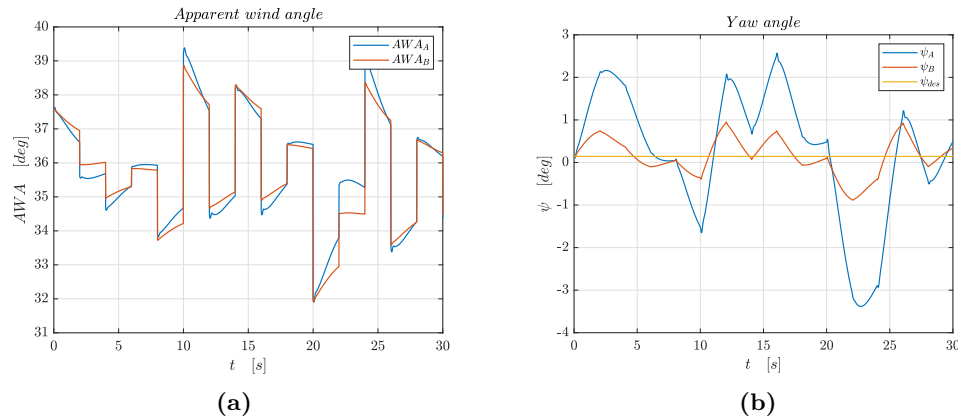


Figure 78: AWA (a) and ψ (b) evolution under a random wind angle variation.

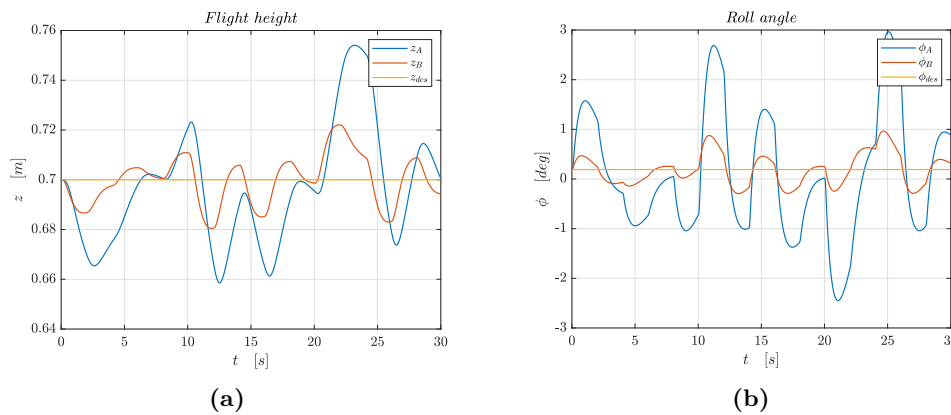


Figure 79: z (a) and ϕ (b) evolution under a random wind angle variation.

In figures 80a it can be noticed the relationship between apparent wind and yaw angles.

When the wind angle changes, the sail produces a different lift along a different direction. This breaks the equilibrium condition, causing the iQfoil to yaw. The controller tends to restore the $\psi = 0$ condition, so the position discontinuities for TWA and AWA graphs preclude the ψ first derivative continuity. Moreover, the yaw angle and AWA assume almost the same trend but inverted. This happens because of the strict relationship between AWA and TWA, which can be interpreted as the yaw angle with respect to the wind instead of the north.

$$\begin{aligned} TWA &= TWA_n - \psi; \\ AWA &= \operatorname{atg} \left(\frac{TWS \operatorname{sen}(TWA)}{TWS \operatorname{cos}(TWA) + U} \right); \end{aligned} \quad (49)$$

The same behaviour can be observed after a step true wind angle disturbance:

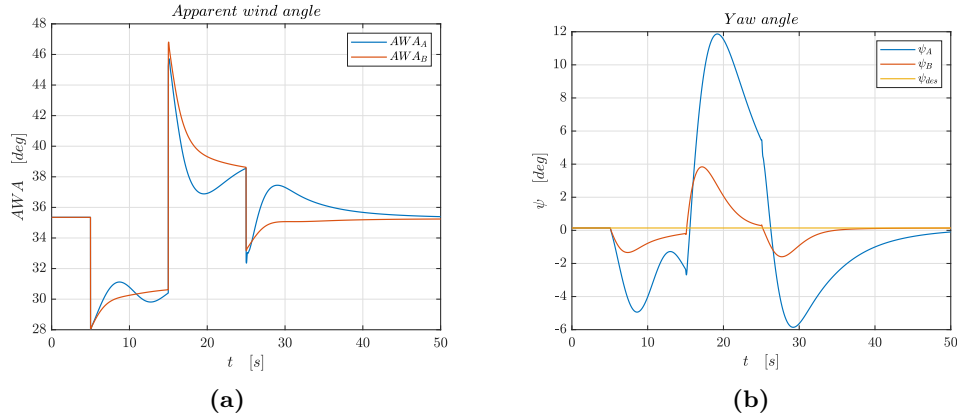


Figure 80: AWA (a) and ψ (b) evolution after a doublet wind angle variation.

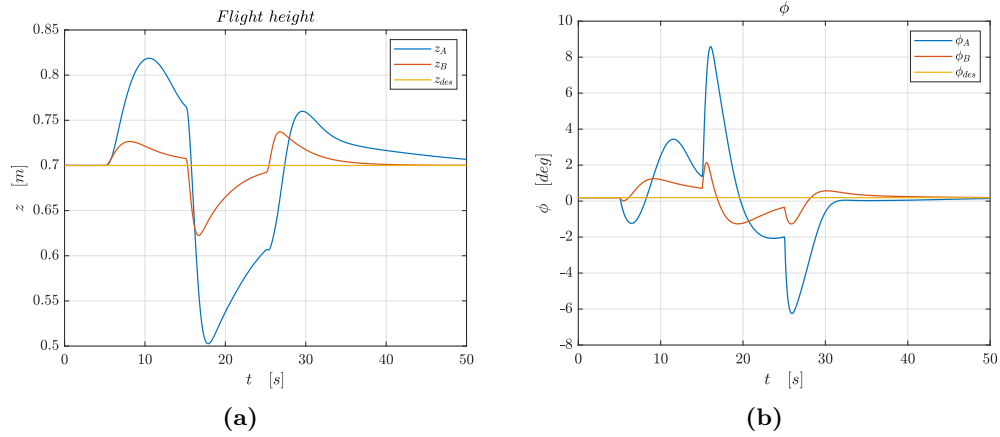


Figure 81: z (a) and ϕ (b) evolution after a doublet wind angle variation.

8.6.2 Wind speed disturbances

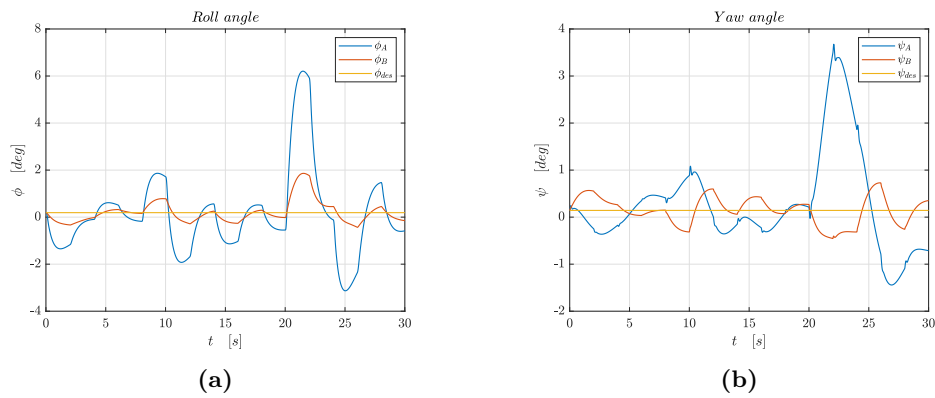


Figure 82: ϕ (a) and ψ (b) evolution during a random wind speed variation.

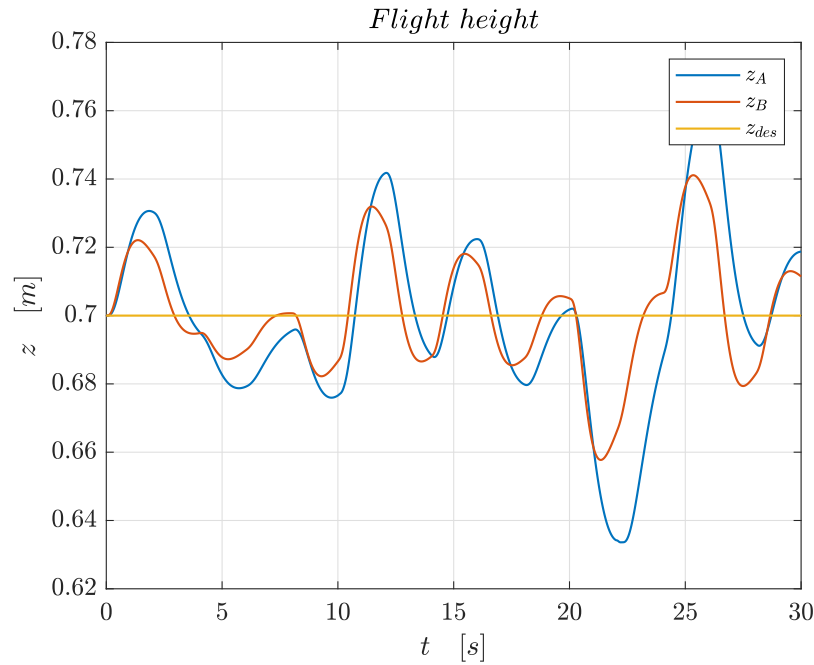


Figure 83: z evolution during a random wind speed variation.

What draws the attention of the previous figures is the flight height trend with respect to that in fig. 75. Actually, higher wind speeds cause higher altitudes. For this reason, gusts are between over-lift causes.

Below the response to a doublet gust-lack are reported:

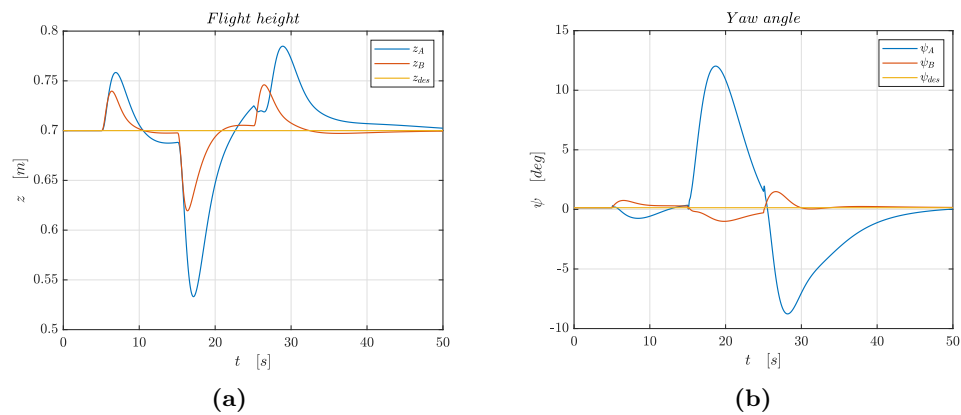


Figure 84: z (a) and ψ (b) evolution after a doublet wind speed variation.

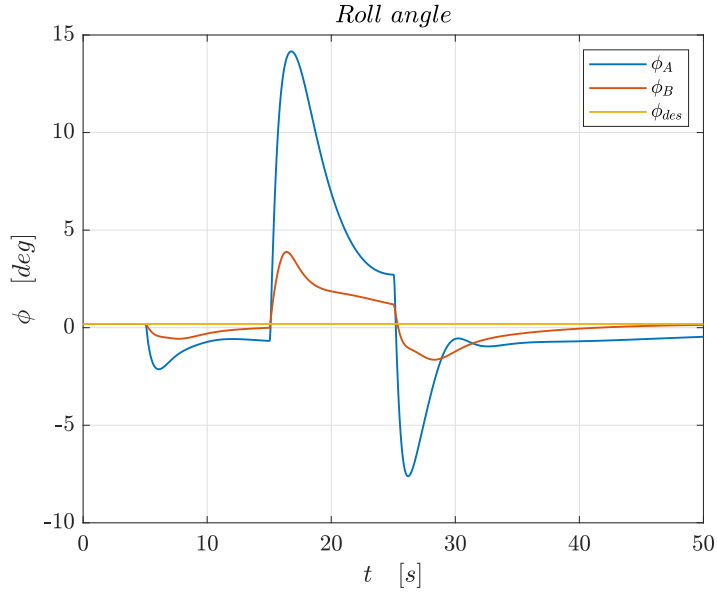


Figure 85: ϕ evolution after a doublet wind speed variation.

In ϕ evolution, an inverted behavior with respect to z can be seen. Indeed, as a gust causes an increase of trust and so of speed, lift and, at last, vertical speed, it is also responsible for a greater lateral force by the sail, that applies a roll moment to the iQfoil. For the right-hand convention, if the roll rate goes from the athlete to the sail, ϕ decreases, reason why it is negative when $z > 0.7m$ and vice-versa.

8.6.3 Sea waves effect

Thanks to FIV athletes' experiences, it is known that iQfoil damps sea waves effect. This is coherent with what results from the previously described waves model and the relative simulation.

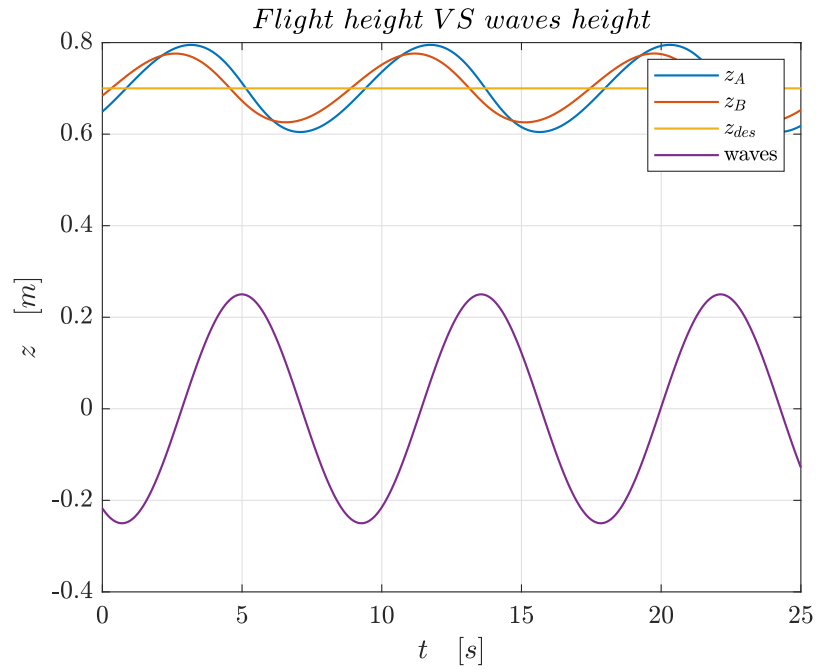


Figure 86: Sea waves effect on flight height.

The phase difference between the sea surface oscillation and those of iQfoil is about 90° , which can be explained considering by the derivative in eq.47. The difference between controllers A and B is less impressive than in the previous cases because the intervention of the athlete to react to waves is almost not required.

8.6.4 Roll step command effect

The first command-related case study faced in this section is the roll step command response. In this simulation the desired roll angle became 30° from 0.

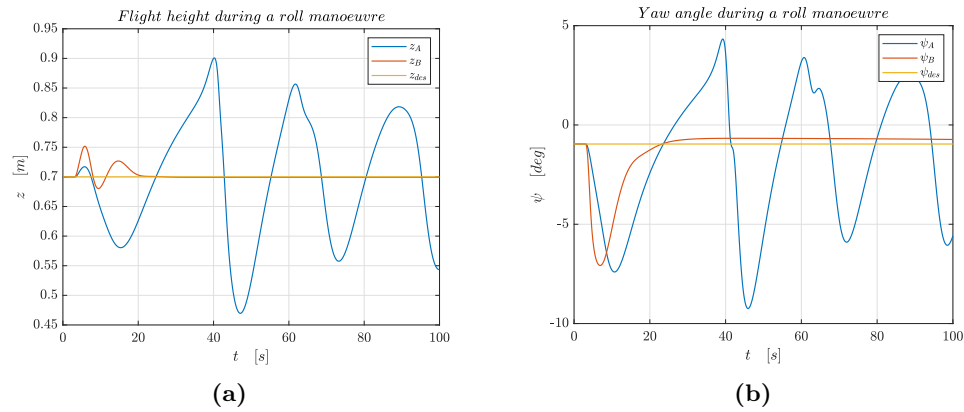


Figure 87: z (a) and ψ (b) evolution after a 30° roll step command.

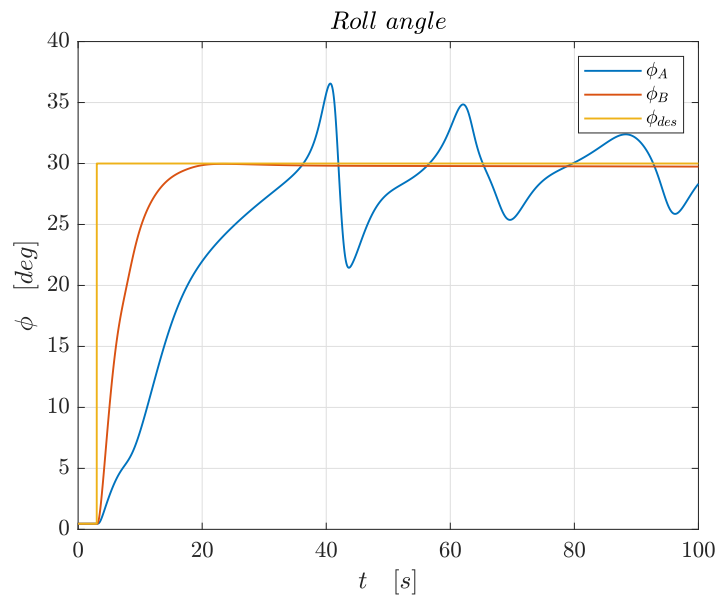


Figure 88: ϕ evolution after a 30° roll step command.

Controller B's superiority is evident from previous graphs. The roll angle has both faster and stable behavior while ψ and z are less affected by the exit from the initial condition. The lack of controller A is felt in both measuring overshoots and characteristic times. In particular, referring to ϕ :

	A	B
Delay time	10.8s	3.1s
Rise time	8.9s	26.7s
Settling time	//	11.2s
Overshoot	22%	//

Table 17: Time domain specification about a 30° roll step command.

About this case study, another observation can be made. Looking at the sideslip angle response, it is possible to notice that it decreases after the roll manoeuvre, coherently with what is observed in real life. Indeed, the sideslip angle is controlled keeping the correct roll angle so that the foil lift presents a projection on the horizontal plane equal to or greater than the sail lateral force. Usually, positive sideslip angles only are a problem, while negative ones allow to reach the next buoy faster. In section 8.5, it has been mentioned that this is the only case study faced assuming to sail upstream. This is because when the AWA is small, a great component of the sail lift is parallel to the y-axis, reason why it is more common to fly rolled.

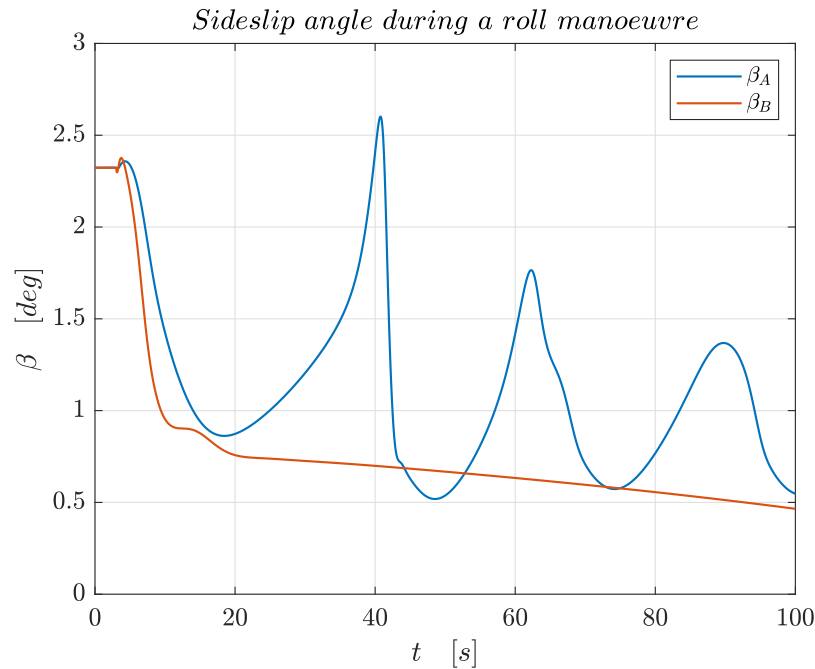


Figure 89: β evolution after a 30° roll step command.

8.6.5 Yaw step commands effect

The Yaw step commands case study has been used both for measuring time domain specifications of controllers A and B and for testing their effectiveness in all the plausible wind angles range. Hence, the commands imposed to the iQfoil require A turning manoeuvre from $TWA = 90^\circ$ to $TWA = 145^\circ$ and then $TWA = 55^\circ$.

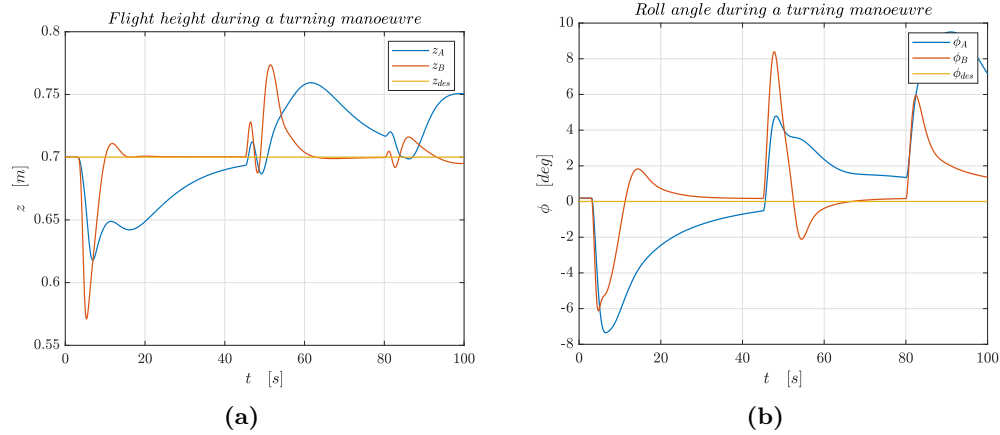


Figure 90: z (a) and ϕ (b) evolution after a two turn step command.

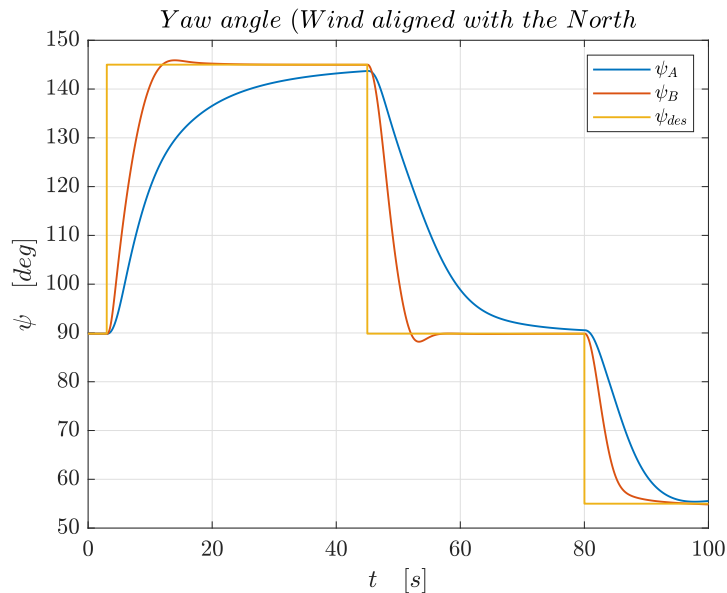


Figure 91: ψ evolution after a two turn step command.

In this case, the response of controller A is better than after a roll command, but still worse than that of controller B. Looking at z and ϕ responses, controller B causes greater changes with respect to the set point, however, the peak values are acceptable and it ensures a faster settling to the desired condition. This time too the time domain specifications have been determined. About the following table, it is important to mind that the last two turning manoeuvres are affected by the previous history.

	A	B
Delay time	6.4s	3.2s
	7.9s	3.4s
	6.0s	3.0s
Rise time	21.8s	6.5s
	17.6s	5.8s
	11.5s	5.8s
Settling time	29.8	7.4s
	21.9s	6.3s
	13.2s	7.3s
Overshoot	//	1.63%
	//	3.22%
	//	//

Table 18: Time domain specification about a two turn step command.

An interesting quantity to observe in this situation is the longitudinal position of the sail's centre of pressure. Moving the sail back and forward, the athlete acts on the yaw equilibrium, achieving the chance to ensure or perturb it according to circumstances. In order to reach the final condition, both controllers must bring the sail in the same position, although, they give discordant first inputs. The movement determined by controller B matches better the behavior of a real athlete, which provides another reason to consider it the best of them.

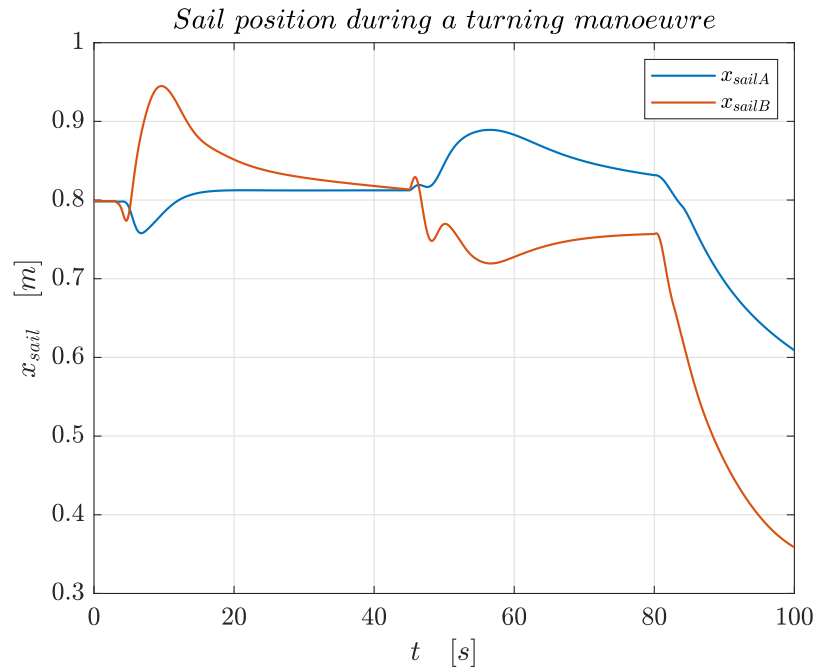


Figure 92: x_{sail} evolution after a two turn step command.

8.6.6 descending step command effect

In section 5 the effect of flight height on over-lift prevention has been explained. The analysis of a descending manoeuvre is useful to understand the effectiveness of the athlete in determining the longitudinal attitude. In the following figures, an altitude decrease of $0.2m$, from $0.7m$ to $0.5m$, will be studied.

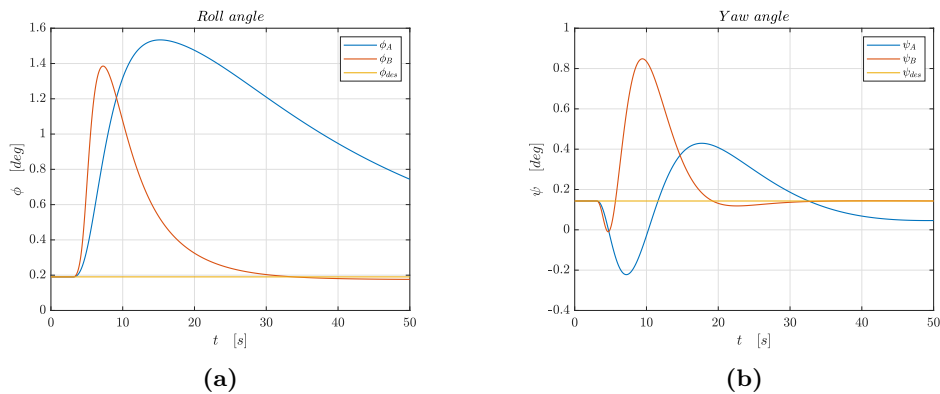


Figure 93: ϕ (a) and ψ (b) evolution after a descending step command.

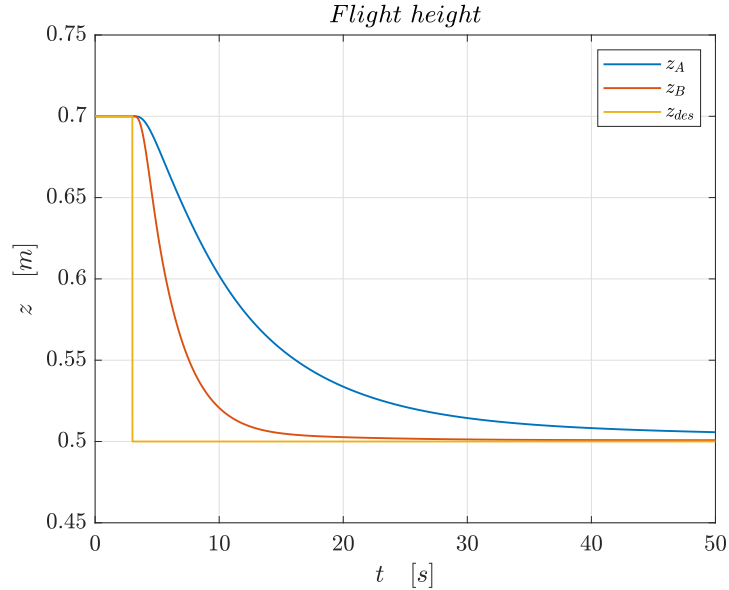


Figure 94: Altitude through time after a descending step command.

	A	B
Delay time	7.0s	2.7s
Rise time	22.6s	7.1s
Settling time	34.9s	9.3s
Overshoot	//	//

Table 19: Time domain specification about a descending step command.

At last, the usage of the athlete's weight and its effect on iQfoil's incidence and pitch angle will be faced. The expediencies from the previous models and the background theory predicted a first movement forward by the athlete to reduce the pitch angle and the incidence. Once the down speed is acquired, the incidence must arise, while the pitch angle reaches its lower value because of the negative ramp angle. Finally, when the final condition is reached, the athlete gets in position to keep it. The final position was expected to be further back than at the beginning, and the last analysis has confirmed this conclusion.

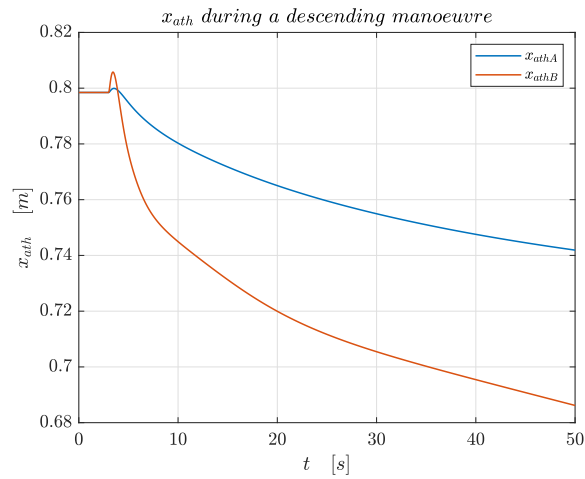


Figure 95: x_{ath} evolution after a descending step command.

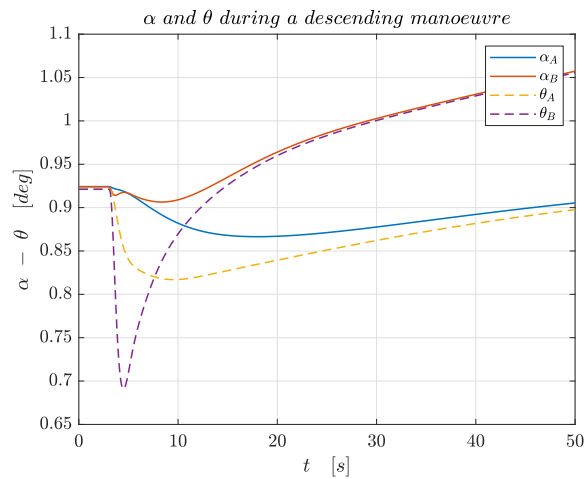


Figure 96: α and θ evolution after a descending step command.

From the graph in figure 95 controller B seems to be more sensible to the flight height, acquiring the chance of reaching higher speeds without over-lifting. In figure 96, it is possible to notice that α and θ are equal in the initial and final conditions when $\dot{z} = 0$. This is due to their relationship:

$$\begin{aligned}\theta &= \alpha + \gamma; \\ \alpha &= \operatorname{arctg} \left(\frac{w}{u} \right); \\ \gamma &= \operatorname{arctg} \left(\frac{\dot{z}}{\dot{x}} \right); \end{aligned} \tag{50}$$

These equations can be interpreted by noticing that the meanings of α and γ are similar, except that the speeds in their definitions are referred respectively to body and ned reference systems. This justifies the presence of θ , which, together with ϕ and ψ , describes the orientation of the two systems the one respect to the other.

Since both initial and final conditions require $z = \operatorname{cost}$, what is mentioned above is coherent with the theory. In the intermediate instants, the difference between the incidence and the pitch angle must have a negative value. The area enclosed between the two curves is related to the altitude change: the more it is distributed along the time, the less steep the descent is, as shown by controller A curves in graphs 94 and 96.

8.6.7 Graphical representation

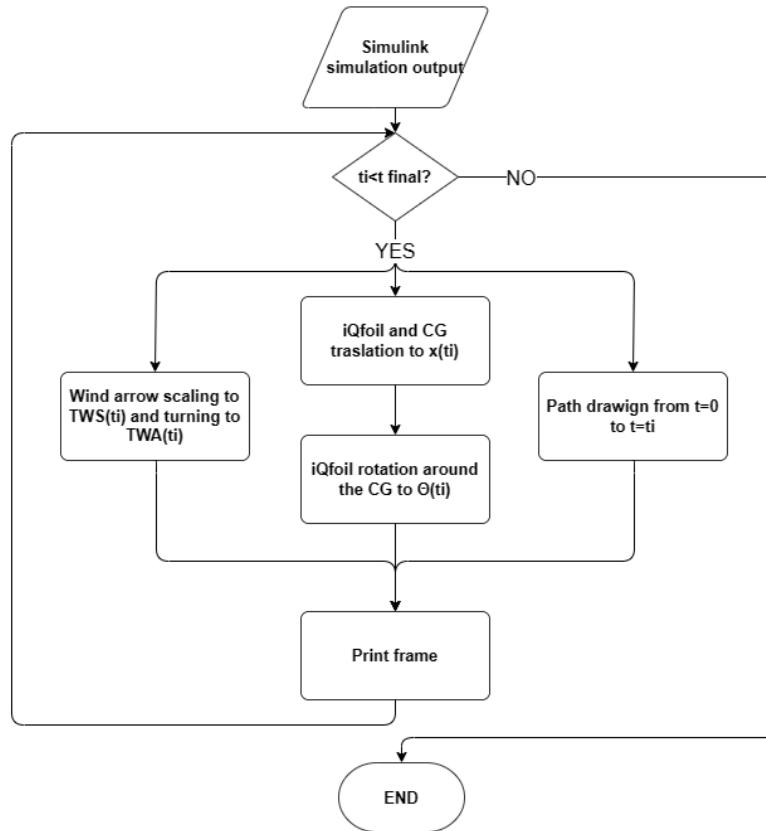


Figure 97: Graphical representation tool flowchart.

A further result of this work has been the graphical representation of iQfoil motion, which has been implemented on *Grasshopper*. The script draws from Simulink simulation output and rebuilds for each time step the current state and prints a frame on the computer memory. The frames can be combined in a video that shows the physical meaning of the graphs reported in this section. Moreover, the tool allows to compare the attitude of the iQfoil to the Simulink scopes and the path observed from above.

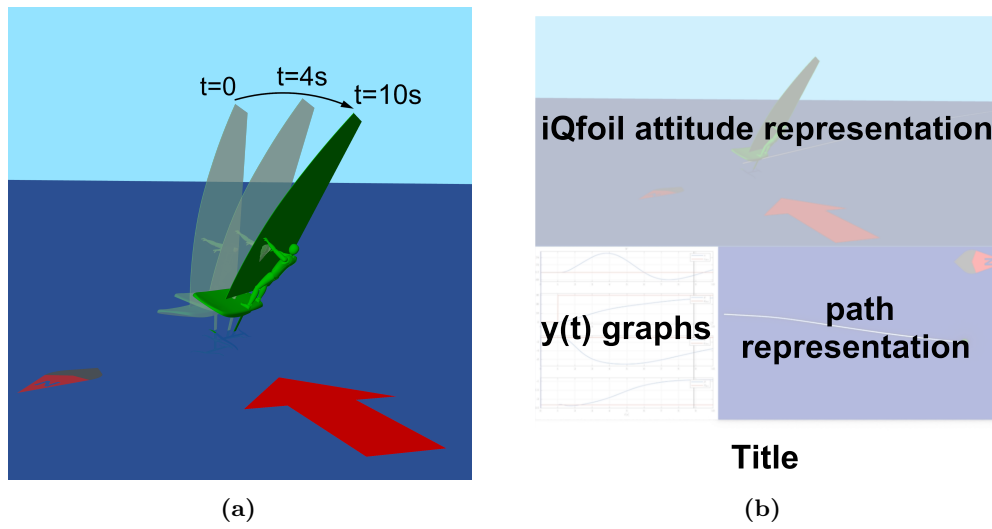


Figure 98: Graphical representation of the roll manoeuvre treated in par. 8.6.4 (a) and the frame structure (b).

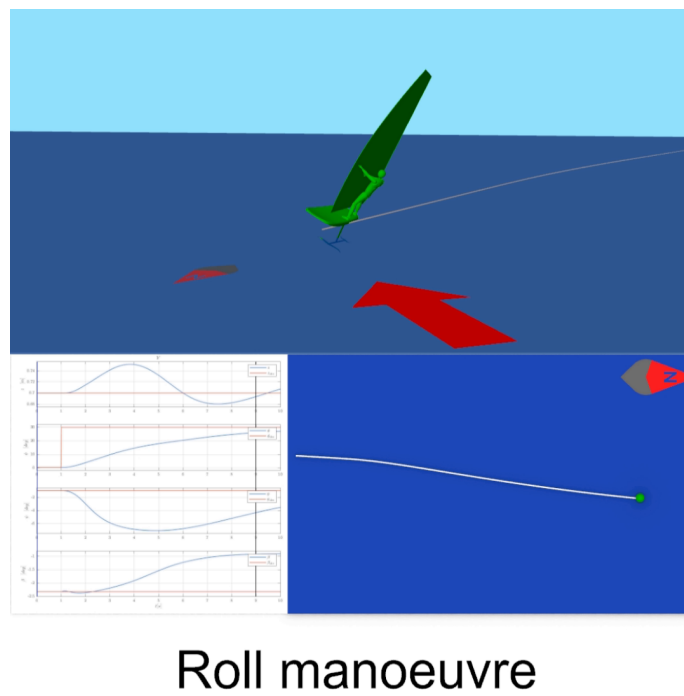


Figure 99: Screenshot of the output video.

9 Conclusion and Future Works

The outputs of this thesis are distributed through the chapters, reason why it is advisable to make a summary. Starting from a physical iQfoil, a dynamic 6DOF model has been achieved, and the intermediate steps, necessary to carry on the work, constitute some important results.

Between them, the maps provided to FIV can be an important support to **the Olympic athletes training**. The comprehension of the effects of the settings to a deeper level allows a more methodical use of them and a saving of time for the team. Although, the greatest achievement of this collaboration lies in the talks we had, a precious chance to understand iQfoil behavior before modeling it.

In addition, the **geometric model** has been produced. it gave the chance to compute the necessary inertial properties and to prepare the geometries for the following fluidynamic analysis. Thanks to the CAD file, to understand the relationships between various quantities, for example the sensitivities of inertia and centre of gravity with respect to the athlete position and the board rake have been quantified.

The fluidynamic investigation of components' aerodynamic derivatives led to a fundamental output for carrying on the work, but also to explain the magnitude orders of each contribution to Olympic coaches, who needed them to choose where it is more valuable to focus. Thanks to the use of **macro script applied to CFD**, the dependencies on more quantities at the same time have been determined and interpolated

Then, the 6DOF plant model led to the **linearisation of iQfoil motion**. The eigenvalues and vector analysis have been necessary to investigate the states coupling. Without this step, the development of the subsequent controllers would not have been possible.

Finally, some controllers have been implemented, so as to simulate the iQfoil flight, despite not having an athlete movement model. The optimisation led to a control system that **emulates the real-life performance**. The last results has been the time response to various commands and external disturbances and, in the end, their graphical representation.

Despite all the goals achieved, a lot of margin of improvement can be taken into account. The control system itself would be interesting to better compare to athletes' behavior. Hence, an **experimental campaign** would be the chance to install sensors on them and record the reaction to inputs. Moreover, The comparison of different athletes' usage of their weight and the sail would allow to understand how many ways can lead to similar flights and which of them are advisable to prevent over-lifting phenomena.

Between the aims of such an experimental campaign could be a **pumping model**, meaning a description of that athlete movement that forces iQfoil longitudinal dynamic in order to achieve an alternate increase of speed and incidence and anticipate the take-off. To reach this result, a study of the board's hydrodynamic coefficients when it interacts with both air and water would be necessary, as well as a modelisation of its hydrostatic behavior, meaning the dependency of its buoyancy centre on its attitude.

References

- [1] *The iQfoil Story*. <https://www.windsurf.co.uk/the-iqfoil-story/> (cit. on p. 12).
- [2] *Paris 2024: What is iQFOiL, the new Olympic sailing board replacing RS:X?* <https://olympics.com/en/news/paris-2024-what-is-iqfoil-new-olympic-sailing-board-rs-x> (cit. on p. 12).
- [3] *The PoliTo Sailing Team*. <https://areeweb.polito.it/politosailingteam/> (cit. on p. 12).
- [4] K Alexander and V Furniss. “Systematic Measurements of a Windsurfer Sail Performance”. In: *13th Australian Fluid Mechanics Conference* (1998), p. 4 (cit. on pp. 12, 27, 60, 61).
- [5] *iQfoil class official website*. <https://www.iqfoilclassofficial.org/> (cit. on pp. 14, 17, 18).
- [6] *Rhino User’s Guide for Windows*. <https://docs.mcneel.com/rhino/6/usersguide/en-us/index.htm> (cit. on p. 21).
- [7] *Grabcad*. <https://grabcad.com/library> (cit. on p. 23).
- [8] *Mathworks: Matlab documentation*. <https://it.mathworks.com/help/matlab/> (cit. on pp. 24, 33).
- [9] *Python website*. <https://it.mathworks.com/products/simulink.html> (cit. on pp. 24, 73).
- [10] TJ Schmitt. “Wind-Tunnel Investigation of Air Loads on Human Being”. In: (1964), p. 67 (cit. on p. 27).
- [11] *XFLR5 documentation*. <http://www.xflr5.tech/xflr5.htm> (cit. on pp. 27, 37).
- [12] *STAR CCM+ home page*. https://starccm.smartcae.com/?gad_source=1&gclid=Cj0KCQjwhL6pBhDjARIsAGx8D58FbKJ_bHUM_RMbrnMjHm4I3cYTQt3jVE9AJPWe_Dds6bZpZn8XyZcaAi5mEALw_wcB (cit. on p. 27).
- [13] *Grasshopper documentation*. <https://developer.rhino3d.com/guides/grasshopper/> (cit. on p. 27).
- [14] Renzo Arina. *Fondamenti di Aerodinamica*. Torino: Levrotto Bella, 2015 (cit. on p. 37).
- [15] Milovan Perić Joel H. Ferziger. *Computational Method for Fluid Dynamic*. Springer, 2002 (cit. on p. 42).
- [16] Hoekstra M. Eça L. “A procedure for the estimation of the numerical uncertainty of CFD calculations based on grid refinement studies”. In: (2014), p. 27 (cit. on pp. 42, 43).

-
- [17] Dr. Robert C. Nelson. *Flight Stability and Automatic Control*. McGraw-Hill, 1998 (cit. on p. 62).
- [18] Perez Tristan. *Ship Motion Control*. Springer, 2005 (cit. on pp. 63, 69, 70).
- [19] *Matlab guide on GA function*. <https://it.mathworks.com/help/gads/ga.html> (cit. on p. 65).
- [20] *Simulink website*. <https://it.mathworks.com/products/simulink.html> (cit. on p. 68).
- [21] Eric N. Johnson Brian L. Stevens Frank L. Lewis. *Aircraft Control and Simulation*. Wiley, 2016 (cit. on pp. 76, 84).
- [22] Loyd D. Reid Bernard Etkin. *Dynamics of flight - Stability and Control*. JOHN WILEY SONS, INC., 1996 (cit. on p. 79).
- [23] Willems J. C. Young P. C. “An approach to the linear multivariable servomechanism problem”. In: (1971), p. 19 (cit. on p. 84).
- [24] Murray R.M. *LQR Control*. University Lecture. 2006 (cit. on p. 85).
- [25] Steward R. H. *Onde del Mare*. University Lecture. 2007 (cit. on pp. 92, 93).

A 6DOF static model solution method

	A	B	C	D	E	F	G
x_{ath}	0.3036	0.62554	0.4617	0.1432	0.11649	0.46098	0.25959
y_{ath}	0.79468	1.452	1.0158	0.68624	0.67624	1.0193	0.75543
x_{sail}	-0.026358	0.13557	0.047754	-0.09946	-0.11116	0.047341	-0.046097
$sail_p$	0.20142	0.2651	0.2162	0.19655	0.19674	0.21635	0.19913
U	17.4676	25.2936	20.9227	14.7201	14.3372	20.9016	16.6343
ϕ	0.59896	0.49507	0.57921	0.59	0.5759	0.62071	0.59037
θ	3.0385	1.176	1.9612	4.4789	4.7469	1.9646	3.4025
ψ	-0.033508	-0.13667	-0.038788	-0.037257	0.00035891	0.11263	0.0061089
β	-1.8698	-1.5646	-1.6591	-2.2407	-2.3167	-1.6698	-1.955
res_{max}	2.1825e-05	9.9593e-05	2.8076e-05	1.8992e-05	3.5819e-05	4.9405e-05	4.2496e-05
	H	I	J	K	L	M	N
x_{ath}	0.10848	0.53473	0.39366	0.11557	0.26252	0.1099	0.11115
y_{ath}	0.67359	1.1848	0.9021	0.67511	0.75606	0.67384	0.67408
x_{sail}	-0.11521	0.086143	0.016706	-0.11121	-0.043737	-0.11431	-0.11338
$sail_p$	0.19677	0.23554	0.20872	0.19674	0.19927	0.19678	0.1968
U	14.2263	22.7991	19.3564	14.3253	16.6898	14.2462	14.2636
ϕ	0.58226	0.56381	0.54367	0.55856	0.54933	0.57502	0.56585
θ	4.828	1.5683	2.381	4.7564	3.3784	4.8137	4.8013
ψ	-0.03261	0.01711	-0.02917	-0.0097265	0.00425	-0.022453	-0.00048015
β	-2.3416	-1.6073	-1.7254	-2.3144	-1.9408	-2.3357	-2.3301
res_{max}	3.7087e-05	5.6926e-05	2.3405e-05	3.906e-05	2.4312e-05	2.7433e-05	2.7127e-05
	O	P	Q	R	S	T	
x_{ath}	0.35973	0.55938	0.59471	0.49048	0.11543	0.11267	
y_{ath}	0.85477	1.2507	1.3576	1.0779	0.67526	0.67485	
x_{sail}	0.0014045	0.098602	0.11912	0.062107	-0.11142	-0.11295	
$sail_p$	0.2056	0.2429	0.25521	0.22255	0.19674	0.19677	
U	18.6194	23.4607	24.4358	21.6376	14.3232	14.2842	
ϕ	0.52149	0.57856	0.53158	0.59895	0.56381	0.57481	
θ	2.6159	1.4509	1.297	1.7986	4.7577	4.7856	
ψ	-0.038945	-0.050913	0.015102	0.021027	-0.012415	-0.0085004	
β	-1.7664	-1.5945	-1.5796	-1.6399	-2.3162	-2.3277	
res_{max}	2.1872e-05	4.6788e-05	7.9835e-05	7.202e-05	2.427e-05	2.6098e-05	

Table 20: Solutions for the underdetermined equilibrium problem starting from twenty different points and with no criteria of selection.

	A	B	C	D	E	F	G
x_{ath}	0.65341	0.65352	0.65181	0.65359	0.6534	0.65352	0.65347
y_{ath}	1.497	1.4971	1.4973	1.4972	1.497	1.4971	1.4973
x_{sail}	0.15158	0.15171	0.14948	0.15174	0.15162	0.15177	0.15158
$sail_p$	0.26954	0.26957	0.26924	0.26957	0.26955	0.26958	0.26955
U	26.0576	26.0608	26.0118	26.0624	26.0575	26.0608	26.0592
ϕ	0.071514	0.06635	0.1701	0.065653	0.069605	0.063302	0.073015
θ	1.0911	1.0909	1.0936	1.0907	1.0912	1.091	1.0909
ψ	-0.93247	-0.93386	-0.89385	-0.93625	-0.9302	-0.93156	-0.93389
β	-1.5031	-1.5027	-1.5119	-1.5025	-1.503	-1.5025	-1.5032
res_{max}	0.00025676	0.0002139	0.00046258	0.00025699	0.00026699	0.00018559	0.00018176
	H	I	J	K	L	M	N
x_{ath}	0.65351	0.6535	0.65353	0.65353	0.65342	0.65362	0.65355
y_{ath}	1.4973	1.4972	1.4971	1.4972	1.4974	1.4975	1.4974
x_{sail}	0.15172	0.15163	0.15173	0.15169	0.15155	0.15175	0.15168
$sail_p$	0.26959	0.26955	0.26957	0.26957	0.26956	0.2696	0.26958
U	26.0606	26.0599	26.061	26.061	26.0579	26.0633	26.0614
ϕ	0.066906	0.070244	0.065349	0.068088	0.075158	0.067306	0.069272
θ	1.0909	1.0909	1.0909	1.0908	1.091	1.0905	1.0907
ψ	-0.93089	-0.93513	-0.93355	-0.93421	-0.92942	-0.93388	-0.93398
β	-1.5028	-1.5029	-1.5026	-1.5028	-1.5035	-1.5027	-1.5029
res_{max}	0.0001007	7.9133e-05	0.00011808	0.00012671	0.00010464	9.8262e-05	0.00010414
	O	P	Q	R	S	T	
x_{ath}	0.65359	0.65318	0.65354	0.65342	0.65364	0.65353	
y_{ath}	1.4974	1.4973	1.4973	1.497	1.4974	1.4972	
x_{sail}	0.15165	0.15117	0.1517	0.15161	0.15184	0.15173	
$sail_p$	0.26956	0.26949	0.26958	0.26954	0.26961	0.26958	
U	26.0623	26.0507	26.0611	26.0579	26.0641	26.0609	
ϕ	0.070405	0.092416	0.067831	0.069658	0.061989	0.065832	
θ	1.0906	1.0913	1.0908	1.0911	1.0906	1.0909	
ψ	-0.9378	-0.92717	-0.93343	-0.93289	-0.93414	-0.93239	
β	-1.5028	-1.5049	-1.5028	-1.5029	-1.5023	-1.5027	
res_{max}	0.00013319	0.0002642	0.00010492	6.7101e-05	0.00020608	0.00015445	

Table 21: Solutions for the underdetermined equilibrium problem starting from twenty different points and with the selection criteria based on the weighted objective function.

C Linearisation validation

Below the comparison between the analytic response of the linearised model and the numeric one of the non-linear model are shown.

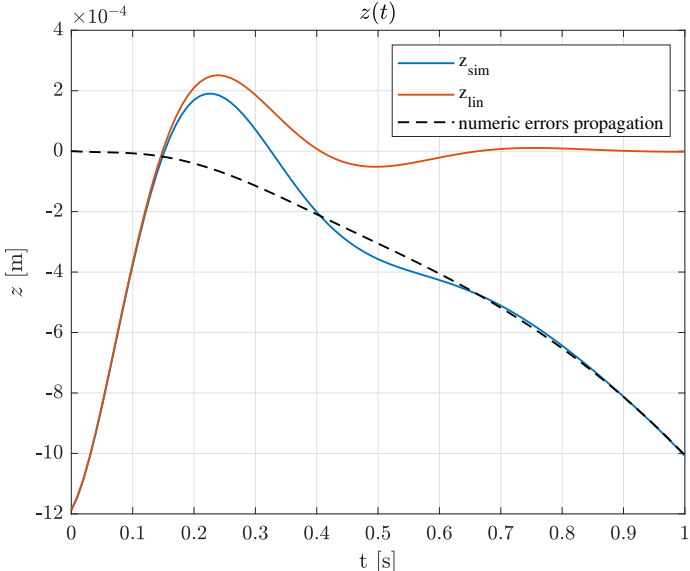


Figure 100: Responses comparison between analytic linearised model and numeric non-linear one - z .

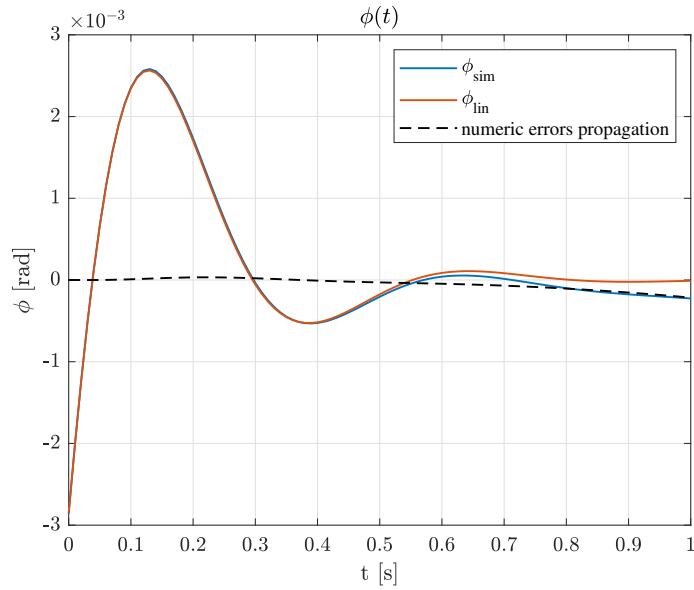


Figure 101: Responses comparison between analytic linearised model and numeric non-linear one - ϕ .

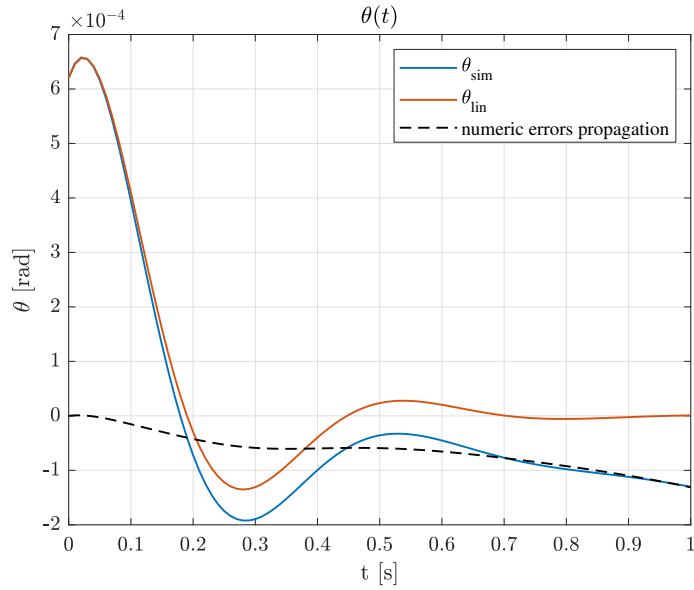


Figure 102: Responses comparison between analytic linearised model and numeric non-linear one - θ .

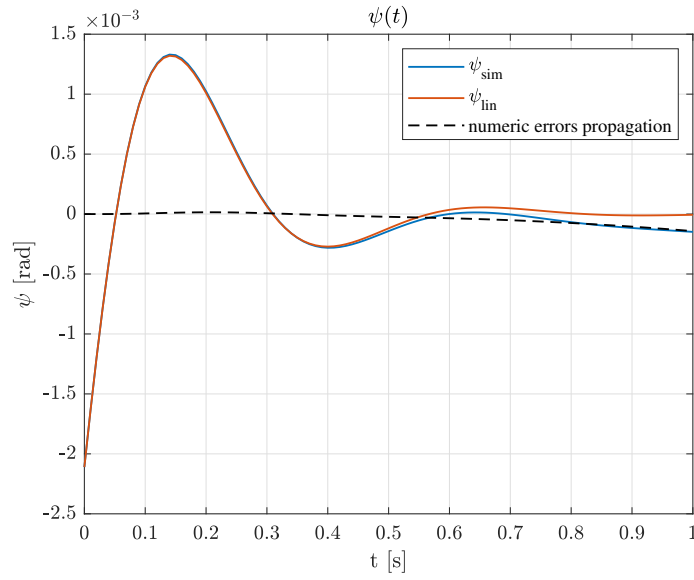


Figure 103: Responses comparison between analytic linearised model and numeric non-linear one - ψ .

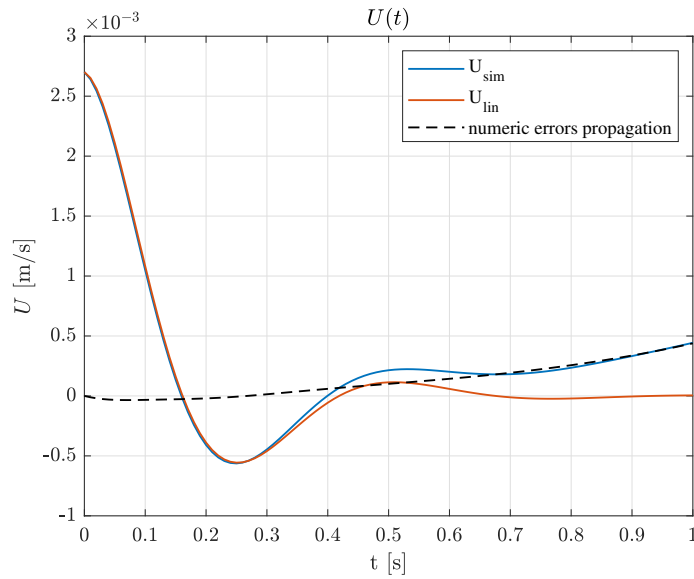


Figure 104: Responses comparison between analytic linearised model and numeric non-linear one - U .

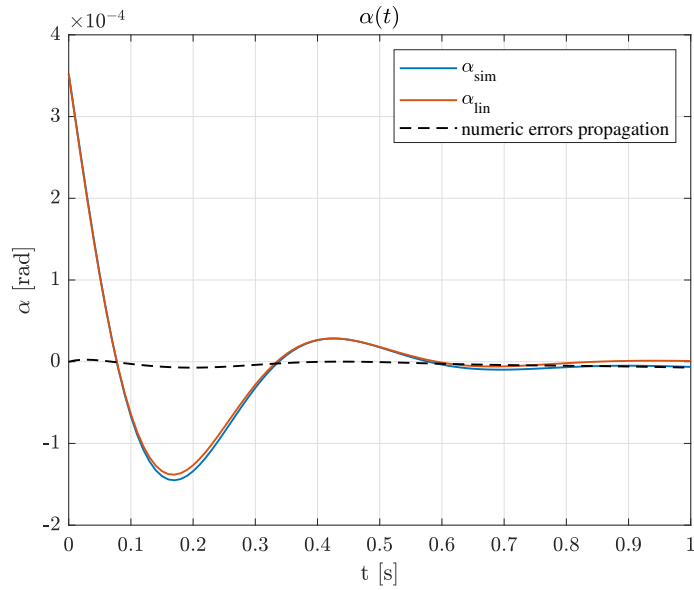


Figure 105: Responses comparison between analytic linearised model and numeric non-linear one - α .

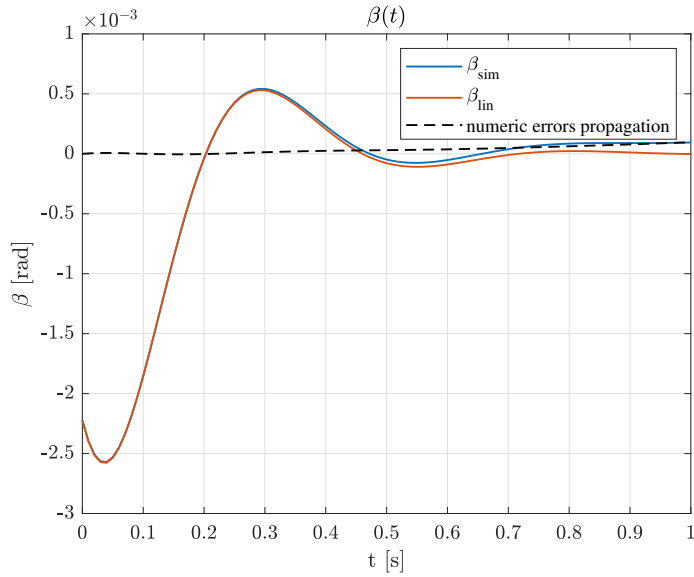


Figure 106: Responses comparison between analytic linearised model and numeric non-linear one - β .

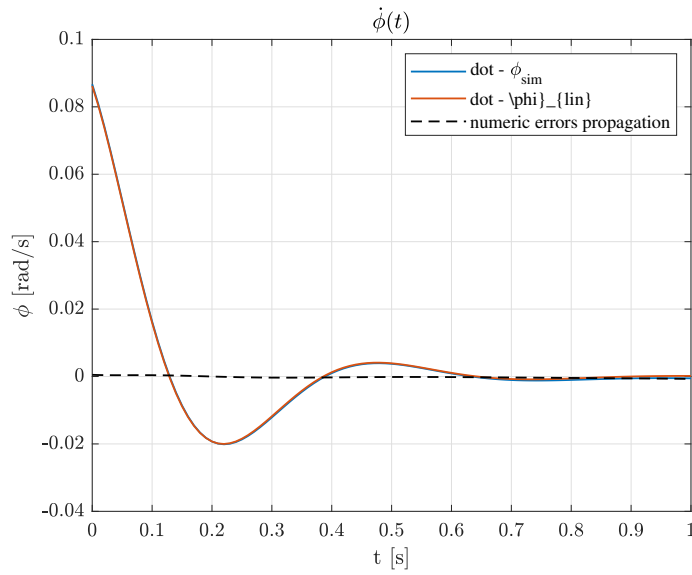


Figure 107: Responses comparison between analytic linearised model and numeric non-linear one - $\dot{\phi}$.

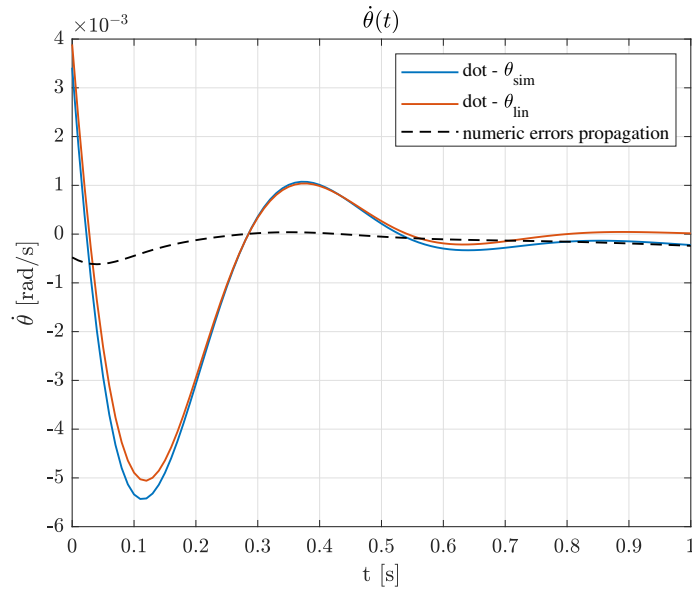


Figure 108: Responses comparison between analytic linearised model and numeric non-linear one - $\dot{\theta}$.

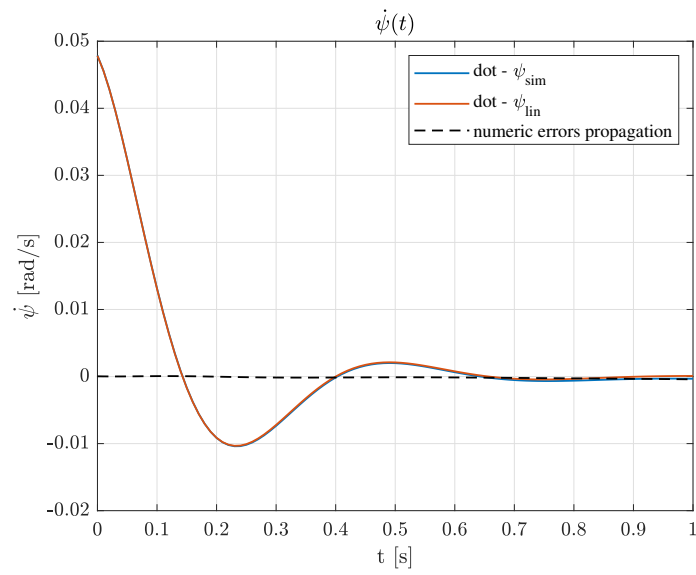


Figure 109: Responses comparison between analytic linearised model and numeric non-linear one - $\dot{\psi}$.